ISSN: 2161-4717 Volume 9, Number 2, June 2019

Scientific Research Publishing

International Journal of Astronomy and Astrophysics

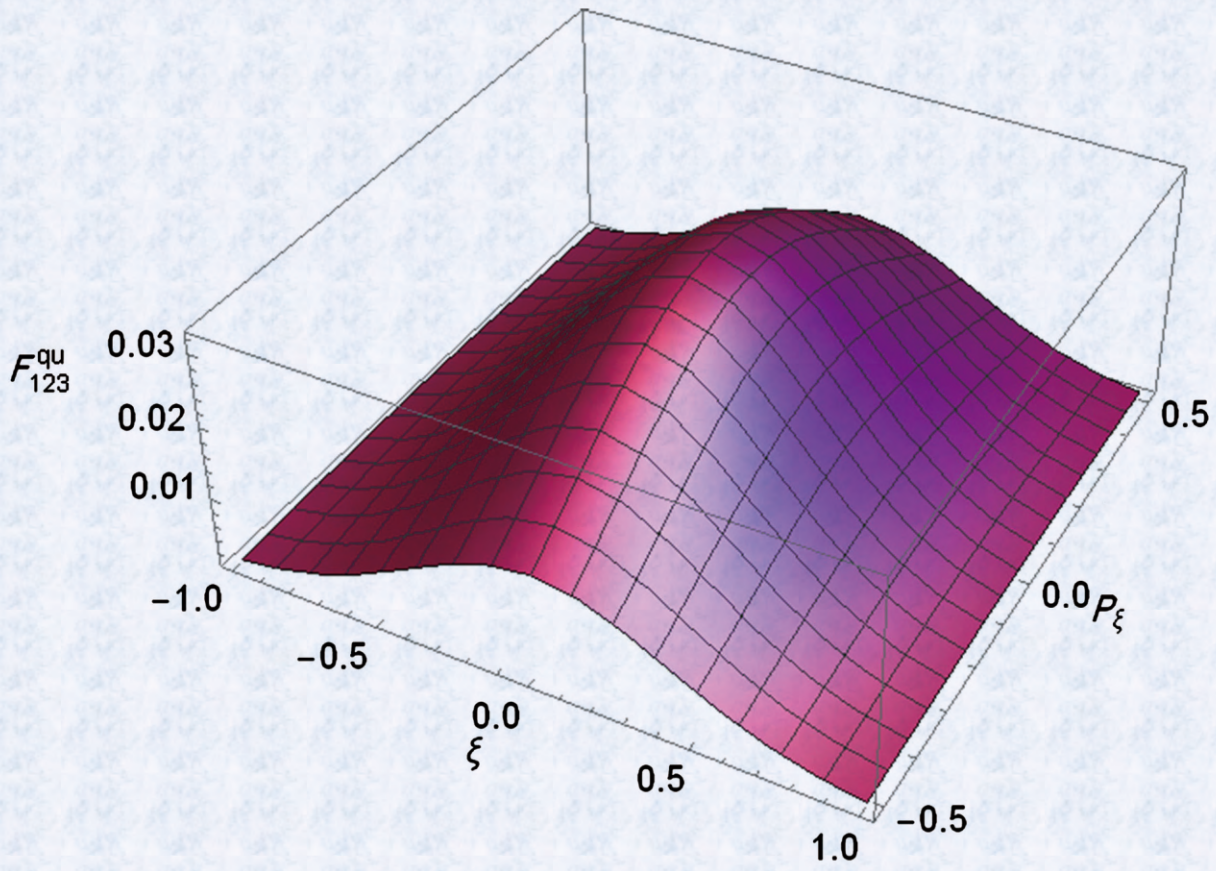

ISSN: 2161-4717

www.scirp.org/journal/ijaa

Journal Editorial Board

ISSN 2161-4717 (Print) ISSN 2161-4725 (Online)
http://www.scirp.org/journal/ijaa

Editor-in-Chief

Editorial Board

International Journal of Astronomy and Astrophysics, 2019, 9, 71-171
http://www.scirp.org/journal/ijaa
ISSN Online: 2161-4725
ISSN Print: 2161-4717

Table of Contents

Volume 9 Number 2 June 2019

The figure on the front cover is from the article published in International Journal of Astronomy and Astrophysics, 2019, Vol. 9, No. 2, pp. 115-132 by Nagat Abd El Rahman Hussein, *et al.*

International Journal of Astronomy and Astrophysics (IJAA)
Journal Information

SUBSCRIPTIONS

The *International Journal of Astronomy and Astrophysics* (Online at Scientific Research Publishing, www.SciRP.org) is published quarterly by Scientific Research Publishing, Inc., USA.

Subscription rates:
Print: $79 per issue.
To subscribe, please contact Journals Subscriptions Department, E-mail: sub@scirp.org

SERVICES

Advertisements
Advertisement Sales Department, E-mail: service@scirp.org

Reprints (minimum quantity 100 copies)
Reprints Co-ordinator, Scientific Research Publishing, Inc., USA.
E-mail: sub@scirp.org

COPYRIGHT

PRODUCTION INFORMATION

For manuscripts that have been accepted for publication, please contact:
E-mail: ijaa@scirp.org

Scientific Research Publishing

International Journal of Astronomy and Astrophysics, 2019, 9, 71-96
http://www.scirp.org/journal/ijaa
ISSN Online: 2161-4725
ISSN Print: 2161-4717

A Study of Dark Matter with Spiral Galaxy Rotation Curves

Bruce Hoeneisen

Universidad San Francisco de Quito, Quito, Ecuador
Email: bruce1@fnal.gov

How to cite this paper: Hoeneisen, B. (2019) A Study of Dark Matter with Spiral Galaxy Rotation Curves. *International Journal of Astronomy and Astrophysics*, **9**, 71-96.
https://doi.org/10.4236/ijaa.2019.92007

Received: April 2, 2019
Accepted: May 2, 2019
Published: May 5, 2019

Abstract

To constrain the properties of dark matter, we study spiral galaxy rotation curves measured by the THINGS collaboration. A model that describes a mixture of two self-gravitating non-relativistic ideal gases, "baryons" and "dark matter", reproduces the measured rotation curves within observational uncertainties. The model has four parameters that are obtained by minimizing a χ^2 between the measured and calculated rotation curves. From these four parameters, we calculate derived galaxy parameters. We find that dark matter satisfies the Boltzmann distribution. The onset of Fermi-Dirac or Bose-Einstein degeneracy obtains disagreement with observations and we determine, with 99% confidence, that the mass of dark matter particles is $m_h > 16$ eV if fermions, or $m_h > 45$ eV if bosons. We measure the root-mean-square velocity of dark matter particles in the spiral galaxies. This observable is of cosmological origin and allows us to obtain the root-mean-square velocity of dark matter particles in the early universe when perturbations were still linear. Extrapolating to the past we obtain the expansion parameter at which dark matter particles become non-relativistic: $a_{h\mathrm{NR}} = \left[4.17 \pm 0.34(\mathrm{stat}) \pm 2.50(\mathrm{syst})\right] \times 10^{-6}$. Knowing $\Omega_c \rho_{\mathrm{crit}}$ we then obtain the dark matter particle mass $m_h = 69.0 \pm 4.2(\mathrm{stat}) \pm 31.0(\mathrm{syst})$ eV, and the ratio of dark matter-to-photon temperature $T_h/T = 0.389 \pm 0.008(\mathrm{stat}) \pm 0.058(\mathrm{syst})$ after e^+e^- annihilation while dark matter remains ultra-relativistic. We repeat these measurements with ten galaxies with masses that span three orders of magnitude, and angular momenta that span five orders of magnitude, and obtain fairly consistent results. We conclude that dark matter was once in thermal equilibrium with the (pre?) Standard Model particles (hence the observed Boltzmann distribution) and then decoupled from the Standard Model and from self-annihilation at temperatures above m_μ. These results disfavor models with freeze-out or freeze-in. We also measure

the primordial amplitude of vector modes, and constrain the baryon-dark matter cross-section: $\sigma_{hb} \lesssim 2\times10^{-26}$ cm^2. Finally, we consider sterile Majorana neutrinos as a dark matter candidate.

Keywords

Dark Matter, Spiral Galaxies, Majorana Neutrinos

1. Introduction

The dark matter density in the core of spiral galaxies can exceed 10^7 times the mean dark matter density of the Universe. To learn about the properties of dark matter, we study the rotation curves of spiral galaxies measured by the THINGS collaboration [1]. The galaxies studied are in a stationary state, *i.e.* they have pulled away from the expansion of the Universe.

We use the standard notation for cosmology as defined in [2], and the values of the cosmological parameters presented therein. Sometimes we use units with $\hbar = 1$ and $c = 1$ as is customary.

2. A Model of Spiral Galaxy Rotation Curves

Figure 1 presents rotation curves of the spiral galaxy NGC 3198 measured by the THINGS collaboration [1]. The observed rotation curve $v_{\text{obs}}(r)$ has contributions from baryons $v_b(r)$ (stars in the disk and bulge, and gas), and from the halo of dark matter $v_h(r)$:

$$v_{\text{obs}}^2 \equiv v^2 = v_b^2 + v_h^2, \quad v_b^2 = v_{\text{disk}}^2 + v_{\text{bulge}}^2 + v_{\text{gas}}^2. \tag{1}$$

These rotation velocities correspond, by definition, to test particles in circular orbits of radius r in the plane of the galaxy. There is good agreement between the THINGS analysis and previous measurements by K. Begeman [3]. The mass distribution of stars is obtained from measurements of surface brightness in the 3.6μm band and models of the mass-to-light ratio $\Upsilon_*^{3.6}$. The mass distribution of gas is obtained from H_I maps. The uncertainties of $v(r)$ are from the THINGS observations and analysis [1]. We estimate the uncertainties of $v_b(r)$ from the scatter between 4 fits presented by the THINGS collaboration: "ISO, free", "ISO, fixed", "NFK, free", and "NFK, fixed" [1]. These fits assume either the Navarro, Frenk and White (NFK) halo model [4], or the pseudo-isothermal-gas (ISO) model.

From the measured rotation curves $v(r)$ and $v_b(r)$ we can obtain directly $g_b = -v_b^2/r$ and $g_h = -(v^2 - v_b^2)/r$. From $g_h = -M_h(r)G/r^2$ (assuming spherical symmetry) we can obtain

$$\rho_h = \frac{1}{4\pi G r^2}\frac{\mathrm{d}(r v_h^2)}{\mathrm{d}r}, \tag{2}$$

and similarly for ρ_b. We use these equations as cross-checks. Note that $\rho_h(r)$

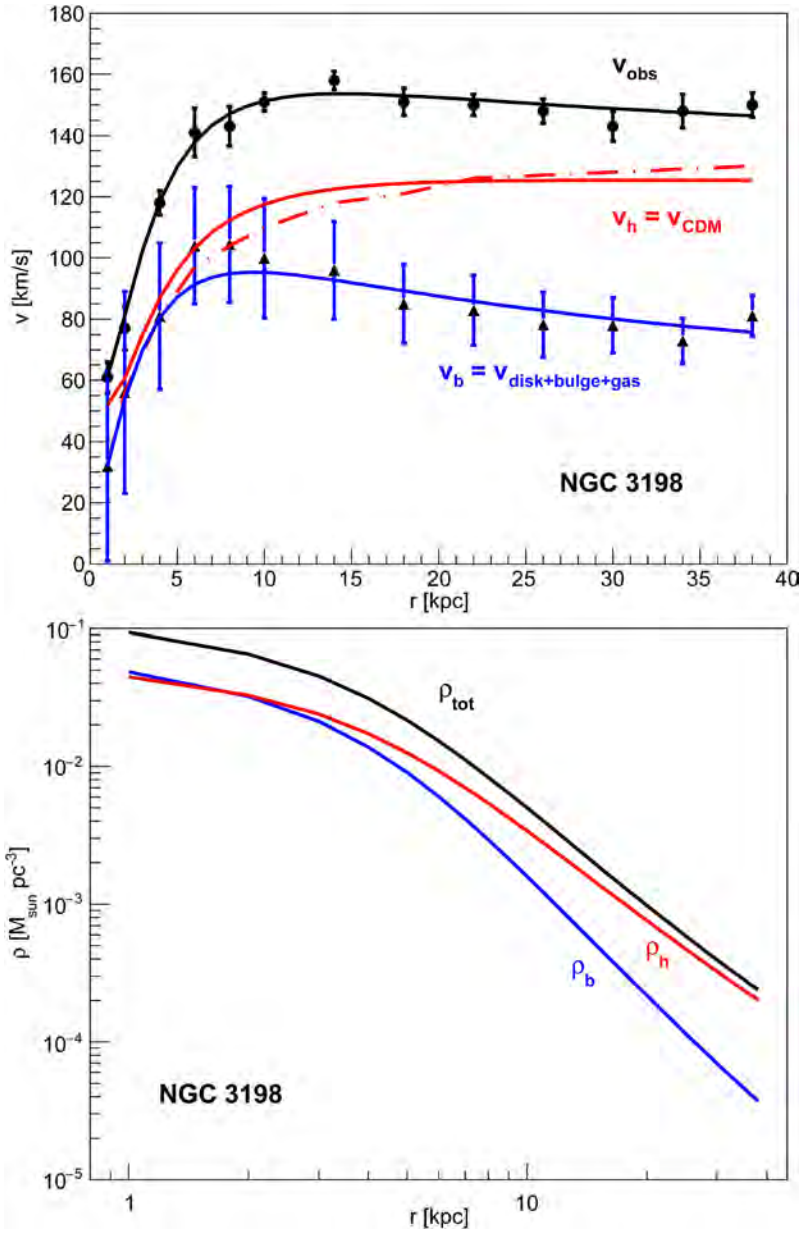

Figure 1. Top figure: Observed rotation curve $v_{obs}(r)$ (dots) and the baryon contribution $v_b(r)$ (triangles) of galaxy NGC 3198 obtained by the THINGS collaboration [1]. The "ISO, free" fit obtains $v_h(r)$ (dash-dotted line) [1]. The solid lines are obtained by numerical integration as explained in the text. The fitted parameters are given in **Table 1**. Bottom figure: Mass densities of baryons and of dark matter of galaxy NGC 3198 obtained by numerical integration as explained in the text.

and $\rho_b(r)$ are insensitive to whether or not the dark matter is rotating.

In the present analysis we would like to go further, *i.e.* constrain the equation of state of dark matter. To this end we compare the measured rotation curves with the following simplified model of a mixture of two self-gravitating non-relativistic ideal gases: "baryons" and "dark matter". We assume that the interactions between baryons and dark matter can be neglected.

Table 1. Fitted parameters with $\kappa_b = 0$, and $\kappa_h = 0$. The last column shows the χ^2 of the fit and the number of degrees of freedom. The fits are presented in **Figures 1-10**.

Galaxy	$\langle v_{rh}^2 \rangle^{1/2}$ [km/s]	$\langle v_{rb}^2 \rangle^{1/2}$ [km/s]	$\rho_h(r_{\min})$ $[10^{-2} M_\odot \cdot \mathrm{pc}^{-3}]$	$\rho_b(r_{\min})$ $[10^{-2} M_\odot \cdot \mathrm{pc}^{-3}]$	χ^2 / d.f.
NGC 2403	101 ± 3	63.4 ± 1.8	7.5 ± 1.4	30.4 ± 6.2	7.2/20
NGC 2841	220 ± 3	168 ± 3	9.3 ± 0.7	9.7 ± 1.2	22.1/22
NGC 2903	142 ± 3	117 ± 3	14.6 ± 2.1	25.2 ± 3.1	29.0/24
NGC 2976	129 ± 177	49 ± 6	4.0 ± 2.7	17.0 ± 3.7	9.8/16
NGC 3198	104 ± 3	90 ± 3	4.5 ± 0.8	4.9 ± 1.2	8.3/22
NGC 3521	153 ± 10	136 ± 5	22.9 ± 8.6	43.4 ± 11.8	6.8/20
NGC 3621	126 ± 5	78.8 ± 1.0	2.6 ± 0.5	26.6 ± 1.5	13.2/22
DDO 154	36.5 ± 3.7	22.3 ± 1.7	1.3 ± 0.3	1.9 ± 0.8	7.5/18
NGC 5055	144 ± 4	130 ± 3	28.2 ± 6.8	41.4 ± 10.1	19.2/24
NGC 7793	85.5 ± 5.0	52.2 ± 1.5	8.0 ± 1.6	29.7 ± 4.4	36.3/16

$$\nabla \cdot \boldsymbol{g}_b = -4\pi G \rho_b, \quad \nabla \cdot \boldsymbol{g}_h = -4\pi G \rho_h, \tag{3}$$

$$\boldsymbol{g} = \boldsymbol{g}_b + \boldsymbol{g}_h, \quad g_b \equiv -\frac{v_b^2}{r}, \quad g_h \equiv -\frac{v_h^2}{r}, \quad v^2 \equiv v_b^2 + v_h^2, \tag{4}$$

$$\nabla P_b = \rho_b \left(\boldsymbol{g} + \kappa_b \frac{v^2}{r} \hat{\boldsymbol{e}}_r \right), \quad \nabla P_h = \rho_h \left(\boldsymbol{g} + \kappa_h \frac{v^2}{r} \hat{\boldsymbol{e}}_r \right), \tag{5}$$

$$P_b = \langle v_{rb}^2 \rangle \rho_b \quad \text{and} \quad P_h = \langle v_{rh}^2 \rangle \rho_h \left(1 \pm \rho_h \frac{\pi^{3/2} \hbar^3}{2 \langle v_{rh}^2 \rangle^{3/2} N_{f,b} m_h^4} + \cdots \right). \tag{6}$$

$\langle v_{rb}^2 \rangle$ and $\langle v_{rh}^2 \rangle$ are the mean-square of the velocity components in the radial direction r of baryons and dark matter respectively. Newton's Equation (3) determine the gravitational field $\boldsymbol{g}(r) = \boldsymbol{g}_b(r) + \boldsymbol{g}_h(r)$ due to the densities $\rho_b(r)$ of baryons and $\rho_h(r)$ of dark matter. Equations (5) express momentum conservation and are valid even for collisionless gases. The centrifugal acceleration terms proportional to κ_b and κ_h are inserted to study the rotation of baryons and dark matter.

We consider dark matter to be a mixture of interacting or non-interacting particles of masses m_{hi}. Let $n_{hi}(r, v_r)\mathrm{d}v_r$ be the number density of dark matter particles of mass m_{hi} with radial component of velocity between v_r and $v_r + \mathrm{d}v_r$. Then

$$\rho_h = \sum_i m_{hi} \int_0^\infty n_{hi}(r, v_r)\mathrm{d}v_r, \quad P_h \equiv \langle v_{rh}^2 \rangle \rho_h, \tag{7}$$

where

$$\langle v_{rh}^2 \rangle \equiv \frac{\sum_i m_{hi} \int_0^\infty v_r^2 \cdot n_{hi}(r, v_r)\mathrm{d}v_r}{\sum_i m_{hi} \int_0^\infty n_{hi}(r, v_r)\mathrm{d}v_r}, \tag{8}$$

and similarly for baryons. The pressure $P_h(r)$ is the momentum component in the radial direction in the galactic plane per unit time traversing unit area at r with $v_r > 0$.

Equations (6) are the equations of state of the gasses. For the dark matter halo we have included a term due to the onset of degeneracy of fermions (upper signs) or bosons (lower signs). N_f (N_b) is the number of fermion (boson) degrees of freedom. We take $N_f = 2$ for one flavor of spin-up and spin-down sterile Majorana neutrinos. Results can be amended for other cases. For bosons we take $N_b = 1$. Fermi-Dirac and Bose-Einstein degeneracy will be considered in Section 7. For now we set m_h to some large value, e.g. $m_h = 500$ eV, so the last term in Equation (6) is negligible.

We integrate numerically Equations (3) to (6) from $r_{\min}$ to $r_{\max}$ along a radial direction in the galactic plane. Hence $\nabla P_h = \hat{\boldsymbol{e}}_r \mathrm{d}P_h/\mathrm{d}r$ and $\nabla \cdot \boldsymbol{g}_h = \left(1/r^2\right)\mathrm{d}\left(r^2 g_h\right)/\mathrm{d}r$, and similarly for baryons.

Variables κ_b and $\langle v_{rb}^2 \rangle$, and also κ_h and $\langle v_{rh}^2 \rangle$, occur in the combinations

$$\langle v_{rb}^2 \rangle' \equiv \frac{\langle v_{rb}^2 \rangle}{1-\kappa_b}, \quad \langle v_{rh}^2 \rangle' \equiv \frac{\langle v_{rh}^2 \rangle}{1-\kappa_h}, \tag{9}$$

if the last term in (6) is negligible. To lift this degeneracy and obtain these variables separately, we need information in addition to the galaxy rotation curves.

We fit four parameters to minimize the χ^2 between the measured and calculated rotation velocities $v(r)$ and $v_b(r)$: the starting densities $\rho_h(r_{\min})$ and $\rho_b(r_{\min})$, and the "reduced" root-mean-square radial velocities $\langle v_{rh}^2 \rangle'$, and $\langle v_{rb}^2 \rangle'$. These parameters are boundary conditions at $r \to 0$ and $r \to \infty$. Assuming $\langle v_{rh}^2 \rangle'$ and $\langle v_{rb}^2 \rangle'$ are independent of r we obtain fits to the galaxy rotation curves that are in agreement with observations, within the experimental uncertainties, as shown in **Figures 1-10**, and in **Table 1**. The parameter correlation coefficients for galaxy NGC 3198 are shown in **Table 2**.

3. Derived Galaxy Parameters

We define $M_b(r)$ as the baryon mass contained within r, and similarly for $M_h(r)$. Equations (3) to (6) allow the definition of several galaxy parameters: the "equal density radius" r_{ed} with $\rho_b(r_{\text{ed}}) = \rho_h(r_{\text{ed}})$, the "galaxy proper radius"

Table 2. Correlation coefficients of the four fitted parameters in **Table 1** for galaxy NGC 3198.

	$\langle v_{rh}^2 \rangle'^{1/2}$	$\langle v_{rb}^2 \rangle'^{1/2}$	$\rho_h(r_{\min})$	$\rho_b(r_{\min})$
$\langle v_{rh}^2 \rangle'^{1/2}$	1.000	−0.833	−0.802	0.860
$\langle v_{rb}^2 \rangle'^{1/2}$	−0.833	1.000	0.775	−0.831
$\rho_h(r_{\min})$	−0.802	0.775	1.000	−0.639
$\rho_b(r_{\min})$	0.860	−0.831	−0.639	1.000

r_g at which $M_b(r_g)/M_h(r_g) = \Omega_b/\Omega_c$, and the corresponding "primordial comoving radius" r_c defined by $M_b \equiv \frac{4}{3}\pi r_c^3 \Omega_b \rho_{\text{crit}}$. The "baryon mass" M_b converges, so we define $M_b \equiv M_b(r_g)$. In the early Universe, when the perturbation that formed the galaxy was still linear, the matter of the galaxy was contained in the expanding sphere of proper radius r_g, and comoving radius r_c at

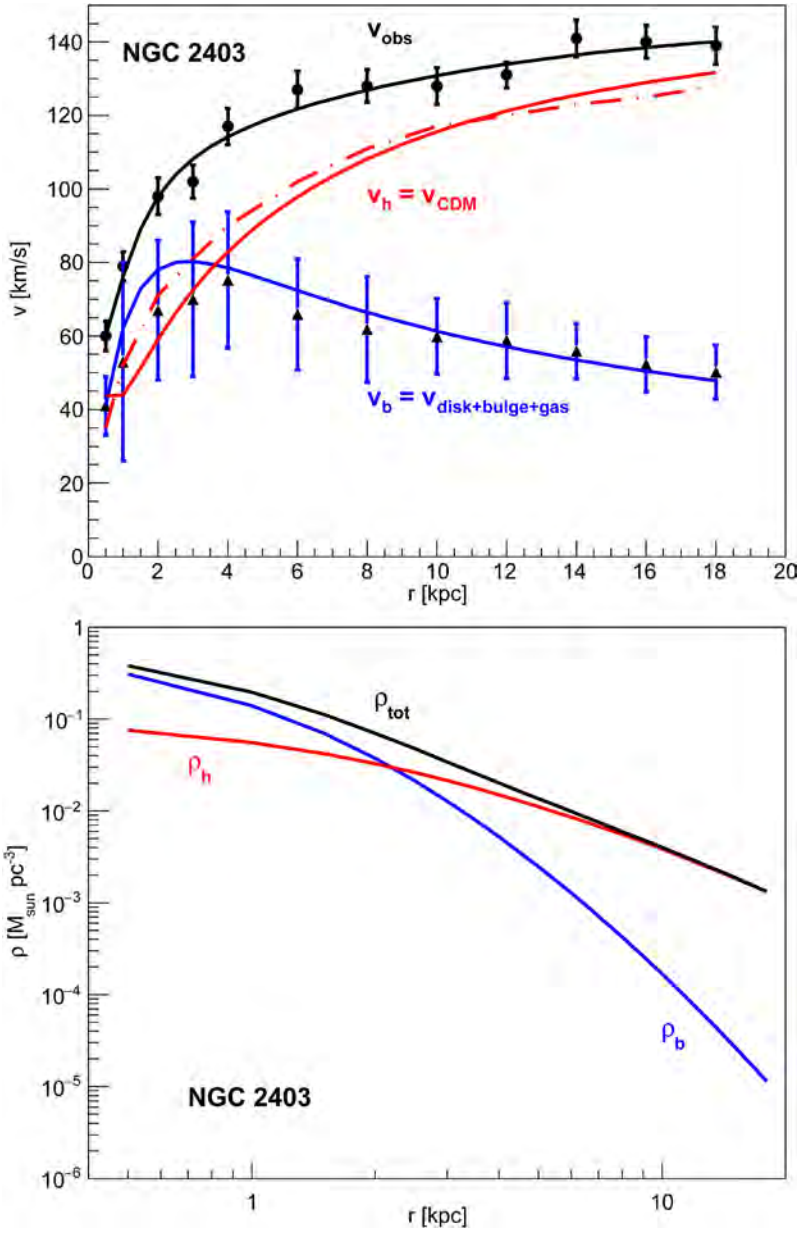

Figure 2. Top figure: Observed rotation curve $v_{\text{obs}}(r)$ (dots) and the baryon contribution $v_b(r)$ (triangles) of galaxy NGC 2403 obtained by the THINGS collaboration [1]. The "NFW, free" fit obtains $v_h(r)$ (dash-dotted line) [1]. The solid lines are obtained by numerical integration for non-degenerate dark matter as explained in the text. The fitted parameters are given in **Table 1**. Bottom figure: Mass densities of baryons and of dark matter of galaxy NGC 2403 obtained by numerical integration as explained in the text.

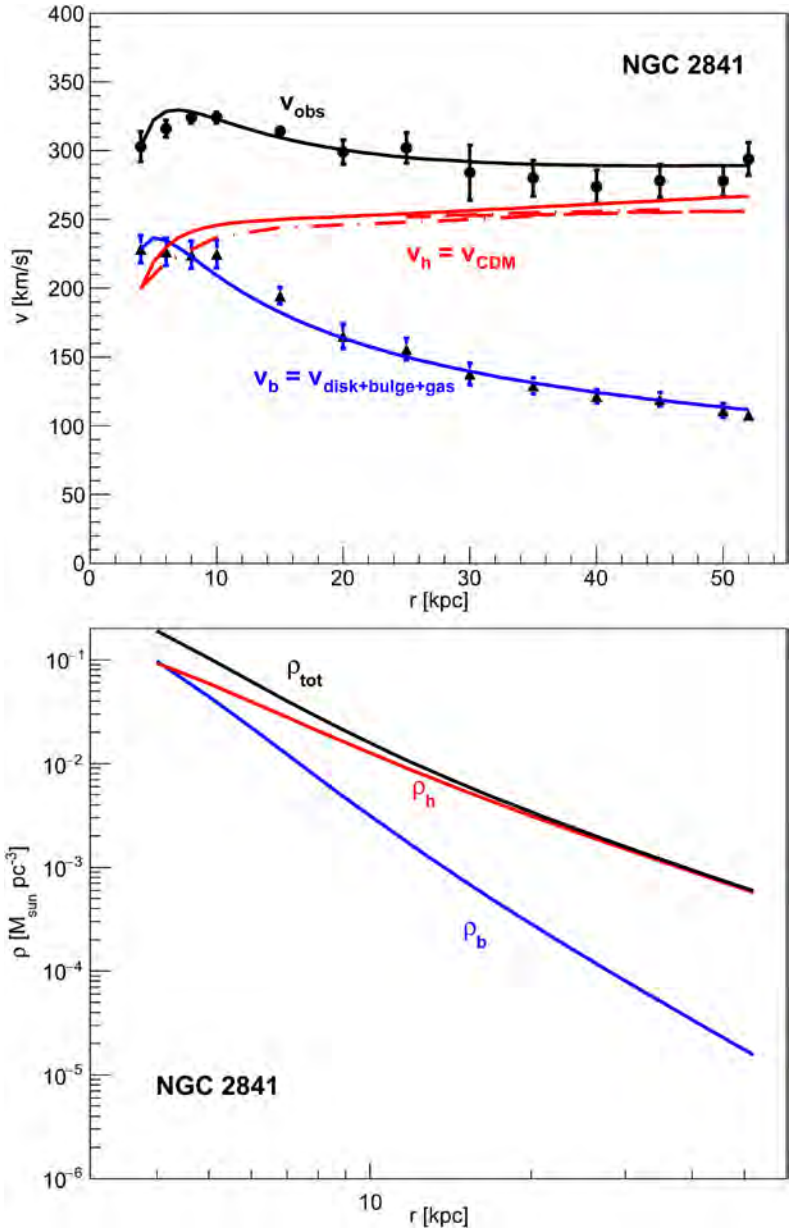

Figure 3. Top figure: Observed rotation curve $v_{obs}(r)$ (dots) and the baryon contribution $v_b(r)$ (triangles) of galaxy NGC 2841 obtained by the THINGS collaboration [1]. The "ISO, free" fit obtains $v_h(r)$ (dash-dotted line) [1]. The solid lines are obtained by numerical integration as explained in the text. The fitted parameters are given in **Table 1**. Bottom figure: Mass densities of baryons and of dark matter of galaxy NGC 2841 obtained by numerical integration as explained in the text.

time t_g. At time t_g the expansion parameter is r_g/r_c. The results, obtained with the four fitted parameters listed in **Table 1**, are presented in **Table 3**. The angular momenta of baryons L_b inside r_g are given in **Table 4**.

4. Estimate of κ_b

As an example, let us consider the spiral galaxy NGC 2403. A distribution of ve-

locities along a particular line of sight is presented in figure 3 of [1]. The central value is ≈186 km/s, and the standard deviation is ≈11 km/s. So we estimate $\sqrt{\kappa_b}v\big/\left\langle v_{rb}^2\right\rangle^{1/2} \approx 186/11$. From **Table 1**, $\left\langle v_{rb}^2\right\rangle'^{1/2} \equiv \left\langle v_{rb}^2\right\rangle^{1/2}\big/\left(1-\kappa_b\right)^{1/2} = 63.4 \pm 1.8$ km/s, and from **Figure 2**, $v \approx 140$ km/s. From these relations we obtain $\kappa_b \approx 0.98$, so the trajectories of stars and gas are approximately circular.

5. Estimate of κ_h

Consider an expanding sphere of proper radius r_g and comoving radius r_c at time t_g containing the matter that will become spiral galaxy NGC 2403. We assume adiabatic primordial perturbations, so the velocity fields of baryons and

Table 3. Galaxy parameters obtained by numerical integration with the fitted parameters in **Table 1**. See Section 3 for definitions.

Galaxy	M_b $\left[10^{10} M_\odot\right]$	r_{ed} [kpc]	r_g [kpc]	r_c [Mpc]	t_g [Gyr]
NGC 2403	$0.9\times e^{\pm 0.22}$	$2.2\times e^{\pm 0.28}$	$13.6\times e^{\pm 0.24}$	$0.7\times e^{\pm 0.07}$	$0.047\times e^{\pm 0.25}$
NGC 2841	$15\times e^{\pm 0.13}$	$4.1\times e^{\pm 0.12}$	$48.5\times e^{\pm 0.18}$	$1.8\times e^{\pm 0.04}$	$0.077\times e^{\pm 0.20}$
NGC 2903	$10\times e^{\pm 0.46}$	$3.5\times e^{\pm 0.20}$	$74\times e^{\pm 0.47}$	$1.6\times e^{\pm 0.15}$	$0.18\times e^{\pm 0.48}$
NGC 2976	$0.4\times e^{\pm 0.58}$	$1.8\times e^{\pm 0.41}$	$6.3\times e^{\pm 0.47}$	$0.5\times e^{\pm 0.19}$	$0.022\times e^{\pm 0.45}$
NGC 3198	$9\times e^{\pm 1.0}$	$1.9\times e^{\pm 1.0}$	$128\times e^{\pm 1.0}$	$1.5\times e^{\pm 0.34}$	$0.42\times e^{\pm 1.0}$
NGC 3521	$69\times e^{\pm 1.8}$	$5.0\times e^{\pm 0.87}$	$403\times e^{\pm 2.0}$	$3.0\times e^{\pm 0.60}$	$0.86\times e^{\pm 1.5}$
NGC 3621	$3.9\times e^{\pm 0.18}$	$5.8\times e^{\pm 0.15}$	$38\times e^{\pm 0.20}$	$1.1\times e^{\pm 0.06}$	$0.11\times e^{\pm 0.22}$
DDO 154	$0.07\times e^{\pm 0.48}$	$1.1\times e^{\pm 0.65}$	$7.0\times e^{\pm 0.46}$	$0.3\times e^{\pm 0.16}$	$0.062\times e^{\pm 0.46}$
NGC 5055	$62\times e^{\pm 1.3}$	$2.3\times e^{\pm 0.77}$	$416\times e^{\pm 1.5}$	$2.9\times e^{\pm 0.42}$	$0.95\times e^{\pm 1.5}$
NGC 7793	$0.5\times e^{\pm 0.23}$	$1.6\times e^{\pm 0.19}$	$10\times e^{\pm 0.27}$	$0.6\times e^{\pm 0.08}$	$0.04\times e^{\pm 0.30}$

Table 4. Baryon angular momentum L_b within radius r_g obtained by numerical integration (assuming $\kappa_b = 0.98$), and limits on m_h at 99% confidence. r_g is defined in Section 3.

Galaxy	$\log_{10}\left\{L_b\big/\left[M_\odot \text{ km/s}\cdot\text{pc}\right]\right\}$	Fermion $m_h>$	Boson $m_h>$
NGC 2403	12.63 ± 0.17	18 eV	no limit
NGC 2841	14.65 ± 0.15	12 eV	35 eV
NGC 2903	14.61 ± 0.44	18 eV	40 eV
NGC 2976	11.93 ± 0.43	no limit	no limit
NGC 3198	14.76 ± 0.94	16 eV	45 eV
NGC 3521	16.37 ± 1.58	10 eV	no limit
NGC 3621	13.73 ± 0.15	no limit	no limit
DDO 154	10.86 ± 0.36	30 eV	no limit
NGC 5055	16.32 ± 1.07	no limit	no limit
NGC 7793	12.13 ± 0.19	25 eV	no limit

of dark matter are the same. Then the angular momenta of baryons and dark matter in the sphere of proper radius r_g are in the ratio $L_b/L_h = M_b/M_h(r_g) = \Omega_b/\Omega_h$. According to the model of hierarchical formation of galaxies [5] [6], the sphere of radius r_g expands, reaches maximum expansion, and then collapses to form a galaxy, see figure 5 of Reference [6]. The angular momenta L_b and L_h are conserved if we neglect mixing. The density becomes approximately proportional

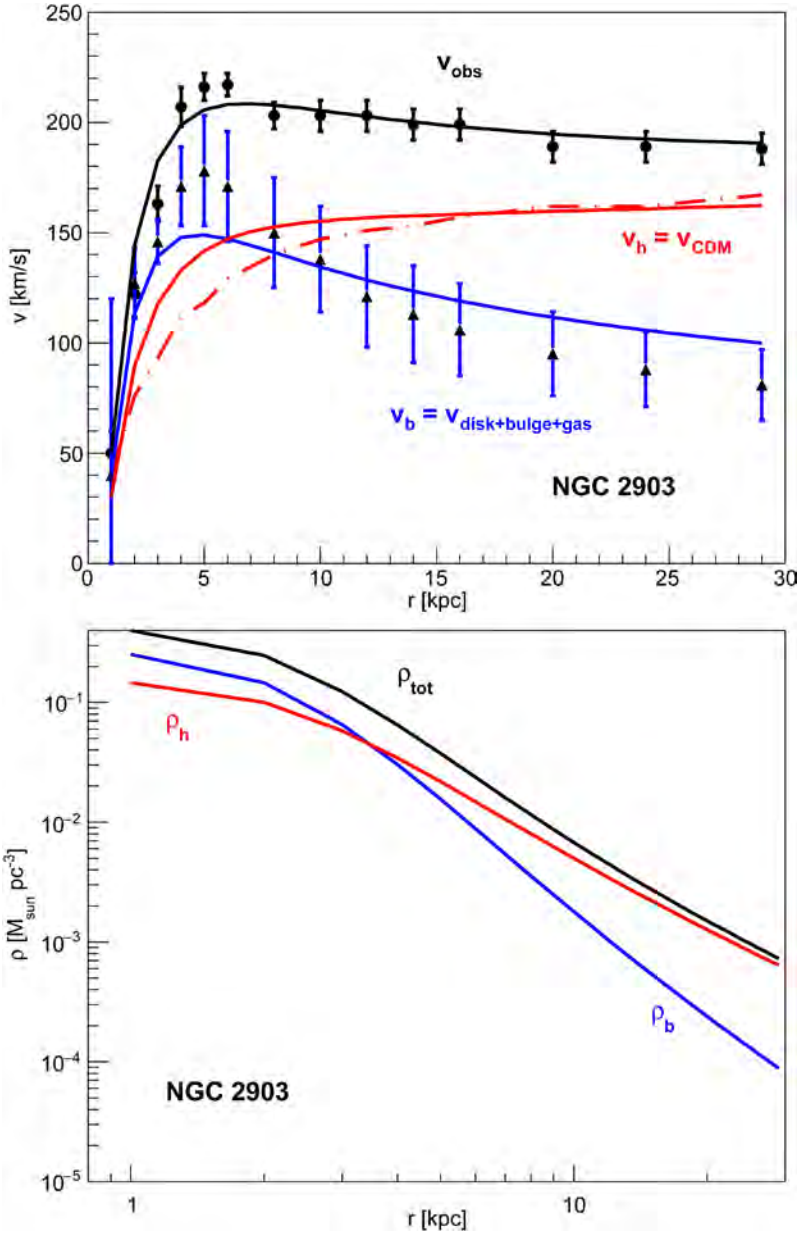

Figure 4. Top figure: Observed rotation curve $v_{obs}(r)$ (dots) and the baryon contribution $v_b(r)$ (triangles) of galaxy NGC 2903 obtained by the THINGS collaboration [1]. The "ISO, free" fit obtains $v_h(r)$ (dash-dotted line) [1]. The solid lines are obtained by numerical integration as explained in the text. The fitted parameters are given in **Table 1**. Bottom figure: Mass densities of baryons and of dark matter of galaxy NGC 2903 obtained by numerical integration as explained in the text.

to $1/r^2$. If dark matter rotates with velocity $\sqrt{\kappa_h}v$ the angular momentum of dark matter of the galaxy of radius r_g is $L_h \approx (\pi/8) M_h \sqrt{\kappa_h} v r_g$. From the numerical integration for galaxy NGC 2403, $L_b = 0.15 M_b \sqrt{\kappa_b} v r_g$ with $\kappa_b = 0.98$. Solving for κ_h we obtain $\kappa_h \approx 0.143$.

For galaxy NGC 3198 we obtain $L_b = 0.16 M_b \sqrt{\kappa_b} v r_g$ with $\kappa_b = 0.98$, and $\kappa_h \approx 0.163$.

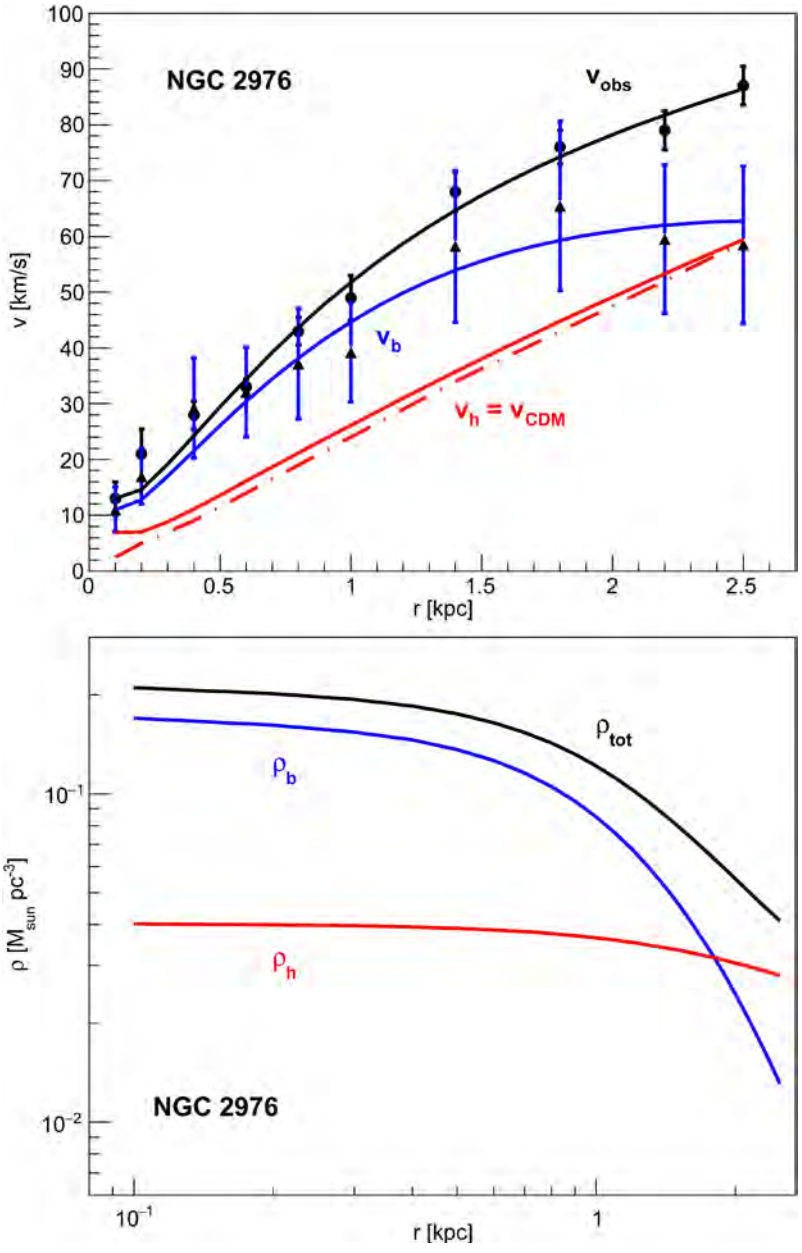

Figure 5. Top figure: Observed rotation curve $v_{obs}(r)$ (dots) and the baryon contribution $v_b(r)$ (triangles) of galaxy NGC 2976 obtained by the THINGS collaboration [1]. The "ISO, free" fit obtains $v_h(r)$ (dash-dotted line) [1]. The solid lines are obtained by numerical integration as explained in the text. The fitted parameters are given in **Table 1**. Bottom figure: Mass densities of baryons and of dark matter of galaxy NGC 2976 obtained by numerical integration as explained in the text.

6. The Boltzmann Distribution

Excellent fits to the rotation curves are obtained from Equations (3) to (6) with $\left\langle v_{rb}^2 \right\rangle'$ and $\left\langle v_{rh}^2 \right\rangle'$ independent of r, and non-degenerate dark matter. Since for the galaxies under consideration $\kappa_b \approx 1$ and $\kappa_h \approx 0$, we will neglect the possible dependence of κ_b and κ_h on r. From (5) and (6) we obtain

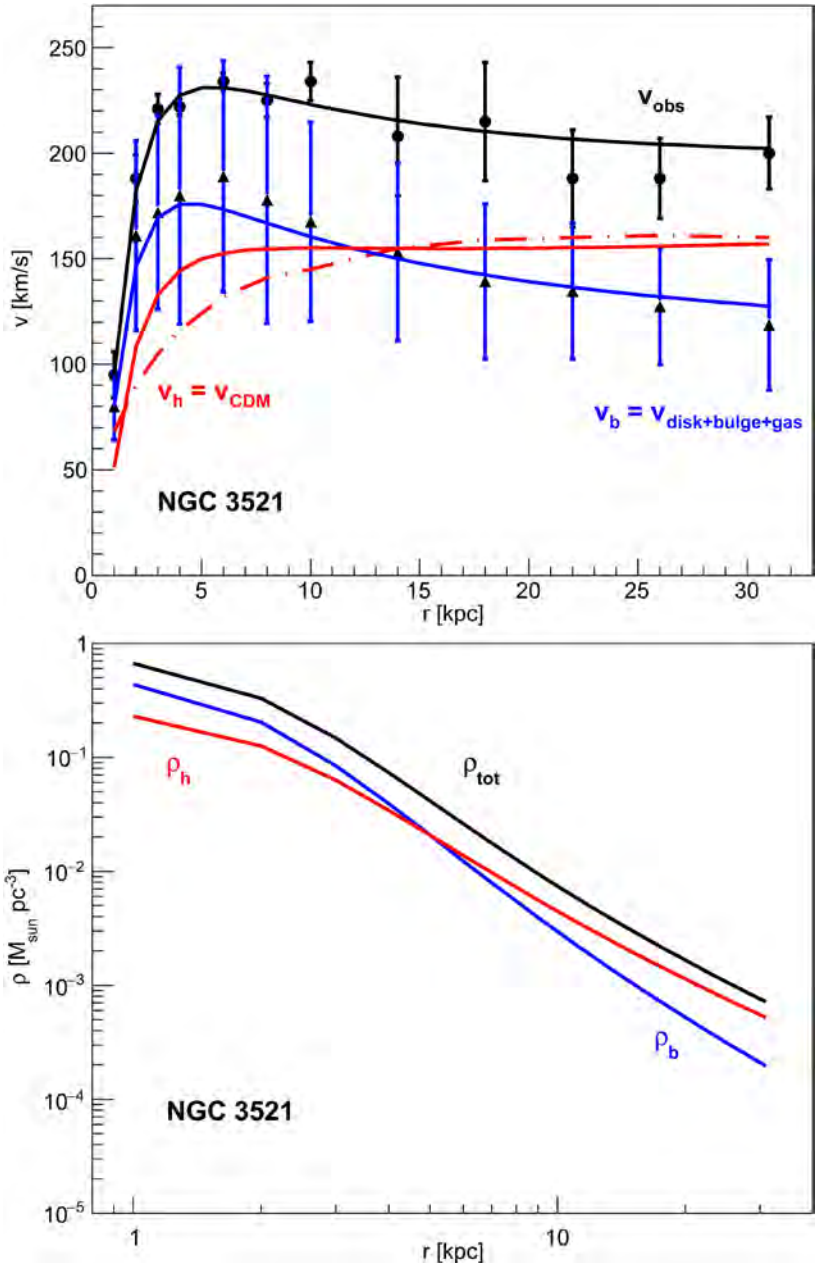

Figure 6. Top figure: Observed rotation curve $v_{\text{obs}}(r)$ (dots) and the baryon contribution $v_b(r)$ (triangles) of galaxy NGC 3521 obtained by the THINGS collaboration [1]. The "NFW, free" fit obtains $v_h(r)$ (dash-dotted line) [1]. The solid lines are obtained by numerical integration as explained in the text. The fitted parameters are given in **Table 1**. Bottom figure: Mass densities of baryons and of dark matter of galaxy NGC 3521 obtained by numerical integration as explained in the text.

$$\rho_h \propto \exp\left[\frac{-\phi(r)}{\langle v_{rh}^2 \rangle'}\right], \quad n_{hi}(r, v_r) \propto \exp\left[\frac{-v_r^2/2 - \phi(r)}{\langle v_{rh}^2 \rangle'}\right], \tag{10}$$

where $\phi(r) \equiv -\int g(r)\mathrm{d}r$ is the gravitational potential. Note that $v_r^2/2 + \phi(r)$ is conserved. So, within the observational uncertainties of the galaxy rotation curves, dark matter satisfies the Boltzmann distribution (10). This is a non-trivial

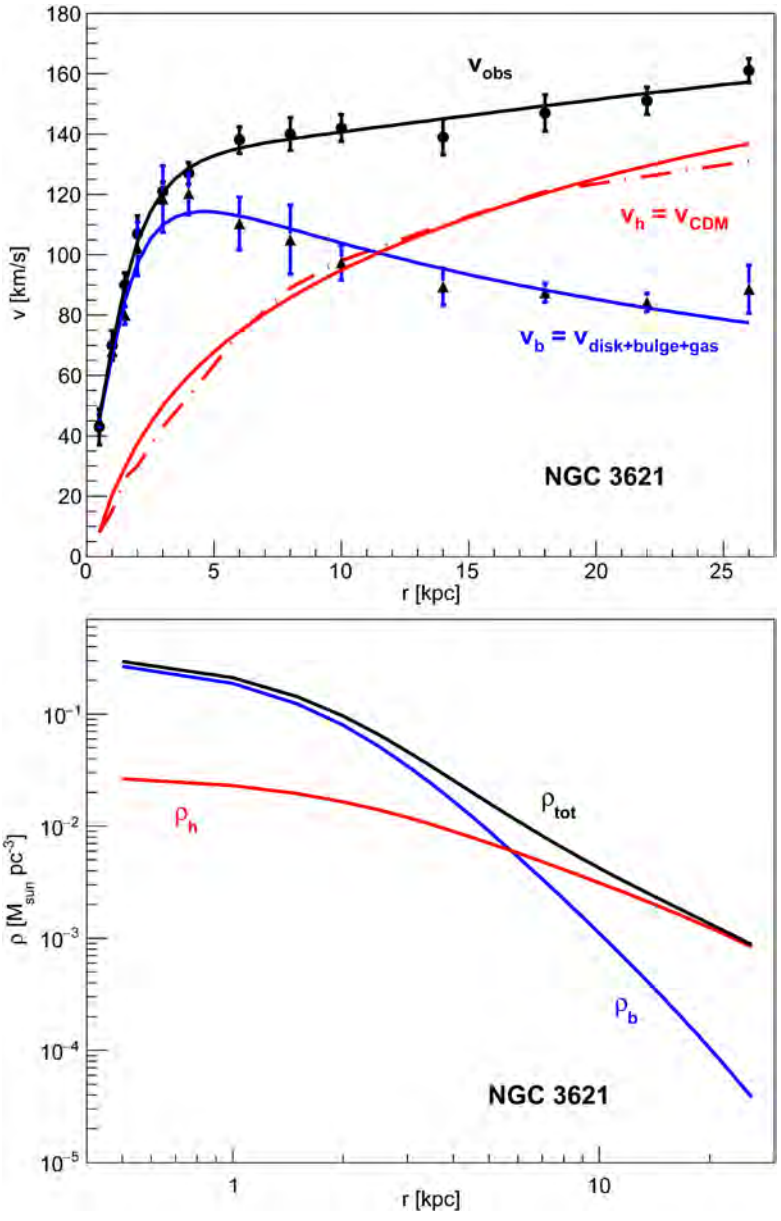

Figure 7. Top figure: Observed rotation curve $v_{\text{obs}}(r)$ (dots) and the baryon contribution $v_b(r)$ (triangles) of galaxy NGC 3621 obtained by the THINGS collaboration [1]. The "ISO, free" fit obtains $v_h(r)$ (dash-dotted line) [1]. The solid lines are obtained by numerical integration as explained in the text. The fitted parameters are given in Table 1. Bottom figure: Mass densities of baryons and of dark matter of galaxy NGC 3621 obtained by numerical integration as explained in the text.

result. The derivation of the Boltzmann distribution in statistical mechanics assumes that the "system" under study is in "thermal equilibrium" with a "reservoir", and implies the equipartition theorem, e.g. $\frac{1}{2}m_i v_i^2 = \frac{1}{2}m_j v_j^2$, which does not hold between dark matter and baryons. There is no obvious "reservoir" interacting with the dark matter, so the well known derivation of the Boltzmann

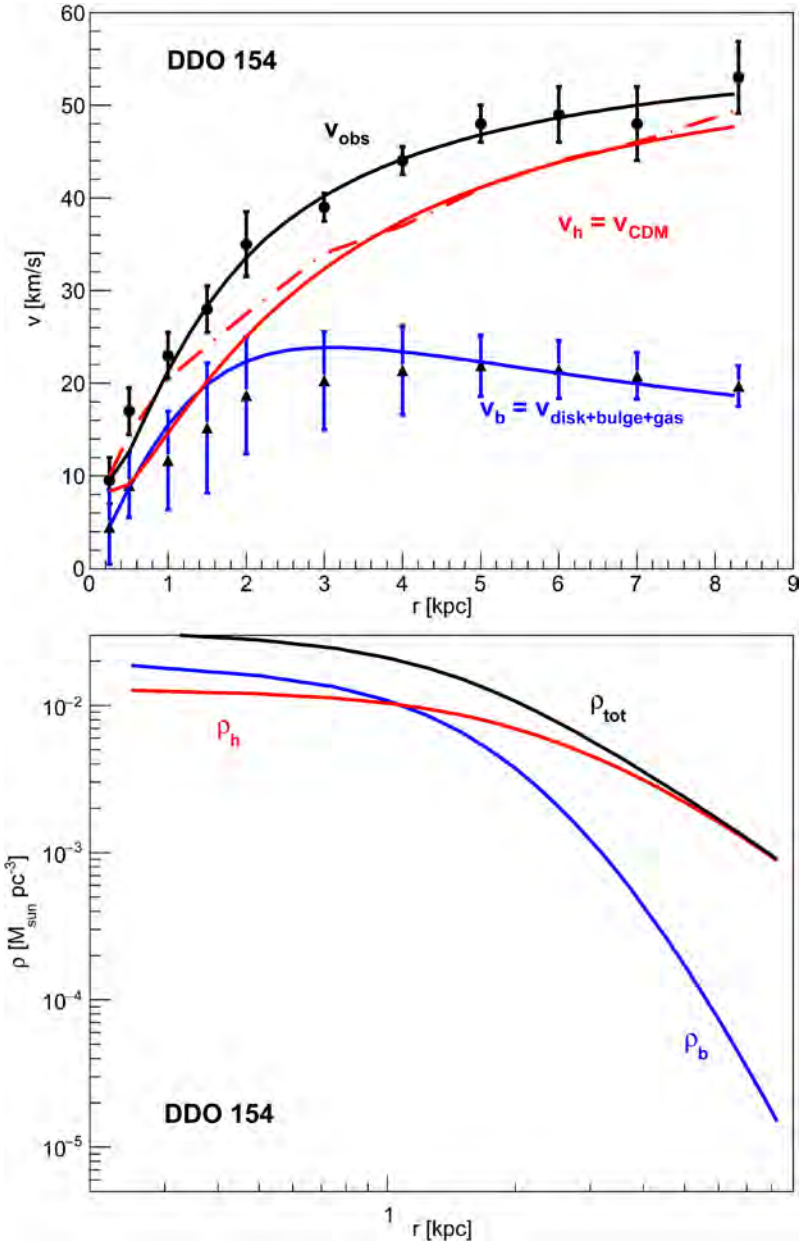

Figure 8. Top figure: Observed rotation curve $v_{obs}(r)$ (dots) and the baryon contribution $v_b(r)$ (triangles) of galaxy DDO 154 obtained by the THINGS collaboration [1]. The "NFW, free" fit obtains $v_h(r)$ (dash-dotted line) [1]. The solid lines are obtained by numerical integration for non-degenerate dark matter as explained in the text. The fitted parameters are given in **Table 1**. Bottom figure: Matter densities of baryons and of dark matter of galaxy DDO 154 obtained by numerical integration as explained in the text.

distribution may not apply to dark matter, unless dark matter was once in thermal equilibrium with "something". Does the observed Boltzmann distribution suggest that dark matter was once in statistical equilibrium with the primordial (pre?) Standard Model cosmological soup?

7. Lower Bounds on m_h for Fermions and Bosons

So far we have not considered the last term in Equation (6), *i.e.* we have set m_h

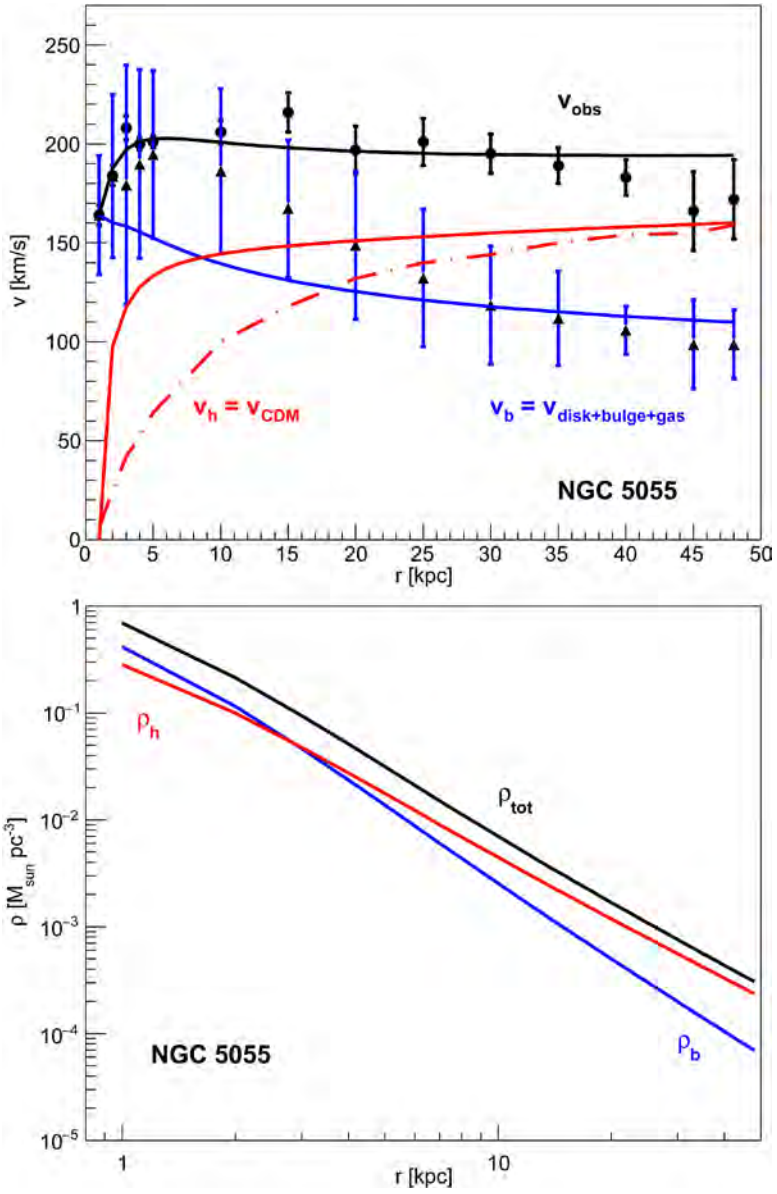

Figure 9. Top figure: Observed rotation curve $v_{obs}(r)$ (dots) and the baryon contribution $v_b(r)$ (triangles) of galaxy NGC 5055 obtained by the THINGS collaboration [1]. The "ISO, fixed" fit obtains $v_h(r)$ (dash-dotted line) [1]. The solid lines are obtained by numerical integration as explained in the text. The fitted parameters are given in **Table 1**. Bottom figure: Mass densities of baryons and of dark matter of galaxy NGC 5055 obtained by numerical integration as explained in the text.

to some high value. Note that we obtain excellent fits to the galaxy rotation curves assuming $P_h(r) = \langle v_{rh}^2 \rangle \rho_h(r)$ with $\langle v_{rh}^2 \rangle$ independent of *r*. By lowering the value of m_h in the fits we can probe non-linearities between $P_h(r)$ and $\rho_h(r)$. In particular, we study the onset of Fermi-Dirac or Bose-Einstein degeneracy of dark matter composed of particles of mass m_h. The dark matter density and pressure are [7]

$$\rho_h = \langle v_{rh}^2 \rangle^{3/2} \frac{N_{f,b} m_h^4}{(2\pi)^{3/2} \hbar^3} \left[\frac{e^{\mu'}}{1^{3/2}} \mp \frac{e^{2\mu'}}{2^{3/2}} + \frac{e^{3\mu'}}{3^{3/2}} \mp \frac{e^{4\mu'}}{4^{3/2}} + \cdots \right], \tag{11}$$

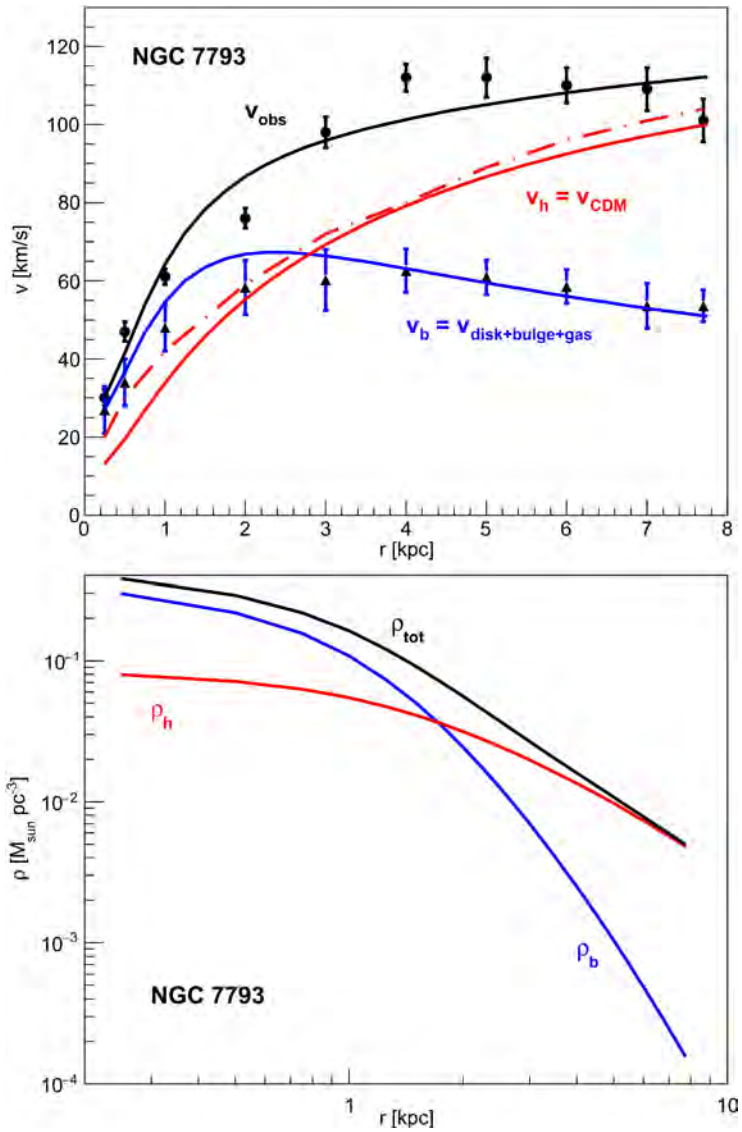

Figure 10. Top figure: Observed rotation curve $v_{obs}(r)$ (dots) and the baryon contribution $v_b(r)$ (triangles) of galaxy NGC 7793 obtained by the THINGS collaboration [1]. The "NFW, fixed" fit obtains $v_h(r)$ (dash-dotted line) [1]. The solid lines are obtained by numerical integration for non-degenerate dark matter as explained in the text. The fitted parameters are given in **Table 1**. Bottom figure: Mass densities of baryons and of dark matter of galaxy NGC 7793 obtained by numerical integration as explained in the text.

$$P_h = \left\langle v_{rh}^2 \right\rangle^{5/2} \frac{N_{f,b} m_h^4}{(2\pi)^{3/2} \hbar^3} \left[\frac{e^{\mu'}}{1^{5/2}} \mp \frac{e^{2\mu'}}{2^{5/2}} + \frac{e^{3\mu'}}{3^{5/2}} \mp \frac{e^{4\mu'}}{4^{5/2}} + \cdots \right], \tag{12}$$

where $\mu' \equiv \mu / (kT_h)$, and upper signs are for fermions, and lower signs are for bosons. μ is the chemical potential. In the course of integrating Equations (3) to (6) numerically we need to obtain $\rho_h(r)$ given $P_h(r)$ and $\left\langle v_{rh}^2 \right\rangle$. We do this by solving (12) for $e^{\mu'}$ and substituting the result in (11). We consider up to third order terms in the series of (11) and (12) until the onset of full degeneracy for fermions:

$$P_h = \rho_h^{5/3} \frac{6^{2/3} \pi^{4/3} \hbar^2}{5 N_f^{2/3} m_h^{8/3}}, \tag{13}$$

or the onset of Einstein condensation for bosons:

$$P_h = \left\langle v_{rh}^2 \right\rangle \rho_h \cdot 0.5136, \tag{14}$$

where the numerical factor is the ratio of the two series with $\mu = 0$.

For bosons $0 < e^{\mu'} < 1$. Einstein condensation sets in when $e^{\mu'}$ reaches 1. As m_h is lowered we find that $e^{\mu'}$ at $r_{\min}$ may exceed 1 indicating the onset of Einstein condensation. However the χ^2 of the fit to the galaxy rotation curves already exclude this value of m_h even when we increase the starting value of $g(r_{\min}) = -v^2 / r_{\min}$ within experimental bounds. In conclusion, the galaxy rotation curves exclude Einstein condensation in the studied galaxies.

Suppose a galaxy (not in Table 1) has a core with Einstein condensation. Let bosons in excited states fall to the ground state. The pressure will drop and hence more bosons will fall to smaller r and condense, and the process is runaway. But this condensation and collapse does not occur in the galaxies studied in this article. Einstein condensation would show up as a divergence of ρ_h as $r \to 0$ in Figure 1.

Fits to rotation curves of galaxy NGC 3198 for several values of m_h are summarized in Table 5. From this Table we conclude, with 99% confidence, that

Table 5. Fits to the rotation curves of galaxy NGC 3198 for several values of m_h to study the onset of fermion or boson degeneracy. The four fitted parameters are $\left\langle v_{rh}^2 \right\rangle'$ and $\left\langle v_{rb}^2 \right\rangle'$ defined in Equation (9), and $\rho_h(r_{\min})$ and $\rho_b(r_{\min})$. The number of degrees of freedom is 22. From this table we conclude, with 99% confidence, that $m_h > 16$ eV for fermions, and $m_h > 45$ eV for bosons. This limit for bosons sets in before Einstein condensation at $m_h = 35$ eV. $\kappa_b = 0.98$, $\kappa_h = 0.15$.

Fermions									
m_h [eV]:	500	100	30	20	17	16	15	14	13
χ^2:	8.2	8.1	10.1	9.9	12.2	19.3	30.5	44.9	61.4
Bosons									
m_h [eV]:	500	100	60	50	45	40	37	35	33
χ^2:	8.2	8.3	10.0	13.6	17.7	24.9	31.4	36.3	41.2

$m_h > 16$ eV for fermions, and $m_h > 45$ eV for bosons, if they dominate the dark matter density. Einstein condensation sets in at $m_h = 35$ eV.

As another example let us consider galaxy NGC 2403. For fermions, degeneracy sets in at $m_h \approx 40$ eV, full degeneracy begins at $m_h \approx 30$ eV, and the limit we can set based on the increase of the χ^2 of the fit by 9 units is $m_h = 18$ eV. For bosons, degeneracy sets in at $m_h \approx 50$ eV, Einstein condensation begins at $m_h = 47$ eV, and for NGC 2403 no limit on m_h can be set based on the increase of χ^2. Additional examples are presented in Table 4.

In conclusion, the observed spiral galaxy rotation curves disfavor dark matter dominated by axion-like bosons with mass less than 45 eV.

8. Measurement of the Dark Matter Particle Mass m_h

To be specific let us consider galaxy NGC 2403. The observed rotation curves of this galaxy, presented in Figure 2, are obtained with the 4 fitted parameters listed in Table 1. In particular $\left\langle v_{rh}^2 \right\rangle' = 101 \pm 3$ km/s, and $\rho_h(r_{\min}) = 0.075 \pm 0.014\, M_\odot/\mathrm{pc}^3$. Derived parameters are presented in Table 3. The mean dark matter density in the sphere of proper radius r_g is $\bar{\rho}_h = M_b \Omega_h / \left(\Omega_b 4\pi r_g^3/3\right) \approx 0.00455\, M_\odot/\mathrm{pc}^3$. We wish to relate these parameters to the primordial root-mean-square velocity of dark matter particles when perturbations were linear. We assume that dark matter particles have decoupled while still ultrarelativistic, *i.e.* have negligible interactions besides gravity. We take $\kappa_h \approx 0.15$.

A model of the hierarchical formation of galaxies is described in References [5] and [6]. Consider the expanding sphere of proper radius r_g and comoving radius r_c at time t_g containing the matter that will form galaxy NGC 2403. This sphere expands, reaches maximum expansion, and then collapses to form galaxy NGC 2403, see figure 5 of Reference [6]. We estimate the root-mean-square velocity of dark matter at time t_g, when perturbations are still linear, to be

$$v_{h\mathrm{rms}} \approx \sqrt{3} \left\langle v_{rh}^2 \right\rangle^{1/2} \left(\frac{\bar{\rho}_h}{\rho_h(r_{\min})} \right)^{1/3} \approx 63 \text{ km/s}. \tag{15}$$

The absolute velocity $v_{h\mathrm{rms}}$ has contributions from three spatial components, hence the factor $\sqrt{3}$. The last factor is a correction corresponding to adiabatic compression. According to the model of the hierarchical formation of galaxies, Equation (15) should be valid even with merging of galaxies. A correction due to mixing, expected to be of order O(1), may be needed. Extrapolating to the past, we find that the expansion parameter at which dark matter particles become non-relativistic is

$$a_{h\mathrm{NR}} \approx \frac{r_g}{r_c} \frac{v_{h\mathrm{rms}}}{c} \approx 4.1 \times 10^{-6}, \tag{16}$$

and the corresponding photon temperature is $T_0/a_{h\mathrm{NR}} \approx 57$ eV. Note that $v_{h\mathrm{rms}} \propto 1/a$ for non-relativistic particles, and the expansion parameter at time t_g is $a = r_g/r_c$. Equation (16) assumes that dark matter particles decoupled while still ultra-relativistic. To be specific, we assume that particles of mass m_h

dominate dark matter, and that these particles have $N_b = 0$ boson degrees of freedom, and $N_f = 2$ fermion degrees of freedom. The number density of dark matter particles at expansion parameter $a_{h\mathrm{NR}}$ can be calculated in two ways:

$$n_{h\mathrm{NR}} = \frac{\Omega_c \rho_{\mathrm{crit}}}{m_h a_{h\mathrm{NR}}^3} = \frac{1.20205}{\pi^2}\left(\frac{kT_{h\mathrm{NR}}}{\hbar c}\right)^3 \left\{N_b + \frac{3}{4}N_f\right\}, \tag{17}$$

where the ultra-relativistic expression to the right assumes zero chemical potential. Substituting $m_h c^2 \approx 3.15 kT_{h\mathrm{NR}}$, we obtain $m_h \approx 70$ eV. The ratio of the temperatures of dark matter and photons is $T_h/T \approx m_h/(3.15\times 57\ \mathrm{eV}) \approx 0.39$ after e^+e^- annihilation while dark matter remains ultra-relativistic. Repeating these calculations for other galaxies, and including statistical uncertainties derived from the uncertainties of the measured galaxy rotation curves, we obtain Table 6.

Note that M_b and r_g drop out of the expression for $a_{h\mathrm{NR}}$:

$$a_{h\mathrm{NR}} = \frac{\sqrt{3}\left\langle v_{rh}^2 \right\rangle^{1/2}}{c}\left[\frac{\Omega_c \rho_{\mathrm{crit}}}{\rho_h\left(r_{\min}\right)}\right]^{1/3}, \tag{18}$$

with $r_{\min} \to 0$. This equation can be understood directly: it expresses $\left\langle v_{rh}^2 \right\rangle^{1/2} \propto 1/a$, were the last factor in (18) is the "expansion parameter" in the core of the galaxy.

Table 6. Measurements of the expansion parameter $a_{h\mathrm{NR}}$ at which dark matter becomes non-relativistic (calculated with Equation (18), and the fits in Table 1). All uncertainties are statistical, 1σ. The parameter correlation coefficient −0.802 between $\left\langle v_{rh}^2 \right\rangle^{1/2}$ and $\rho_h(r_{\min})$ is taken into account. Also shown are two parameters derived from $a_{h\mathrm{NR}}$: the dark matter particle mass m_h, and the ratio of temperatures T_h/T of dark matter and photons after e^+e^- annihilation and before dark matter becomes non-relativistic. * Galaxy NGC 2841 was excluded from the average because the measurement of $\rho_h(\min)$ does not reach the core, see Figure 3. The uncertainty of the average is multiplied by $\left[\chi^2/(9-1)\right]^{1/2} = 2.17$ (as recommended in [2]).

Galaxy	$10^6 \times a_{h\mathrm{NR}}$	m_h [eV]	T_h/T
NGC 2403	4.09 ± 0.38	70.0 ± 4.9	0.387 ± 0.009
NGC 2841*	8.29 ± 0.33	41.2 ± 1.3	0.462 ± 0.006
NGC 2903	4.60 ± 0.32	64.1 ± 3.4	0.399 ± 0.008
NGC 2976	6.44 ± 2.33	49.8 ± 13.5	0.433 ± 0.039
NGC 3198	4.99 ± 0.44	60.3 ± 4.0	0.407 ± 0.010
NGC 3521	4.27 ± 0.82	67.8 ± 9.7	0.391 ± 0.019
NGC 3621	7.26 ± 0.76	45.5 ± 3.6	0.447 ± 0.012
DDO 154	2.65 ± 0.47	96.9 ± 13.0	0.347 ± 0.016
NGC 5055	3.75 ± 0.41	74.7 ± 6.1	0.379 ± 0.011
NGC 7793	3.39 ± 0.43	80.6 ± 7.6	0.369 ± 0.012
Average	4.17 ± 0.34	69.0 ± 4.2	0.389 ± 0.008

Alternatively, (18) expresses adiabatic expansion of a non-relativistic ideal "noble" gas: $T_h V^{\gamma-1}$ = constant with $\gamma = 5/3$. By "noble" we mean that collisions (if any) between dark matter particles do not excite internal degrees of freedom (if any) of these particles.

The independent measurements of m_h presented in Table 6 are fairly consistent, considering that the masses M_b of the galaxies span three orders of magnitude, and the angular momenta L_b span five orders of magnitude. The average over nine independent measurements presented in Table 6 is

$$a_{h\mathrm{NR}} = \left[4.17 \pm 0.34(\mathrm{stat})\right] \times 10^{-6}, \quad m_h = 69.0 \pm 4.2(\mathrm{stat})\ \mathrm{eV}, \tag{19}$$

and the average T_h/T, after e^+e^- annihilation while dark matter is still ultra-relativistic, is

$$T_h/T = 0.389 \pm 0.008(\mathrm{stat}), \tag{20}$$

where T is the photon temperature. Note that $m_h \propto a_{h\mathrm{NR}}^{-3/4}$ and $T_h/T \propto a_{h\mathrm{NR}}^{1/4}$, so the correlated uncertainties of m_h and T_h/T can be derived directly from the uncertainty of $a_{h\mathrm{NR}}$.

The near coincidence of the two temperatures T_h and T is evidence that dark matter was once in thermal equilibrium with the (pre?) Standard Model particles, which explains the observed Boltzmann distribution. From the preceding analysis we also conclude that dark matter decoupled while still ultra-relativistic, so scenarios with freeze-out, or freeze-in are disfavored.

Let us summarize. We assume that ultra-relativistic dark matter has zero chemical potential, and obtain, from the spiral galaxy rotation curves, a value of T_h/T that is consistent with thermal equilibrium of dark matter with the Standard Model sector at some time in the early Universe. This is a highly significant result since T depends on T_0 while T_h does not. If we would have obtained a different value of the "adiabatic invariant" $\langle v_{rh}^2 \rangle^{1/2} \rho_h (r_{\min})^{-1/3}$, we would have concluded that the chemical potential of dark matter is different from zero, and/or dark matter was never in thermal equilibrium with the Standard Model sector. So the observed adiabatic invariant is strong evidence that dark matter has zero chemical potential and was once in thermal equilibrium with the Standard Model particles.

9. Estimate of Systematic Uncertainties

The statistical uncertainties (at 68% confidence) presented so far are derived from the observational uncertainties of the galaxy rotation curves, and contributions from h and Ω_c.

The main systematic uncertainty comes from Equation (15). This Equation is justified by the model of the hierarchical formation of galaxies [5] [6], and should be valid even for merging galaxies. Never-the-less Equation (15) may require a correction due to mixing. Consider galaxy NGC 3198. The time for a particle of dark matter to traverse the radius r_g is 1.3 Gyr, so mixing due to particles entering and leaving the sphere occupied by the galaxy may be impor-

tant. At time t_g mixing can be neglected because the Universe is nearly homogeneous. Mixing during expansion and contraction can also be neglected. Most mixing occurs after the galaxy has formed. Even then, particles leaving and entering the sphere of proper radius r_g are expected to have approximately the same $\langle v_{rh}^2 \rangle$, exept for a correction due to the expansion of the Universe. So we expect the correction due to mixing to be O(1) for galaxies in a stationary state, as confirmed by the fair consistency of measurements with galaxies with masses that span three orders of magnitude, and angular momenta that span five orders of magnitude. Further study of this issue is needed.

Another correction of O(1) is due to the non-spherical symmetry of the galaxies. Yet another correction of O(1) may come from the details of the transition from ultra-relativistic to non-relativistic dark matter.

Pending detailed studies, our preliminary estimates of systematic uncertainties are:

$$a_{h\mathrm{NR}} = \left[4.17 \pm 0.34(\mathrm{stat}) \pm 2.50(\mathrm{syst})\right] \times 10^{-6}, \tag{21}$$

$$m_h = 69.0 \pm 4.2(\mathrm{stat}) \pm 31.0(\mathrm{syst})\ \mathrm{eV}, \tag{22}$$

$$T_h/T = 0.389 \pm 0.008(\mathrm{stat}) \pm 0.058(\mathrm{syst}). \tag{23}$$

Note that (22) and (23) follow directly from (21): their uncertainties are correlated. In comparison, the current uncertainty of m_h spans 70 orders of magnitude for fermions, and 90 orders of magnitude for bosons [8].

10. Thermalized Dark Matter That Decouples While Ultra-Relativistic

We consider dark matter that at some time in the history of the Universe was in thermal equilibrium with the (pre?) Standard Model particles, and decoupled from these particles and from self-annihilation while still ultra-relativistic. To be specific, we consider dark matter to be dominated by a single family of sterile Majorana neutrinos, *i.e.* $N_b = 0$ boson degrees of freedom, and $N_f = 2$ fermion degrees of freedom (for spin-up and spin-down). We also assume three families of active Majorana neutrinos with $N_f = 2$ each.

As the universe expands and cools, Standard Model particles and antiparticles that become non-relativistic annihilate heating the Standard Model sector conserving entropy, without heating sterile and active neutrinos if they have already decoupled. Table 7 presents the ratio T_h/T of dark matter-to-photon temperatures after e^+e^- annihilation while dark matter is still ultra-relativistic. Also presented is the value of m_h needed to obtain the measured Ω_c. We note that the measured T_h/T (23) and measured m_h (22) are consistent with decoupling at temperatures higher than approximately m_μ.

For example, assume the decoupling temperature is in the range m_b to m_W. Then T_h/T is calculated as follows:

$$\frac{T_h}{T} = \left(\frac{4 \times 43}{11 \times 345}\right)^{1/3} = 0.357. \tag{24}$$

Table 7. We consider dark matter that was once in thermal equilibrium with the (pre?) Standard Model particles and then decoupled from these particles in the indicated temperature range. We assume no self-annihilation. T_h/T is the ratio of dark matter temperature to photon temperature after e^+e^- annihilation while dark matter remains ultra-relativistic. m_h is the mass of particles of dark matter needed to obtain the observed Ω_c. Case $N_b = 0$, $N_f = 2$.

Decoupling temperature range	T_h/T in range m_h to m_e	m_h
m_H to m_t	0.344	99.9 ± 3.1 eV
m_W to m_H	0.345	98.9 ± 3.1 eV
m_b to m_W	0.357	89.5 ± 2.8 eV
m_τ to m_b	0.372	78.6 ± 2.5 eV
m_c to m_τ	0.378	75.0 ± 2.4 eV
m_s to m_c	0.399	64.1 ± 2.0 eV
m_e to m_μ	0.714	11.2 ± 0.4 eV

These numbers can be found in the Table in Section 21.3.2 of [2]. At the time of Big Bang Nucleosynthesis (BBN), *i.e.* $T \approx 1$ MeV, neutrinos with, for example, $m_h = 89.5 \pm 2.8$ eV are still ultra-relativistic. The density of radiation at the time of BBN increases by a factor

$$\frac{2+\frac{7}{8}6\left(\frac{4}{11}\right)^{4/3}+\frac{7}{8}2\left(\frac{4\times 43}{11\times 345}\right)^{4/3}}{2+\frac{7}{8}6\left(\frac{4}{11}\right)^{4/3}} = \frac{3.391}{3.363} = 1.0084, \tag{25}$$

due to one family of sterile Majorana neutrinos. Equivalently, the effective number of light neutrinos increases from $N_\nu = 3$ to 3.062, well within BBN experimental bounds, *i.e.* $N_\nu \lesssim 4$ [2].

An example of a sterile neutrino dark matter candidate is presented in **Figure 11**. The figure was obtained by integrating the corresponding Boltzmann equation for the generation of sterile Majorana neutrinos since Electroweak Symmetry Breaking (when active Majorana neutrinos acquire a Dirac mass and therefore sterile Majorana neutrinos couple to the Standard Model). **Figure 11** also shows a brief history of the Universe.

11. Dark Matter-Baryon Cross-Section

Consider a hydrogen atom, or a proton, of mass m_p, in a circular orbit of velocity V_b within the core of a galaxy. The velocity V_b will decay with a relative rate $\tau_b^{-1} \equiv dV_b/(V_b \cdot dt) \approx \rho_h \sigma_{hb} V_b / m_p$ due to collisions with dark matter particles with cross-section σ_{hb}. Taking τ_b equal to the age of the universe, $V_b \approx 150$ km/s, and $\rho_h \approx 0.2\, M_\odot/\text{pc}^3$ (see **Table 1**), we obtain

$$\sigma_{hb} \lesssim 2\times 10^{-26}\ \text{cm}^2, \tag{26}$$

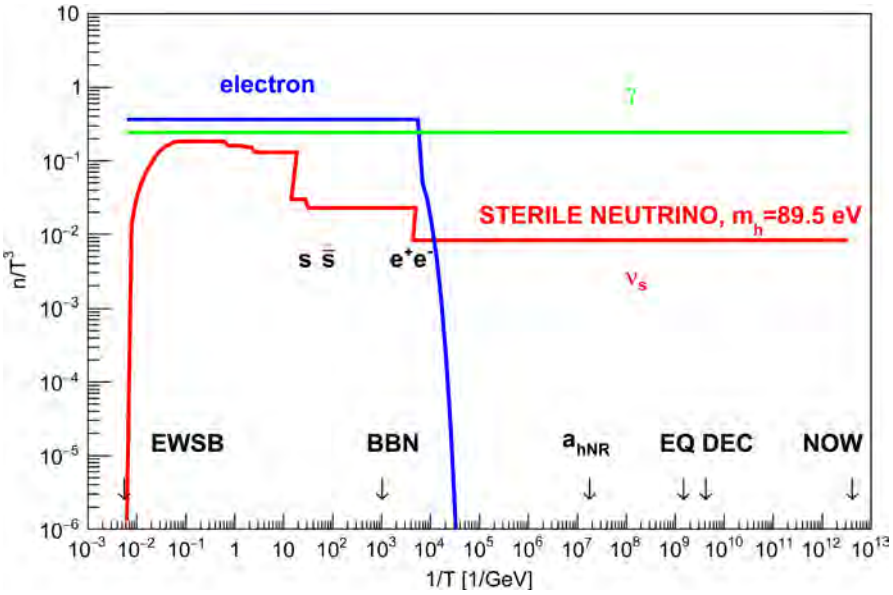

Figure 11. Plotted are the number density n of photons, electrons, and dark matter particles, divided by T^3, as a function of $1/T$, where T is the photon temperature. In this example, the dark matter is dominated by one Majorana sterile neutrino type (two degrees of freedom: spin up, and spin down) with $m_s = 89.5$ eV, produced since Electroweak Symmetry Breaking (EWSB) at $T = 159 \pm 1$ GeV. The corresponding active neutrino flavor in this example has $m_a = 1 \times 10^{-9}$ eV, but this value is not critical. The sterile neutrino in this example enters thermal equilibrium at $T \approx 53$ GeV, and leaves thermal contact at $T \approx 6$ GeV. The mass $m_s = 89.5$ eV is chosen to obtain the observed Ω_c. This solution is consistent with Big Bang Nucleosynthesis. The lifetime of this sterile neutrino is 7×10^{27} years.

independently of m_h.

The mean time between collisions of a dark matter particle with baryons is $\tau_h \approx m_p \Big/ \left(\rho_b \sigma_{hb} \sqrt{3} \left\langle v_{rh}^2 \right\rangle^{1/2} \right)$. Dark matter is not in thermal equilibrium with baryons so τ_h is larger than the age of the universe. With data of galaxy NGC 2841 we obtain

$$\sigma_{hb} \lesssim 2 \times 10^{-26} \text{ cm}^2. \tag{27}$$

These limits are useful for dark matter masses m_h below the reach of direct or indirect searches, e.g. $m_h < 50$ keV. Planed direct low mass WIMP searches with the NEWS-SNO project will reach dark matter masses ≈ 0.1 GeV [2]. No searches in the $m_h = 100$ eV range are mentioned in the Dark Matter review of Reference [2], but ideas to reach the MeV to meV mass scales are mentioned.

12. The Core

The mean baryon density of the universe is $6.2 \times 10^{-9} \, M_\odot / \text{pc}^3$, while the baryon density in the core of galaxy NGC 2403 is $0.3 M_\odot / \text{pc}^3$, so matter has collapsed by a factor 5×10^7 in this case. What prevented $\rho_h(r)$ or $\rho_b(r)$ from collapsing all the way to ∞ as $r \to 0$? In **Figures 1-10** we see no increase of $\rho_h(r)$ or $\rho_b(r)$ as $r \to 0$ down to the first measured point at $r_{\min}$. Why a

core instead of a cusp? The four parameters $\rho_h(r_{\min})$, $\rho_b(r_{\min})$, $\langle v_{rh}^2 \rangle'$, and $\langle v_{rb}^2 \rangle'$ can fit any core radius. So, what determines these four boundary conditions?

Possibilities to consider are Bose-Einstein of Fermi-Dirac degeneracy? (the observed galaxy rotation curves obtain m_h at the edge of degeneracy as shown in Section 7), dark matter or baryon crossing time?, non-spherical initial density perturbations?, angular momentum of the primordial rotation field?, dominance of baryons in the core?, ongoing collapse of the core? (however baryons are already supported by the centrifugal force as shown in Section 4), etc.

In **Figures 1-10** we observe that the baryon core radius, the radius r_{ed} of equal densities, and the dark matter core radius are similar, and increase in this order. We also observe that the baryon density dominates at small radii. These observations suggest that baryons radiate energy conserving angular momentum, fall to the galactic plane, acquire increasingly circular orbits, until baryons are supported by the centrifugal force with $\kappa_b \to 1$. Thereafter baryons can fall no further. For example, a proton or hydrogen atom falling into the galaxy collides with other baryons, falls to the disk and acquires circular velocity $\sqrt{\kappa_b}v$. Once the central gravitational potential is determined mostly by baryons, dark matter rests in this given potential.

Note that as $r \to \infty$, $\rho_h \to v^2/(4\pi G r^2)$ with $v^2 = 2\langle v_{rh}^2 \rangle'$. Note that (18) obtains $\rho_h(0)$ given $\langle v_{rh}^2 \rangle$ and $a_{h\text{NR}}$, and therefore constrains the dark matter core radius.

13. Angular Momentum

The suggestion is that the primordial angular momentum in the sphere of proper radius r_g and comoving radius r_c during the expansion phase at time t_g is the same as the angular momentum $L = L_b(\Omega_c + \Omega_b)/\Omega_b$ of the galaxy with L_b listed in **Table 4**, *i.e.* the angular momentum of the galaxy is conserved and may be of cosmological origin.

Perturbations of density, gravitational potential, and velocity in the non-relativistic universe dominated by dark matter have four independent modes [9]: a scalar growing mode, a scalar decaying mode, and two vector modes with transverse velocity ($\boldsymbol{q} \cdot \delta \boldsymbol{v}_{\boldsymbol{q}} = 0$ in Fourier space) that conserve angular momentum, *i.e.* $\delta \boldsymbol{v}_{\boldsymbol{q}} \propto 1/a$. The velocity field of these vector modes is measured by the galaxy angular momenta listed in **Table 4** if they are of cosmological origin.

14. Structure Formation

Most dark matter should have been non-relativistic at the time when there was a galactic mass inside the horizon [2]. From this criterion we have estimated $m_h \gtrsim 1.3$ keV for unsuppressed formation of galaxies with total (baryonic plus dark) mass as low as $10^8 M_\odot$ [10]. On the other hand, simulations of the Cold Dark Matter scenario produce many more dwarf galaxies than observed [11].

At an expansion parameter $a_{h\text{NR}} \approx 4.2 \times 10^{-6}$, when dark matter with mass

$m_h \approx 69$ eV becomes non-relativistic, the universe is still dominated by radiation, see Figure 11. The age of the universe is $t = a_{h\mathrm{NR}}^2 \big/ \left(2H_0\sqrt{\Omega_r}\right)$, the distance to the horizon is $l = 2ct$, and the mass of baryons inside the horizon is $M_b \approx 20\times 10^{10} M_\odot$, comparable to large galaxies in Table 3. Smaller size perturbations are suppressed, so we may have a problem understanding the formation of galaxies with $M_b < 20\times 10^{10} M_\odot$.

Note that protons are non-relativistic when the smallest observed galaxies and globular clusters enter the horizon. Compared to the cold dark matter scenario with $m_h \gg 5$ keV, for $m_h = 69$ eV the power spectrum of density fluctuations on scales smaller than $M_b = 20\times 10^{10} M_\odot$ becomes suppressed. If the dark matter inside the horizon becomes nearly homogeneous while ultra-relativistic (as expected), then the suppression factor is $\Omega_b \big/ \left(\Omega_b + \Omega_c\right) \approx 0.16$ assuming adiabatic initial conditions.

The hierarchical formation of galaxies is shown in figure 6 of Reference [6]. Suppose that only the small scale perturbations are suppressed by a factor 0.16. Since some galaxies with $M_b \approx 20\times 10^{10} M_\odot$ have formed, other perturbations on this scale are on the verge of formation, and hence even low amplitude small scale perturbations can collapse and form a small galaxy or globular cluster. This observation may address the "missing satellite problem" [11]. A dedicated study of this issue is needed.

Dark matter with mass ≈ 69 eV also has tension with studies of the power spectra of density perturbations on scales less than 10 h^{-1} Mpc with the "Lyman-alpha forest" [12]. These studies set lower bounds on dark matter mass of ≈ 4 keV for early decoupled thermal relics. So we have tension between these two measurements which needs further study. Note however that 69 eV is near the limit of the reach of the Lyman-alpha forest study [12].

15. Conclusions

We conclude that the rotation curves of regular spiral galaxies are described, within observational uncertainties, by Equations (3) to (6). These equations describe the stationary state of two self-gravitating non-relativistic ideal gases, "baryons" and "dark matter", that do not interact significantly with each other except for gravity. These equations can be integrated numerically given four parameters (that are boundary conditions). These four parameters are obtained by minimizing a χ^2 between the measured and calculated spiral galaxy rotation curves.

From these studies, we obtain a wide range of quantitative results on the physics of galaxies, dark matter, and cosmology. In particular, we have presented precision measurements of the dark matter mass m_h and temperature $T_h(a)$.

The most significant result is the ratio of the temperatures of dark matter and photons after e^+e^- annihilation while dark matter is still ultra-relativistic:

$$T_h/T = 0.389 \pm 0.008(\mathrm{stat}) \pm 0.058(\mathrm{syst}). \tag{28}$$

The plausibility that this result is correct lies in the consistency of nine com-

plete and independent measurements of the mass m_h of particles of dark matter with spiral galaxies that span three orders of magnitude in mass, and five orders of magnitude in angular momentum. The ratio (28) could have been orders of magnitude larger than, or smaller than, unity, because T depends on T_0, while T_h is independent of T_0. The ratio T_h/T depends on the measured adiabatic invariant $\langle v_{rh}^2 \rangle^{1/2} \rho_h (r_{\min})^{-1/3}$, so this analysis provides evidence that dark matter was once in thermal equilibrium with the (pre?) Standard Model particles. It is therefore likely that dark matter particles will have one of the precise masses listed in Table 7 (or in its extensions for other N_b or N_f). The decoupling of dark matter from the Standard Model sector at temperatures higher than m_μ allows us to follow the Boltzmann distribution of these particles all the way from primordial times into the cores of spiral galaxies. An integration of the Boltzmann equation for the production of sterile Majorana neutrinos after Electroweak Symmetry Breaking shows consistency with these results, see Figure 11. Such sterile Majorana neutrinos evade all current dark matter searches.

The present studies pose new questions. Why is the spiral galaxy core radius similar in galaxies that span three orders of magnitude in mass? It seems likely that this core radius is of cosmological origin. In fact Equation (18) is already a constraint. It also seems likely that the angular momentum of spiral galaxies is of cosmological origin. Studies of angular momentum correlation between galaxies should settle this issue. If the angular momenta are cosmological, we have a handle on the amplitude of the primordial vector modes. The importance of this avenue of research lies in the fact that the velocities of these vector modes grow towards the past conserving angular momentum and hence could dominate the origin of the Universe.

Conflicts of Interest

The author declares no conflicts of interest regarding the publication of this paper.

References

[1] de Blok, W.J.G., *et al.* (2008) High-Resolution Rotation Curves and Galaxy Mass Models from THINGS. *The Astronomical Journal*, **136**, 2648-2719.

[2] Tanabashi, M., *et al.* (Particle Data Group) (2018) The Review of Particle Physics. *Physical Review D*, **98**, Article ID: 030001.

[3] Begeman, K. (1987) HI Rotation Curves of Spiral Galaxies. PhD Thesis, University of Groningen, Groningen.

[4] Navarro, J.F., Frenk, C.S. and White, S.D.M. (1996) The Structure of Cold Dark Matter Halos. *ApJ*, **462**, 563.
Navarro, J.F., Frenk, C.S. and White, S.D.M. (1997) A Universal Density Profile from Hierarchical Clustering. *ApJ*, **490**, 493.

[5] Hoeneisen, B. (2000) A Simple Model of the Hierarchical Formation of Galaxies. arXiv:astro-ph/0009071.

[6] Hoeneisen, B. (2018) Study of Galaxy Distributions with SDSS DR14 Data and Measurement of Neutrino Masses. *International Journal of Astronomy and Astrophysics*, **8**, 230-257. https://doi.org/10.4236/ijaa.2018.83017

[7] Hoeneisen, B. (1993) Thermal Physics. Mellen Research University Press, San Francisco.

[8] Profumo, S. (2017) Particle Dark Matter. World Scientific, Singapore.

[9] Weinberg, S. (2008) Cosmology. Oxford University Press, Oxford.

[10] Hoeneisen, B. (2015) Trying to Understand Dark Matter. arXiv:1502.07375

[11] Klypin, A.A., Kravtsov, A.V., Valenzuela, O. and Prada, F. (1999) Where Are the Missing Galactic Satellites? *Astrophysical Journal*, **522**, 8292. https://doi.org/10.1086/307643

[12] Baur, J., Palanque-Delabrouille, N., Yche, C., Magneville, C. and Viel, M. (2016) Lyman-Alpha Forests Cool Warm Dark Matter. *Journal of Cosmology and Astroparticle Physics*, No. 8, Article ID: 012. https://doi.org/10.1088/1475-7516/2016/08/012

Scientific Research Publishing

International Journal of Astronomy and Astrophysics, 2019, 9, 97-114
http://www.scirp.org/journal/ijaa
ISSN Online: 2161-4725
ISSN Print: 2161-4717

Extraction of the Speed of Gravity (Light) from Gravity Observations Only

Espen Gaarder Haug

Norway Norwegian University of Life Sciences, Ås, Norway
Email: espenhaug@mac.com

How to cite this paper: Haug, E.G. (2019) Extraction of the Speed of Gravity (Light) from Gravity Observations Only. *International Journal of Astronomy and Astrophysics*, **9**, 97-114.
https://doi.org/10.4236/ijaa.2019.92008

Received: February 25, 2019
Accepted: May 6, 2019
Published: May 9, 2019

Abstract

We show how one can measure the speed of gravity only using gravitational phenomena. Our approach offers several ways to measure the speed of gravity (light) and checks existing assumptions about light (gravity) in new types of experiments. The speed of light is included in several well-known gravitational formulas. However, if we can measure this speed from gravitational phenomena alone, then is it the speed of light or the speed of gravity we are measuring? We think it is more than a mere coincidence that they are the same. In addition, even if it is not possible to draw strong conclusions now, our formulations support the view that there is a link between electromagnetism and gravity. This paper also shows that all major gravity phenomena can be predicted from only performing two to three light observations. There is no need for knowledge of Newton's gravitational constant G or the mass size to complete a series of major gravity predictions.

Keywords

Speed of Gravity, Speed of Light, Redshift, Gravitational Time Dilation, Schwarzschild Radius, Gravity Predictions from Light Only

1. Introduction

In 1890, Maurice Lévy [1] suggested that the speed of gravity is equal to the speed of light. Poincaré [2] argued in 1904 that the speed of gravity could not be larger than the speed of light in vacuum. The speed of gravity in Einstein's general relativity theory [3] is assumed to be the same as the speed of light [4] [5]. Still, there exist a series of alternative gravity theories assuming that the speed of gravity is much greater than the speed of light, see, for example, [6] [7] [8] [9] for such models and discussion on them. To measure the speed of gravity is therefore of great importance to find out which theories can be ruled out and

which ones are worth exploring further [10] [11].

There have been several indirect detections of the speed of gravity in the past. For example, [12], based on information from a rather complex set-up including quasar observations, concluded that the speed of gravity c_{gw} was between 0.8 and 1.2 times the speed of light in vacuum. In more recent times, advanced experimental studies in relation to gravity waves claim to support the idea that the speed of gravity is in the ball park of the speed of light in a vacuum [13] [14] [15]. Clearly, these measurements give a very wide confidence interval for the speed of gravity, something to which we return later in this paper. These experiments are based on very complex set-ups and also, we would say, a complex set of assumptions.

This paper will show how we can extract the speed of gravity (light) from a series of simple gravity observations. The approach explained is much simpler conceptually and experimentally than gravity wave experiments. Our theory also supports the concept that gravity is moving at the speed of light, and the experiments suggested will likely give a very narrow confidence interval for the speed of gravity. It can be questioned if we are finding the speed of light or the speed of gravity in our method. Alternatively, they could perhaps be the same, if electromagnetism and gravity at a deeper level are connected, as they could be in a yet-to-be discovered unified theory. This will be discussed briefly in Section 6 of this paper.

2. Extracting the Speed of Gravity (Light)—The Simple Way

The speed of light is an input factor in several gravity formulas, such as the calculation for the Schwarzschild radius

$$r_s = \frac{2GM}{c^2} \tag{1}$$

The formula can also be found from Newton's gravity theory [16] by setting the radius equal to the point where Newton's escape velocity is the speed of light[1]. In addition, it can be derived from Einstein's theory of general relativity [3] in combination with the Schwarzschild metric [17] [18] because the escape velocity there supposedly is the same [19]. In 1784, Michell first calculated what radius would give an escape velocity equal to the speed of light, see [20]. He also hypothesized that the star would be dark. General relativity has a different interpretation and a much wider theory on these objects, which are seen as black holes in that context. We will not discuss black holes versus dark stars and the possibilities of such objects, but it is important to keep in mind that when we talk about the Schwarzschild radius here, it is also linked to Newton's gravity theory, since the same radius can be calculated from that theory.

Further, the Schwarzschild radius is related to gravitational time dilation (gra-

[1]We will claim that the Newton method, as typically used, is not that sound because it involves a kinetic energy formula of the form $\frac{1}{2}mv^2$ in the derivation. This formula is clearly only valid when $v \ll c$.

vitational time dilation was first suggested by Einstein)

$$\frac{T_h}{T_L}=\frac{\sqrt{1-\frac{r_s}{R_h}}}{\sqrt{1-\frac{r_s}{R_L}}}=\frac{\sqrt{1-\frac{v_{e,h}^2}{c^2}}}{\sqrt{1-\frac{v_{e,L}^2}{c^2}}} \tag{2}$$

where T_h is the time as measured at a radius of R_h, T_L is the time measured at a radius of R_L from the center of the gravitational object $\left(R_h > R_L\right)$, and $v_{e,L}$ and $v_{e,h}$ are the escape velocities at the two different altitudes. In other words, the speed of light is input from several gravitational phenomena that have been confirmed by observations. However, to our knowledge little has been written about working the calculation the other way around, namely using gravitational observations to measure the speed of light. This is also interesting from a fundamental point of view. Why can we find the speed of light, as we will show, simply by observing gravitational phenomena? In undertaking this exploration, we will gain some insight into how the gravity formulas were derived in the first place.

2.1. Speed of Gravity/Light from a Gravitational Red-Shift Experiment

If we shoot a laser beam of light from the top of a tower to the bottom of the tower, we can measure the redshift, with respective radii of R_h and R_L to the center of the Earth. The gravitational redshift is then given by

$$\frac{\overline{\lambda}_h-\overline{\lambda}_L}{\overline{\lambda}_L}=\frac{\sqrt{1-\frac{v_{e,h}^2}{c^2}}}{\sqrt{1-\frac{v_{e,L}^2}{c^2}}}-1=\frac{\sqrt{1-\frac{2v_{o,h}^2}{c^2}}}{\sqrt{1-\frac{2v_{o,L}^2}{c^2}}}-1 \tag{3}$$

where v_e and v_o are the escape velocity and the orbital velocity at these two radii, and λ_L and λ_h are the wavelengths at the two altitudes. Solved with respect to c, this gives

$$c=\frac{\sqrt{2\lambda_h^2v_{o,L}^2-2\lambda_L^2v_{o,h}^2}}{\sqrt{\lambda_h^2-\lambda_L^2}} \tag{4}$$

In a weak gravitational field, $v_o \ll c$ and this can be well-approximated as

$$\frac{\lambda_h-\lambda_L}{\lambda_L}\approx\frac{1-\frac{1}{2}\frac{2v_{o,h}^2}{c^2}}{1-\frac{\frac{1}{2}2v_{o,L}^2}{c^2}}-1 \tag{5}$$

Solved with respect to c, this gives

$$c\approx\frac{\sqrt{\lambda_hv_{o,L}^2-\lambda_Lv_{o,h}^2}}{\sqrt{\lambda_h-\lambda_L}} \tag{6}$$

And since $g = \frac{v_o^2}{R}$, we can also find the speed of the light from measuring the gravitational acceleration at the two altitudes instead of using the orbital velocities; this gives

$$c = \frac{\sqrt{2\lambda_h^2 g_L R_L - \lambda_L^2 g_h R_h}}{\sqrt{\lambda_h^2 - \lambda_L^2}} \tag{7}$$

We can also do the weak field approximation

$$c \approx \frac{\sqrt{\lambda_h g_L R_L - \lambda_L g_h R_h}}{\sqrt{\lambda_h - \lambda_L}} \tag{8}$$

If the redshift is measured from two altitudes on Earth, then the gravitational acceleration field is naturally preferable. But we could also send a laser beam between two satellites orbiting the Earth at different altitudes and then we could just as well use the orbital velocities.

2.2. Speed of Gravity from Orbital Velocity and Two Atomic Clocks

If we have two atomic clocks sitting at different altitudes, then we have

$$\frac{T_h}{T_L} = \frac{\sqrt{1 - \frac{r_s}{R_h}}}{\sqrt{1 - \frac{r_s}{R_L}}} \tag{9}$$

$$\frac{T_h}{T_L} = \frac{\sqrt{1 - \frac{gR}{c^2}}}{\sqrt{1 - \frac{gR}{c^2}}} \tag{10}$$

Solved with respect to the speed of light, we get

$$\frac{T_h}{T_L} = \frac{\sqrt{1 - \frac{\frac{2GM}{c^2}}{R_h}}}{\sqrt{1 - \frac{\frac{2GM}{c^2}}{R_L}}}$$

$$\frac{T_h^2}{T_L^2} = \frac{1 - \frac{\frac{2GM}{c^2}}{R_h}}{1 - \frac{\frac{2GM}{c^2}}{R_L}}$$

$$\frac{T_h^2}{T_L^2} = \frac{c^2 - \frac{2GM}{R_h}}{c^2 - \frac{2GM}{R_L}}$$

$$T_h^2c^2-\frac{2GM}{R_L}T_h^2=T_L^2c^2-\frac{2GM}{R_h}T_L^2$$

$$T_h^2c^2-T_L^2c^2=\frac{2GM}{R_L}T_h^2-\frac{2GM}{R_h}T_L^2$$

$$c=\frac{\sqrt{2v_{o,L}^2T_h^2-2v_{o,h}^2T_L^2}}{\sqrt{T_h^2-T_L^2}} \tag{11}$$

Obviously the Earth is rotating, so if the work is not done at the poles then we must take the different rotational speeds of the Earth at different altitudes into account (see [21] for an introduction on the topic). Therefore, we have

$$\frac{T_h}{T_L}=\frac{\sqrt{1-\frac{r_s}{R_h}-\frac{v_{o,h}^2}{c^2}}}{\sqrt{1-\frac{r_s}{R_L}-\frac{v_{o,L}^2}{c^2}}} \tag{12}$$

Solved with respect to the speed of light, we have

$$c=\frac{\sqrt{T_L^2v_h^2-T_h^2v_L^2}}{\sqrt{T_L^2-T_h^2+2v_L^2T_h^2-2v_h^2T_L^2}} \tag{13}$$

Table 1 below summarizes ways to extract the speed of light (gravity) from gravitational observations alone.

Figure 1 illustrates some of the ways we can find the speed of gravity (or just light) by only doing gravity observations. In Figure 1(a), we have two orbiting satellites, we send light between them and measure the redshift. In addition, we measure the orbital velocity of the satellites and from this we know the speed of light. In Figure 1(b), we measure the gravitational time dilation at two altitudes, as well as the Earth's gravitational acceleration field at each altitude, and from

Table 1. Ways to measure (extract) the speed of light/gravity from gravitational observations.

	Prediction	Easily applicable in practice?
From redshift and orbital velocity	$c=\frac{\sqrt{2\lambda_h^2v_{o,L}^2-2\lambda_L^2v_{o,h}^2}}{\sqrt{\lambda_h^2-\lambda_L^2}}$	Easy enough
From redshift and acceleration field	$c=\frac{\sqrt{2\lambda_h^2g_LR_L-2\lambda_L^2g_hR_h}}{\sqrt{\lambda_h^2-\lambda_L^2}}$	Easy enough
Atomic clocks + orbital velocity	$c=\frac{\sqrt{2v_{o,L}^2T_h^2-2v_{o,h}^2T_L^2}}{\sqrt{T_h^2-T_L^2}}$	Does not take rotation of Earth into account
Atomic clocks + acceleration field	$c=\frac{\sqrt{2g_LR_LT_h^2-2g_hR_hT_L^2}}{\sqrt{T_h^2-T_L^2}}$	Does not take rotation of Earth into account
Atomic clocks + orbital velocity	$c=\frac{\sqrt{T_L^2v_{o,h}^2-T_h^2v_{o,L}^2}}{\sqrt{T_L^2-T_h^2+2v_{o,L}^2T_h^2-2v_{o,h}^2T_L^2}}$	Easy enough

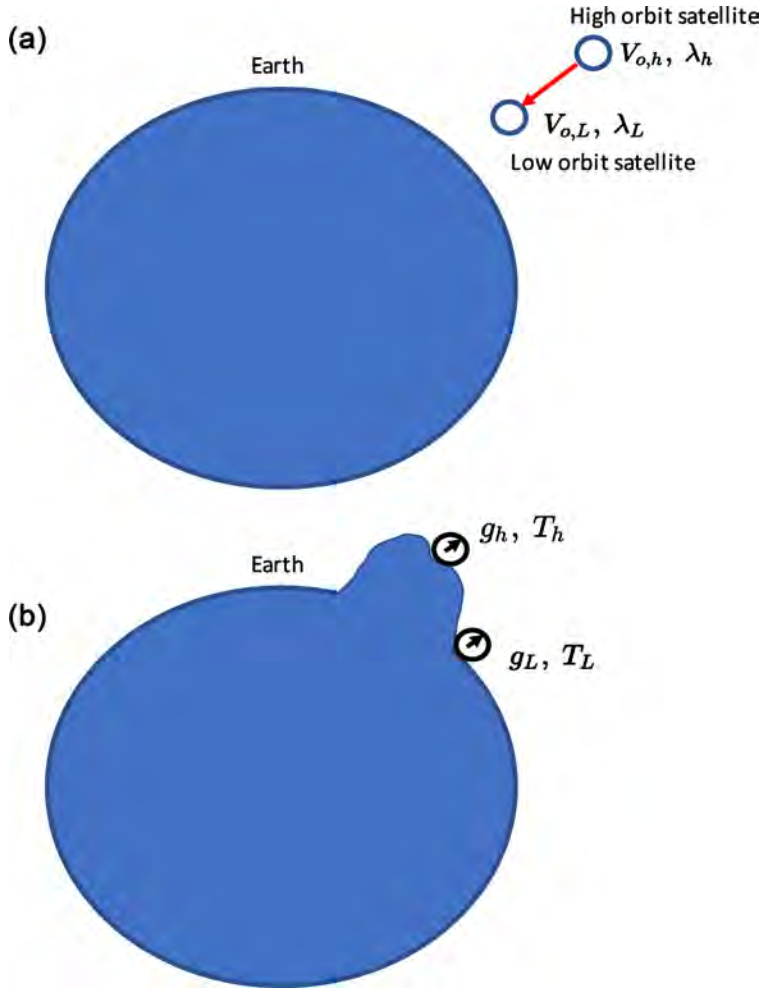

Figure 1. Illustrations of two set-ups where we can measure the speed of light only from gravity observations. In the figure, we also see what observations need to be done at each location.

this we know the speed of light (gravity).

3. No Need to Know G or the Mass Size or Even the Speed of Light to Find the Schwarzschild Radius and to Predict Other Gravity Phenomena

The past scientific literature does not seem to mention the fact that one can easily find the Schwarzschild radius (for example of the Earth) without any prior knowledge of the Newton gravitational constant or any knowledge of the mass size. This can be done by using the following relation

$$r_s = 2g_L \frac{R_L^2}{c^2} \tag{14}$$

where g_L is the gravitational acceleration that on Earth's surface can be observed with no knowledge of gravitational theory. Further, the speed of light and the radius of the Earth can be found without any knowledge of gravitational theory. We have found that a long series of gravitational phenomena can be pre-

dicted when one first has found the Schwarzschild radius without knowledge of G or the mass size, as clearly shown by [22] [23].

Interestingly, we can even find (measure) the Schwarzschild radius by replacing the speed of light with our extracted speed of light, as shown in the sections above. The Schwarzschild radius can be found based on the following formula

$$r_s = 2g_L \frac{R_L^2}{c^2}$$

$$r_s = 2g_L \frac{R_L^2}{\frac{2\lambda_h^2 g_L R_L - 2\lambda_L^2 g_h R_h}{\lambda_h^2 - \lambda_L^2}}$$

$$r_s = \frac{2R_L^2\left(\lambda_h^2 - \lambda_L^2\right)}{2\lambda_h^2 R_L - 2\lambda_L^2 R_h \frac{g_h}{g_L}}$$

$$r_s = \frac{R_L^2\left(\lambda_h - \lambda_L\right)}{\lambda_h R_L - \lambda_L R_h \frac{R_L^2}{R_h^2}}$$

$$r_s = \frac{\lambda_h^2 - \lambda_L^2}{\frac{\lambda_h^2}{R_L} - \frac{\lambda_L^2}{R_h}}$$

$$r_s = \frac{R_L R_h\left(\lambda_h^2 - \lambda_L^2\right)}{\lambda_h^2 R_h - \lambda_L^2 R_L} \tag{15}$$

where λ_L and λ_h are the wavelengths of a light beam moving out from or towards Earth, as measured from radius R_L and R_h respectively (where $R_h > R_L$). In other words, it is directly linked to the gravitational redshift of light. For example, one can measure the wavelength of a light beam at the top of a tower (tall building) and the bottom of a tower (see Pound and Rebka Jr. [24]). This is all that is needed to know the Schwarzschild radius of the Earth. The important point is that we can extract the Schwarzschild radius without the Newton gravitational constant and with no knowledge of the speed of light (gravity) or the mass size. All we need to know is the gravitational redshift at two points. Thus we may question if the Schwarzschild radius really is a radius related to black holes, or if it represents something more profound and linked to all (or most) gravity phenomena.

Table 2 shows how a series of major gravity phenomena can be predicted simply from two observations of a light beam plus a measurement of the speed of light. This is done by measuring the wavelength of two distant points and knowing the radii where the measurements are taken relative to the gravity object (for example the Earth). This seems to provide a clear proof that gravity is directly linked to light and therefore, the speed of gravity must be exactly the speed of light.

General relativity theory has not been able to link its theory to quantum physics;

Table 2. The table shows that all major gravity phenomena can be predicted by only two (or three) observations from a light beam in the gravitational field of the gravity object. We need to measure the wavelength at two altitudes of a light beam plus the speed of light. There is no need to know the Newton gravitational constant or the mass of the gravity object. This also strongly supports the ideas that there is a direct connection between electromagnetism and gravity and that the speed of gravity is actually the speed of light. The radius R is where we want to perform the gravity prediction, and R_L and R_h are the radii where we perform the wavelength (or frequency) observations.

What to measure or predict	Formula	How	Is it easy to do?	Knowledge of G or M
Exact solution (strong and weak fields):				
Schwarzschild radius	$r_s = \frac{R_L R_h \left(\lambda_h^2 - \lambda_L^2\right)}{\lambda_h^2 R_h - \lambda_L^2 R_L}$	Light observations only	Yes	No
Gravitational acceleration	$g = \frac{1}{2}\frac{R_L R_h \left(\lambda_h^2 - \lambda_L^2\right)}{\lambda_h^2 R_h - \lambda_L^2 R_L}\frac{c^2}{R^2}$	Light observations only	Yes	No
Orbital velocity	$v_o = c\sqrt{\frac{1}{2}\frac{R_L R_h \left(\lambda_h^2 - \lambda_L^2\right)}{\lambda_h^2 R_h - \lambda_L^2 R_L}\frac{1}{R}}$	Light observations only	Yes	No
Escape velocity	$v_e = c\sqrt{\frac{R_L R_h \left(\lambda_h^2 - \lambda_L^2\right)}{\lambda_h^2 R_h - \lambda_L^2 R_L}\frac{1}{R}}$	Light observations only	Yes	No
Time dilation	$t_2 = t_1\sqrt{1 - \frac{R_L R_h \left(\lambda_h^2 - \lambda_L^2\right)}{\lambda_h^2 R_h - \lambda_L^2 R_L}\frac{1}{R}}$	Light observations only	Yes	No
GR bending of light	$\delta = \frac{2R_L R_h \left(\lambda_h^2 - \lambda_L^2\right)}{\lambda_h^2 R_h - \lambda_L^2 R_L}\frac{1}{R}$	Light observations only	Yes	No
Gravitational redshift	$\lim_{R_h \to \infty} z(R_L) = \frac{1}{2}\frac{R_L R_h \left(\lambda_h^2 - \lambda_L^2\right)}{\lambda_h^2 R_h - \lambda_L^2 R_L}\frac{1}{R}$	Light observations only	Yes	No
Weak field approximations:				
Schwarzschild radius	$r_s = \frac{2R_L R_h \left(\lambda_h - \lambda_L\right)}{\lambda_h R_h - \lambda_L R_L}$	Light observations only	Yes	No
Gravitational acceleration	$g = \frac{R_L R_h \left(\lambda_h - \lambda_L\right)}{\lambda_h R_h - \lambda_L R_L}\frac{c^2}{R^2}$	Light observations only	Yes	No
Orbital velocity	$v_o = c\sqrt{\frac{R_L R_h \left(\lambda_h - \lambda_L\right)}{\lambda_h R_h - \lambda_L R_L}\frac{1}{R}}$	Light observations only	Yes	No
Escape velocity	$v_e = c\sqrt{\frac{2R_L R_h \left(\lambda_h - \lambda_L\right)}{\lambda_h R_h - \lambda_L R_L}\frac{1}{R}}$	Light observations only	Yes	No
Time dilation	$t_2 = t_1\sqrt{1 - \frac{2R_L R_h \left(\lambda_h - \lambda_L\right)}{\lambda_h R_h - \lambda_L R_L}\frac{1}{R}}$	Light observations only	Yes	No
GR bending of light	$\delta = 4\frac{R_L R_h \left(\lambda_h - \lambda_L\right)}{\lambda_h R_h - \lambda_L R_L}\frac{1}{R}$	Light observations only	Yes	No
Gravitational redshift	$\lim_{R_h \to \infty} z(R) = \frac{R_L R_h \left(\lambda_h - \lambda_L\right)}{\lambda_h R_h - \lambda_L R_L}\frac{1}{R}$	Light observations only	Yes	No

in spite of many efforts in the physics world, a unified theory is still missing. We think the Schwarzschild radius plays an important role in gravity, but that it is related to some quite different aspects of matter than those assumed by standard theory. The Schwarzschild radius is, in our view, the reduced Compton frequency per Planck

second multiplied by the Planck length, that is $r_s = \frac{2GM}{c^2} = 2\frac{\frac{c}{\bar{\lambda}}}{\frac{c}{l_p}} l_p = 2l_p \frac{l_p}{\bar{\lambda}}$, be aware that both l_p and $\bar{\lambda}$ can be measured independent of GR and without any knowledge of big *G*, see [25] [26]. For any known elementary particle, such as the electron, the reduced Compton wavelength is much larger than the Planck length. We will suggest that this means the Schwarzschild radius for particles with mass smaller than the Planck mass should be interpreted as a probabilistic Schwarzschild radius. In our view, all elementary particles have a Schwarzschild radius equal to the Planck length, but this comes in and out of existence at the Compton frequency of the particle. This means the Schwarzschild radius of an elementary particle smaller than the Planck mass simply is the Planck length multiplied by a probability that is given by: $\frac{l_p}{\bar{\lambda}}$. So, the Schwarzschild radius is twice the Planck length multiplied by this probability.

When $\bar{\lambda}$ is smaller than the Planck length, something we claim only can happen for a composite mass, then we will have $\frac{l_p}{\bar{\lambda}} > 1$; the integer part of this number means certainty, that is the number of whole Planck length, while the remaining fraction should be viewed as a probability. Here the Schwarzschild radius holds from the smallest elementary particle, such as an electron, to the largest mass. Particles with a Schwarzschild radius smaller than the Planck length simply means the Schwarzschild radius comes in and out of existence. We do not think there exists an physical Compton wavelength shorter than the Planck length, but the Compton wavelength from different particles can be added, based on the following rule, $\bar{\lambda} = \frac{\hbar}{\sum_{i=1}^{N} m_i c} = \frac{1}{\frac{1}{\bar{\lambda}_i} + \frac{1}{\bar{\lambda}_{i+1}} + \frac{1}{\bar{\lambda}_n}}$, something that means any mass has a Compton wavelength, even if a composite particle does not have one physical Compton wavelength, but many. Still, the Compton wavelength of the composite mass will lead to the correct Compton frequency. Further, recent research seems to directly link matter to Compton time, see [27] [28].

In our view, the Schwarzschild radius itself can never be smaller than the Planck length; a smaller radius, as is the case for any observed elementary particle, does not mean such particles do not have a Schwarzschild radius, it means their Schwarzschild radius comes in and out of existence and that gravity is probabilistic below the Planck mass scale. That is to say, probability should be dominant in gravity for masses much smaller than the Planck mass, which would hold for all observed elementary particles.

4. When Using Gravity Observations (Only) Are We Measuring the Speed of Light or the Speed of Gravity?

We have shown a series of ways to extract the speed of gravity from observations

normally only linked to gravity. But is it "just" the speed of light we can extract in this way? If we claim it is the speed of light we are extracting and not the speed of gravity, then why should the speed of light be hidden in a series of gravity phenomena such as time dilation and gravitational acceleration fields, as well as gravitational redshift? Doesn't this indicate that electromagnetism is linked to gravity? Or we could claim it is only the speed of gravity we have extracted, as it is only from gravity phenomena. It does appear that the speed of light and the speed of gravity are one and the same thing, and align with the case where, at a deeper level, we expect to find a unification of electromagnetism and gravity; this is obviously an old, but ongoing debate [29]-[35]. We would strongly suggest that such unification of electromagnetism and gravity is also observable at the macroscopic scale, not only at the quantum scale. There are many opinions here and we will not draw conclusions prematurely, but encourage more physicists to study this, both theoretically and experimentally.

It is well known that the Coulomb electrostatic force [36] and the Newton gravity force theoretically are the same for Planck mass particles, $F = k_e \frac{q_p q_p}{R^2} = G\frac{m_p m_p}{R^2} = \frac{\hbar c}{R^2}$, where q_p and m_p are the Planck charge and the Planck mass, see also [37]. Is it not a bit strange that the speed of light suddenly shows up in Newton's gravity theory when working at the Planck scale and otherwise it is assumed by many physicists that Newtonian gravity is instantaneous? We know the speed of light is linked to the Coulomb electrostatic force as $k_e = c^2 \times 10^{-7}$. Recently, it has also been suggested that the speed of light is embedded in Newton's gravitational constant. Haug has [38] [39] [40] suggested that Newton's gravitational constant is a composite constant $G = \frac{l_p^2 c^3}{\hbar}$. McCulloch [41] [42] has suggested $G = \frac{\hbar c}{m_p^2}$, which basically is identical to our composite gravity constant, but he has pointed out that this leads to a circular problem, as he has followed the common assumptions in modern physics on this point, e.g., that one needs to know G to know m_p and that his composite G then cannot be known without G. We, on the other hand, have shown that the Planck length can be found with no knowledge of G, see [25] [26] [43]. Then all the parts of this composite constant can be found independent of existing gravity theories. If this view is correct, then the speed of light, which likely is the same as the speed of gravity, is embedded in almost all gravity phenomena and it is not surprising that we can extract the speed of gravity from a series of gravity phenomena, without detecting gravity waves, and in a much simpler way. The Planck length is something we logically can relate to—it is a minimum length. The speed of light is how fast the fastest particle (photons) can move, and it is the longest distance something can travel in any given time interval. The gravitational constant, on the other hand, does not seem to correspond to anything logically or physically, as its dimensions are $m^3 \cdot kg^{-1} \cdot s^{-2}$. Newton's gravitational constant is clearly

a universal constant, but in our view, it is a composite constant that consists of more fundamental constants. In particular, we think the Planck length and the speed of light (gravity) are essential for all gravity phenomena, even at the cosmological scale.

We are in no way indicating that Newton had any idea that gravity moved at the speed of light; the speed of gravity is often assumed to be infinite in Newtonian theory. But the speed of gravity in that theory is not truly reflected in the formula. It is indeed the lack of any speed in Newton's gravity formula and Newton's speculations that gravity was infinite that led many others to think it must be infinite. Newton's gravity formula is simply $F = \frac{Mm}{R^2}$. To get it to fit experiments, the formula had to be calibrated, that is, one had to introduce an unknown parameter, today know as big G (or simply the Newton gravity constant). The gravity constant is today experimentally found from what we can call gravitational model calibration. What exactly the gravity constant represents is diffuse, at best. If the speed of gravity plays a central role in all gravity phenomena, then it must be embedded in the Newton formula, even if it simply is as part of a composite constant calibrated to observations. If not, Newton would not have been able to predict the simplest gravity phenomena accurately. The fact that Newton theory does not predict the perihelion of Mercury correctly could simply be due to relativistic effects that not have been taken into account properly, see [44] for a recent discussion on this.

In 1798, the gravity constant was first measured indirectly when Cavendish wanted to weight the Earth with a torsion balance. And it was likely first in 1873 that the Newton gravity constant was mentioned explicitly by Cornu and Baille [45]. Again, it is still a mystery what the gravity constant truly represents. However, returning to recent measurements of the speed of gravity, based on the recent gravitational wave detection Cornish, Blas, and Nardini [14] claim

> "using a Bayesian approach that combines the first three gravitational wave detections reported by the LIGO Scientific and Virgo Collaborations we constrain the gravitational waves propagation speed c_{gw} to the 90% credible interval $0.55c < c_{gw} < 1.42c$, where c is the speed of light in vacuum."

we are not questioning their measurements or predictions here, but it also interesting if we can measure the speed of gravity in a much simpler way using the methodology suggested in this paper.

5. Isotropic or Anisotropic?

It has been suggested that the speed of gravity could be anisotropic [46]. It is therefore of interest to know if our extraction of the speed of gravity (light) from the experiments suggested in this paper could be helpful in this respect. To discuss this, we will address an old and ongoing debate related to the question of whether the one-way speed of light is isotropic or anisotropic. The idea that the one-way speed of light is constant and the same in every direction, e.g., isotropic,

was likely first introduced by Poincaré. In the year of 1898, Poincaré [47] published a philosophical paper titled: *The Measure of Time*. In this article, Poincaré points to how astronomers often assume the speed of light is constant and the same in every direction:

> When a astronomer tells me that a stellar phenomenon, which his telescope reveals to him at this moment, happened, nevertheless, fifty years ago, I seek his meaning, and to that end I shall ask him first how he knows it, that is, how he had measured the velocity of light.
> He has begun by supposing that light has a constant velocity, and in particular that its velocity is the same in all directions. That is a postulate without which no measurement of this velocity could be attempted. This postulate could never be verified by direct experiment.

Poincaré here indicates that it would be impossible to detect the true one-way speed of light in any type of experiment. The problem with this method is that to measure the one-way speed of light, we need to synchronize two clocks, and to synchronize two clocks we need to know the one-way speed of light. We end up with a circular problem. This is likely the reason Poincaré assumed that we could never measure the one-way speed of light and thereby assumed that the one-way speed of light was isotropic for synchronization purposes. In 1905, Einstein [48] goes one step further and simply abandons the ether and by this he also assumes that the one-way speed of light is isotropic. It can also be shown that slow clock transportation synchronization basically corresponds to Einsten-Poincaré synchronization, so this synchronization procedure cannot, in general, be used to set up experiments to detect the one-way speed of light, see [49] [50].

However, it is worth mentioning that a series of experiments have attempted to circumvent the Einstein-Poincaré synchronization procedure in order to detect whether the one-way speed of light is isotropic or anisotropic. A series of experiments have claimed to have detected anisotropic one-way speed of light, see [51]-[57], but many of these experiments have also been criticized, see, for example, [58] [59]. The debate around the one-way speed of light continues to this day [60] [61] [62] [63] and it also remains an open question whether the one-way speed of gravity is isotropic or anisotropic as well.

When it comes to our extraction of the speed of gravity (light) from gravity observations, these often involve two very precise clocks, atomic or optical clocks placed a distance apart. These clocks need to be synchronized, which intuitively suggest that our methods cannot be used to detect if the speed of gravity (light) is isotropic or anisotropic. On the other hand, in experiments where we only need to detect the redshift, then no clock synchronization should be necessary and this could possibly be used to measure the one-way speed of light (gravity). The main challenge would be to attain the degree of accuracy required, as we would also need to measure the gravitational acceleration at each altitude.

If it is the speed of gravity we actually are extracting and not only the speed of light, then the approaches in this paper are still very interesting. This means one

does not need to rely on very sophisticated theories, such as gravity waves detectors, to detect the speed of gravity, but instead we can use much simpler experiments. However, if this is not giving us the speed of gravity, then we need good arguments to address why the speed of light is hidden in so many gravitational phenomena and how we can predict all major gravity phenomena, such as orbital velocity, gravitational time dilation, gravitational acceleration, and the Schwarzschild radius, all without any knowledge of G, c, or the gravity mass, but simply from a beam of light in the gravity field.

6. Conclusions

We have shown how one can, in a simple way, extract the speed of light (gravity) from gravitational observations alone. Even if it only seems to consist of a rearrangement of existing formulas, the exercise and analysis can lead to new insights. We would note some things are so simple that they seem obvious when first pointed out, but they may have deeper implications and certainly deserve further examination.

It is, at present, an open question on whether or not there is a link between gravity and electromagnetism, and there is a renewed interest in the link between the two. We have shown how a series of major gravity phenomena can be predicted by some simple observations of a light beam, namely its velocity and its wavelength at two altitudes in a gravitational field. This may provide a small breakthrough in the current insights around gravity. A unified theory between electromagnetism and gravity is still missing, but hopefully this takes us one step further in the right direction.

Acknowledgements

Thanks to Victoria Terces for helping me edit this manuscript and thanks to an anonymous referee for useful comments.

Conflicts of Interest

The author declares no conflicts of interest regarding the publication of this paper.

References

[1] Lévy, M. (1890) Sur l'application des lois électrodynamiques au mouvement des planétes. *Comptes Rendus des Séances de l'Académie des Sciences. Paris*, **110**, 545-551.

[2] Poincaré, H. (1904) L'état actuel et l'avenir de la physique mathématique. *Bulletin des Sciences Mathématiques*, **28**, 302-324.

[3] Einstein, A. (1916) Näherungsweise integration der feldgleichungen der gravitation. Sitzungsberichte der Königlich Preussischen Akademie der Wissenschaften, Berlin.

[4] Salisbury, W.W. (1969) Velocity of Gravitational Waves. *Nature*, **224**, 782-783. https://doi.org/10.1038/224782a0

[5] Krasnikov, S. (2011) The Speed of Gravity in General Relativity. *Gravitation and*

Cosmology, **17**, 194-197. https://doi.org/10.1134/S0202289311020150

[6] De Felice, A., Hindmarsh, M. and Trodden, M. (2006) Ghosts, Instabilities, and Superluminal Propagation in Modified Gravity Models. *Journal of Cosmology and Astroparticle Physics*, **2006**. https://doi.org/10.1088/1475-7516/2006/08/005

[7] Yahalom, A. (2013) Gravity and Faster than Light Particles. *Journal of Modern Physics*, **4**, 1412-1416. https://doi.org/10.4236/jmp.2013.410169

[8] Moffat, J.W. (2014) Superluminal Gravitational Waves. arXiv:1406.2609

[9] Krasnikov, S. (2014) What Is Faster—Light or Gravity? *Classical and Quantum Gravity*, **32**, Article ID: 075002. https://doi.org/10.1088/0264-9381/32/7/075002

[10] Gong, Y. and Papantonopoulos, E. (2018) Constraints on Scalar-Tensor Theory of Gravity by the Recent Observational Results on Gravitational Waves. *The European Physical Journal C*, **78**, 738. https://doi.org/10.1140/epjc/s10052-018-6227-9

[11] Nersisyan, H., Lima, N.A. and Amendola, L. (2018) Gravitational Wave Speed: Implications for Models without a Mass Scale. arXiv:1801.06683

[12] Kopeikin, S.M. and Fomalont, E.B. (2006) Aberration and the Fundamental Speed of Gravity in the Jovian Deflection Experiment. *Foundations of Physics*, **36**, 1244-1285. https://doi.org/10.1007/s10701-006-9059-7

[13] Du, S., Peng, F. and Li, M. (2017) Measuring the Speed of Gravitational Waves with the Distorted Pulsars. arXiv:1712.05965

[14] Cornish, N., Blas, D. and Nardini, G. (2017) Bounding the Speed of Gravity with Gravitational Wave Observations. *Physical Review Letters*, **119**, Article ID: 161102. https://doi.org/10.1103/PhysRevLett.119.161102

[15] Tattersall, O.J., Ferreira, P.G. and Lagos, M. (2018) Speed of Gravitational Waves and Black Hole Hair. *Physical Review D*, **97**, Article ID: 084005. https://doi.org/10.1103/PhysRevD.97.084005

[16] Newton, I. (1686) Philosophiae Naturalis Principia Mathematica. London. https://doi.org/10.5479/sil.52126.39088015628399

[17] Schwarzschild, K. (1916) Über das gravitationsfeld eines massenpunktes nach der Einsteinschen theorie. Sitzungsberichte der Deutschen Akademie der Wissenschaften zu Berlin, Klasse fur Mathematik, Physik, und Technik, 189.

[18] Schwarzschild, K. (1916) Über das gravitationsfeld einer kugel aus inkompressibler flussigkeit nach der Einsteinschen theorie. Sitzungsberichte der Deutschen Akademie der Wissenschaften zu Berlin, Klasse fur Mathematik, Physik, und Technik, 424.

[19] Augousti, A.T. and Radosz, A. (2006) An Observation on the Congruence of the Escape Velocity in Classical Mechanics and General Relativity in a Schwarzschild Metric. *European Journal of Physics*, **27**, 331-335. https://doi.org/10.1088/0143-0807/27/2/015

[20] Michell, J. (1784) On the Means of Discovering the Distance, Magnitude &c.of the Fixed Stars, in Consequence of the Diminution of the Velocity of Their Light, in Case Such a Diminution Should Be Found to Take Place in Any of Them, and Such Other Data Should Be Procured from Observations. *Philosophical Transactions of the Royal Society*, **74**. https://doi.org/10.1098/rstl.1784.0008

[21] Grøn, Ø. (2009) Lecture Notes on the General Theory of Relativity. Springer Verlag, Berlin. https://doi.org/10.1007/978-0-387-88134-8

[22] Haug, E.G. (2018) Gravity without Newton's Gravitational Constant and No Knowledge of Mass Size. *Preprints*, **2018**, Article ID: 2018080220

[23] Haug, E.G. (2018) A New Mass Measure and a Simplification of Modern Physics That Make Gravity Predictions Independent of G. *Preprints*, **2019**, Article ID: 2019020032. https://www.preprints.org/manuscript/201902.0032/v1 https://doi.org/10.20944/preprints201902.0032.v1

[24] Pound, R.V. and Rebka Jr., G.A. (1959) Gravitational Redshift in Nuclear Resonance. *Physical Review Letters*, **3**, 439-441. https://doi.org/10.1103/PhysRevLett.3.439

[25] Haug, E.G. (2017) Can the Planck Length Be Found Independent of Big G? *Applied Physics Research*, **9**, 58-66. https://doi.org/10.5539/apr.v9n6p58

[26] Haug, E.G. (2018) Finding the Planck Length Independent of Newton's Gravitational Constant and the Planck Constant: The Compton Clock Model of Matter. *Preprints*, **2018**, Article ID: 2018090396. https://www.preprints.org/manuscript/201809.0396/v1 https://doi.org/10.20944/preprints201809.0396.v1

[27] Lan, S., Kuan, P., Estey, B., English, D., Brown, J.M., Hohensee, M.A. and Müller, H. (2013) A Clock Directly Linking Time to a Particle's Mass. *Science*, **339**, 554-557. https://doi.org/10.1126/science.1230767

[28] Dolce, D. and Perali, A. (2015) On the Compton Clock and the Undulatory Nature of Particle Mass in Graphene Systems. *The European Physical Journal Plus*, **130**, 41. https://doi.org/10.1140/epjp/i2015-15041-5

[29] Reichenbächer, E. (1917) Grundzüge zu einer Theorie der Elektrizität und der Gravitation. *Annalen der Physik*, **357**, 134-173. https://doi.org/10.1002/andp.19173570203

[30] Coley, A. (1984) A Note on the Geometric Unification of Gravity and Electromagnetism. *General Relativity and Gravitation*, **16**, 459-464. https://doi.org/10.1007/BF00762338

[31] Schütze, D. (1985) On Unifying Electromagnetism and Gravitation without Curvature. *Journal of Mathematical Physics*, **26**, 2596. https://doi.org/10.1063/1.526725

[32] Magnon, A. (1992) Ashtekar Variables and Unification of Gravitational and Electromagnetic Interactions. *Classical and Quantum Gravity*, **9**, S169.

[33] Füzfa, A. (2016) How Current Loops and Solenoids Curve Spacetime. *Physical Review D*, **93**, Article ID: 024014. https://doi.org/10.1103/PhysRevD.93.024014

[34] Li, L.X. (2016) A New Unified Theory of Electromagnetic and Gravitational Interactions. *Frontiers of Physics*, **11**, Article ID: 110402. https://doi.org/10.1007/s11467-016-0588-z

[35] Zheng-Johansson, J.X. (2018) A Theory of Gravity and General Relativity Based on Quantum Electromagnetism. *Journal of Physics*: *Conference Series*, **965**, Article ID: 012043. https://doi.org/10.1088/1742-6596/965/1/012043

[36] Coulomb, C.A. (1785) Premier mémoire sur l'électricité et le magnétisme. *Histoire de l'Académie Royale des Sciences*, 569-577.

[37] Stenger, V. (2014) Myths of Physics: 2. Gravity Is Much Weaker than Electromagnetism. Huffington Post, Blog by Victor Stenger.

[38] Haug, E.G. (2016) The Gravitational Constant and the Planck Units. A Simplification of the Quantum Realm. *Physics Essays*, **29**, 558-561. https://doi.org/10.4006/0836-1398-29.4.558

[39] Haug, E.G. (2016) Planck Quantization of Newton and Einstein Gravitation. *International Journal of Astronomy and Astrophysics*, **6**, 206-217. https://doi.org/10.4236/ijaa.2016.62017

[40] Haug, E.G. (2018) Newton's and Einstein's Gravity in a New Perspective for Planck

Masses and Smaller Sized Objects. *International Journal of Astronomy and Astrophysics*, **8**, 6-23. https://doi.org/10.4236/ijaa.2018.81002

[41] McCulloch, M.E. (2014) Gravity from the Uncertainty Principle. *Astrophysics and Space Science*, **349**, 957-959. https://doi.org/10.1007/s10509-013-1686-9

[42] McCulloch, M.E. (2016) Quantised Inertia from Relativity and the Uncertainty Principle. *EPL* (*Europhysics Letters*), **115**, Article ID: 69001. https://doi.org/10.1209/0295-5075/115/69001

[43] Haug, E.G. (2018) Planck Mass Measured Totally Independent of Big *G* Utilising McCulloch-Heisenberg Newtonian Equivalent Gravity. *Preprints*, **2018**, Article ID: 2018060391.

[44] Haug, E.G. (2018) Relativistic Newtonian Gravitation That Gives the Correct Prediction of Mercury Precession and Needs Less Matter for Galaxy Rotation Observations. http://vixra.org/pdf/1808.0679v2.pdf

[45] Cornu, A. and Baille, J.B. (1873) Détermination nouvelle de la constante de l'attraction et de la densité moyenne de la terre. *Comptes Rendus Mathematique Academie des Sciences*, *Paris*, **76**, 954-955.

[46] Tso, R., Isi, M., Chen, Y. and Stein, L. (2017) Modeling the Dispersion and Polarization Content of Gravitational Waves for Tests of General Relativity. *Proceedings of the 7th Meeting on CPT and Lorentz Symmetry*, 205-208. https://doi.org/10.1142/9789813148505_0052

[47] Poincaré, H. (1898) The Measure of Time. English Translation by George Bruce Halsted 1913 in the Foundation of Science.

[48] Einstein, A. (1905) On the Electrodynamics of Moving Bodies. *Annalen der Physik*, **17**, 891-921.

[49] Lévy, J. (2003) From Galileo to Lorentz and Beyond. Apeiron.

[50] Haug, E.G. (2014) Unified Revolution, New Fundamental Physics. E.G.H. Publishing, Oslo.

[51] Marinov, S. (1974) The Velocity of Light Is Direction Dependent. *Czechoslovak Journal of Physics B*, **24**, 965-970. https://doi.org/10.1007/BF01591047

[52] Marinov, S. (1980) Measurement of the Laboratory's Absolute Velocity. *General Relativity and Gravitation*, **12**, 57-66. https://doi.org/10.1007/BF00756168

[53] Torr, D.G. and Kolen, P. (1984) An Experiment to Measure Relative Variations in the One-Way Speed of Light. In: Taylor, B.N. and Phillips, W.D., Eds., *Precision Measurements and Fundamental Constants II*, Special Publication, 617, 675-679.

[54] Silvertooth, E.W. (1986) Special Relativity. *Nature*, **322**, 590. https://doi.org/10.1038/322590b0

[55] Monstein, C. and Wesley, J.P. (1996) Solar System Velocity from Muon Flux Anisotropy. *Apeiron*, **30**, 33-37.

[56] Cahill, R.T. (2006) The Roland de Witte 1991 Experiment (to the Memory of Roland de Witte). *Progress in Physics*, **3**, 60-65.

[57] Cahill, R.T. (2012) One-Way Speed of Light Measurements without Clock Synchronization. *Progress in Physics*, **3**, 43-45.

[58] Prokhovnik, S.J. (1979) The Empty Ghosts of Michelson and Morley: A Critique of the Marinov Coupled-Mirrors Experiment. *Foundations of Physics*, **9**, 883-896. https://doi.org/10.1007/BF00708698

[59] Spavieri, C., Quintero, J., Unnikrishnan, C.S., Gilles, G., Cavalleri, G., Tonni, E. and Bosi, L. (2012) Can the One-Way Speed of Light Be Used for Detection of Viola-

tions of the Relativity Principle? *Physics Letters A*, **376**, 795-797. https://doi.org/10.1016/j.physleta.2012.01.010

[60] (2010) A View from Emerging Technology from the arXiv. The One-Way Speed of Light Conundrum. *MIT Technology Review*.

[61] Pérez, I. (2011) On the Experimental Determination of the One-Way Speed of Light. *European Journal of Physics*, **32**, 993. https://doi.org/10.1088/0143-0807/32/4/013

[62] Spavieri, G., Rodriguez, M. and Sánchez, A. (2018) Thought Experiment Discriminating Special Relativity from Preferred Frame Theories. *Journal of Physics Communications*, **2**, Article ID: 085009. https://doi.org/10.1088/2399-6528/aad5fa

[63] Spavieri, G. and Haug, E.G. (2018) Why the Sagnac Effect Favors Absolute over Relative Simultaneity. Submitted to journal, under consideration.

Appendix

In this appendix, we show the cases where we want to measure/predict the gravitational phenomena at one of the same radii from which we measured the wavelength of the beam; see Table 3.

Table 3. The table shows that all major gravity phenomena can be predicted by only two (or three) observations from a light beam in the gravitational field of the gravity object. We need to measure the wavelength at two altitudes of a light beam plus the speed of light. There is no need to know the Newton gravitational constant or the mass of the gravity object. This also strongly supports the ideas that there is a direct connection between electromagnetism and gravity and that the speed of gravity is actually the speed of light.

What to measure or predict	Formula	How	Is it easy to do?	Knowledge of G or M
Exact solution (strong and weak fields):				
Schwarzschild radius	$r_s = \frac{R_L R_h \left(\lambda_h^2 - \lambda_L^2\right)}{\lambda_h^2 R_h - \lambda_L^2 R_L}$	Light observations only	Yes	No
Gravitational acceleration	$g_L = \frac{1}{2}\frac{c^2 R_h \left(\lambda_h^2 - \lambda_L^2\right)}{\lambda_h^2 R_h R_L - \lambda_L^2 R_L^2}$	Light observations only	Yes	No
Gravitational acceleration	$g_h = \frac{1}{2}\frac{c^2 R_L \left(\lambda_h^2 - \lambda_L^2\right)}{\lambda_h^2 R_h^2 - \lambda_L^2 R_L R_h}$	Light observations only	Yes	No
Orbital velocity	$v_{o,L} = c\sqrt{\frac{1}{2}\frac{R_h \left(\lambda_h^2 - \lambda_L^2\right)}{\lambda_h^2 R_h - \lambda_L^2 R_L}}$	Light observations only	Yes	No
Orbital velocity	$v_{o,h} = c\sqrt{\frac{1}{2}\frac{c^2 R_L \left(\lambda_h^2 - \lambda_L^2\right)}{\lambda_h^2 R_h - \lambda_L^2 R_L}}$	Light observations only	Yes	No
Escape velocity	$v_{e,L} = c\sqrt{\frac{R_h \left(\lambda_h^2 - \lambda_L^2\right)}{\lambda_h^2 R_h - \lambda_L^2 R_L}}$	Light observations only	Yes	No
Escape velocity	$v_{e,h} = c\sqrt{\frac{R_L \left(\lambda_h^2 - \lambda_L^2\right)}{\lambda_h^2 R_h - \lambda_L^2 R_L}}$	Light observations only	Yes	No
Time dilation	$t_2 = t_1\sqrt{1 - \frac{R_h \left(\lambda_h^2 - \lambda_L^2\right)}{\lambda_h^2 R_h - \lambda_L^2 R_L}}$	Light observations only	Yes	No
GR bending of light	$\delta_L = 2\frac{R_h \left(\lambda_h^2 - \lambda_L^2\right)}{\lambda_h^2 R_h - \lambda_L^2 R_L}$	Light observations only	Yes	No
GR bending of light	$\delta_h = 2\frac{R_L \left(\lambda_h^2 - \lambda_L^2\right)}{\lambda_h^2 R_h - \lambda_L^2 R_L}$	Light observations only	Yes	No
Gravitational redshift	$\lim_{R_h \to \infty} z\left(R_L\right) = \frac{1}{2}\frac{R_h \left(\lambda_h^2 - \lambda_L^2\right)}{\lambda_h^2 R_h - \lambda_L^2 R_L}$	Light observations only	Yes	No
Gravitational redshift	$\lim_{R_h \to \infty} z\left(R_h\right) = \frac{1}{2}\frac{R_L \left(\lambda_h^2 - \lambda_L^2\right)}{\lambda_h^2 R_h - \lambda_L^2 R_L}$	Light observations only	Yes	No

International Journal of Astronomy and Astrophysics, 2019, 9, 115-132
http://www.scirp.org/journal/ijaa
ISSN Online: 2161-4725
ISSN Print: 2161-4717

Quantum Distribution Functions for Dusty Plasma in Saturn's Rings by Using Curvilinear Coordinates

Nagat Abd El Rahman Hussein[1], Abd El-Rahim Hassan Ahmed[2], Esraa Gamal Sayed[1*]

[1]Mathematics Department, Faculty of Science, Assiut University, Assiut, Egypt
[2]Mathematics Department, Faculty of Science, Al-Azhar University, Assiut, Egypt
Email: *aragamal@yahoo.com

How to cite this paper: Hussein, N.A. El R., Ahmed, A.El-R.H. and Sayed, E.G. (2019) Quantum Distribution Functions for Dusty Plasma in Saturn's Rings by Using Curvilinear Coordinates. *International Journal of Astronomy and Astrophysics*, **9**, 115-132.
https://doi.org/10.4236/ijaa.2019.92009

Received: February 13, 2019
Accepted: May 26, 2019
Published: May 29, 2019

Abstract

This study aims to estimate the quantum Bogoliubov-Born-Green-Kirkwood-Yvon (BBGKY) hierarchy in curvilinear coordinates. We used the results to calculate the quantum binary and triplet distribution functions in curvilinear coordinates. The analytical form of the quantum distribution functions was obtained for dusty plasma in Saturn's rings model. We use particles-in-cell (PIC) simulations to find a visualization of dusty three-component plasma phase space in curvilinear coordinates. Our results were compared with others.

Keywords

Dusty Plasma, Binary and Triplet Distribution Functions, Three Component Plasma, BBGKY Hierarchy

1. Introduction

The quantum distribution functions are of great interest for understanding the properties of dusty plasma. In statistical mechanics, we can get the thermodynamic functions such as the internal energy, the osmotic pressure, and the excess free energy by using the distribution functions for the plasma particles. The importance of quantum distribution function in statistical physics is to give the particles number density in the phase space at time t.

Many authors have calculated the quantum distribution functions. Hussein and Hassan [1] have calculated the quantum binary distribution of high temperature plasma. Kraeft *et al.* [2] used effective potentials to calculate the binary distribution function. Bogoliubov and Kraeft *et al.* [3] [4] defined a set of equations describing the dynamics of a system of a large number of interacting par-

ticles by using the quantum BBGKY hierarchy. Kaniadakis [5] showed that the classical BBGKY hierarchical equation, for the n-particle reduced distribution function. Fesciyan [6] calculated the quantum time independent BBGKY hierarchy of equations at low densities. Hussein *et al.* [7] used the BBGKY hierarchy for calculating the binary and triplet distribution functions for one- and two-component Plasmas in terms of Green's function technique. A quantum mechanical calculation of the radial distribution function for a Plasma was given by [8]. Also, many others have studied the binary and triplet distribution functions [9]-[19]. Many researchers have been interested in identifying the optimal form of the classical distribution functions [16]. Hansen [17] calculated the distribution functions for one component plasma in the classical form and quantum corrections.

The calculation of the distribution functions in general form by using curvilinear coordinates makes it easier for the researchers to find the form of the distribution function in the spherical or cylindrical coordinates or any type of coordinates that facilitates the study of the physical problem. Błaszak and Domanski [20] calculated the canonical quantization of classical mechanics in curvilinear coordinates. Kjaergaard and Mortensen in 1990 [21] made a simple derivation of the quantum mechanical Hamiltonian in curvilinear coordinates. In 2012 a generalized, curvilinear-coordinate formulation of Poisson's equations to solve for the electrostatic fields in plasma was given by Fichtl *et al.* [22].

Dusty Plasmas plays an important role in experimental physics and in many astrophysical situations [23]. To understand many space and astrophysical phenomena, and many industrial and physical applications, the study of plasmas containing heavy dust particles is very important [24]. It differs from ordinary plasma in the presence of dust particles along with a number of positive and negative charges moving at a high speed if compared with the speed of dust [25]. Wang and Zhang [26] employed the quantum hydrodynamic model to study the solution and chaotic structures of dust ion-acoustic waves in quantum dusty plasmas consisting of electrons, ions and charged dust particles.

Dusty plasma was originally important in the field of astrophysics. Examples of astronomical dusty plasmas include planetary ring systems (rings of Saturn). The rings of Saturn are the most important models in space dusty plasma study [27]. The rings of Saturn are made of billions of particles; these particles mostly range from tiny, dust-sized icy grains to giant chunks. They are made of small chunks of ice and rock coated with another material such as dust. A few particles are as large as mountains.

Saturn's ring system extends up to 175,000 miles (282,000 kilometres) from the planet, yet the vertical height is typically about 30 feet (10 meters) in the main rings [28]. Named alphabetically in the order they were discovered, the rings are relatively close to each other, with the exception of a gap measuring 2920 miles (4700 kilometres) wide called the Cassini Division that separates Rings A and B. The main rings are A, B and C. Rings D, E, F and G are fainter and more recently discovered; each ring orbits at a different speed around the

planet [29]. But if we ask a question why plasma molecules move in these rings in circular paths and what is the nature of their components. And how to find the distribution functions of their particles. Does the use of curvilinear coordinates make it easier to find and deal with the functions of predisposition? In this study, we attempted to find the form of the distribution functions of the molecules of planetary rings. A model was found that simulates its shape. How fast the particles of planetary rings and whether it is necessary to use Einstein patches for high speeds. In this research, we tried to answer some of these questions.

Particle-in-cell (PIC) simulations are a useful tool in modelling plasma. The electron velocity distribution function and the plasma potential are found by particle-in-cell (PIC) simulations [30]. Reinmüller in 1998 [31] determined the plasma potential from PIC simulations. We use particle-in-cell (PIC) simulations to find a visualization of dusty three component plasma quantum phase space in curvilinear coordinates.

This work is aimed to calculate the quantum binary and triplet distribution functions of a dusty plasma in curvilinear coordinates. In geometry, curvilinear coordinates are a coordinate system for Euclidean space in which the coordinate lines may be curved. Commonly used curvilinear coordinate systems include rectangular, spherical, and cylindrical coordinate systems. The calculation is based on the Bogoliubov-Born-Green-Kirkwood-Yvon (BBGKY) hierarchy [3].

The cluster expansion method consists of writing the binary distribution function as a power series in the density. The coefficients of different powers of the density involve integrals of the order of that power. These coefficients are then expressed as a sum of a product of integrals. The power series of the binary distribution function in the density convergence badly at high densities, many attempts have been made to overcome such difficulty.

2. The Basic Equations and Hierarchy

Consider 3 Dimensions space with coordinates $X=\left(x_1,x_2,x_3\right)$. A point p in 3d space can be defined using Cartesian coordinates or it can also be defined by its curvilinear coordinates $\xi=\left(\xi_1,\xi_2,\xi_3\right)$. The relation between the coordinates is then given by the invertible transformation functions:

$$\xi_s=\xi_s\left(x_1,x_2,x_3\right),\ s=1,2,3$$

$$x_i=x_i\left(\xi_1,\xi_2,\xi_3\right),\ i=1,2,3 \tag{1}$$

The surfaces ξ_1 = constant, ξ_2 = constant, ξ_3 = constant are called the coordinate surfaces. The coordinate axes are determined by the tangents to the coordinate curves at the intersection of three surfaces. They are not in general fixed directions in space, which happens to be the case for simple Cartesian coordinates, and thus there is generally no natural global basis for curvilinear coordinates. The momentum operator in quantum mechanics is the gradiant operator $p=\left(\hbar/i\right)\nabla$. By defining the Jacobi matrix as:

$$j_{\alpha\beta} = \frac{\partial x^{\alpha}}{\partial \xi^{\beta}}, \ \alpha, \beta = 1, 2, 3. \tag{2}$$

The Jacobian of the transformation is the determinant of the Jacobi matrix

$$J(\xi) = \det\left[j_{\alpha\beta} \right] \tag{3}$$

Define the natural basis vectors:

$$h_i = \frac{\partial r}{\partial \xi_{\alpha}}, \ \alpha = 1, 2, 3$$

$$r = (x_1, x_2, x_3) \tag{4}$$

The reduced *s*-particle density operators defined by Bogoliubov [3] in the following form

$$F_s\left(\xi_1, P_{\xi_1}, \xi_2, P_{\xi_2}, \cdots, \xi_N, P_{\xi_N}\right) = V^s Tr_{\xi_{s+1}\cdots\xi_N} Q^{-1} \exp\left(-\beta H_N\right); \tag{5}$$

where H_N is the Hamiltonian of our system given by

$$H_N = \frac{-\hbar^2}{2m}\nabla^2 + V(\xi) \tag{6}$$

where V is the potential of the system and Q is the configuration integral is given by

$$Q = Tr_{\xi_{s+1}\cdots\xi_N} \mathrm{e}^{-\beta H_N}, \tag{7}$$

The solution of N-particle schrödinger (time-dependent) equation with this Hamiltonian are given by $\left|\Psi^{(1)}\right\rangle \cdots \left|\Psi^{(M)}\right\rangle$ and from a complete orthonormal basis

$$\left\langle \Psi^{(1)} \middle| p_n \middle| \Psi^{(2)} \right\rangle = \frac{\hbar}{i} \int \mathrm{d}\xi_1 \int \mathrm{d}\xi_2 \int \mathrm{d}\xi_3 \sqrt{J} \Psi_1^* \frac{\partial \sqrt{J} \Psi^{(2)}}{\partial \xi_n}$$

$$\sum_{k=1}^{M} \left|\Psi^{(k)}\right\rangle \left\langle \Psi^{(k)}\right| = 1 \tag{8}$$

Define the N-particle density operator

$$\hat{\rho} = \sum_{k=1}^{M} w_k \left|\Psi^{(k)}\right\rangle \left\langle \Psi^{(k)}\right| \tag{9}$$

where w_k are positive real probabilities

$$\sum_{k=1}^{M} w_k = 1 \tag{10}$$

$$0 \le w_k \le 1$$

The density operator $\hat{\rho}$ follow the Von Neumann equation

$$i\hbar \frac{\partial}{\partial t} \hat{\rho} - \left[\hat{H}, \hat{\rho} \right] = 0 \tag{11}$$

In order to derive the quantum BBGKY-hierarchy, we introduce the reduced *s*-particle density operator as

$$\hat{F}_{1\cdots s} = C_s^N Tr_{s+1\cdots N} \hat{\rho} \tag{12}$$

and $Tr_{1\cdots s}\hat{F}_{1\cdots s} = C_s^N = \frac{N!}{(N-s)!}$.

The equation of motion for the reduced density operator obeys directly the Von Neuman equation. Now by substituting from Equation (12) into Equation (11) we get

$$i\hbar\frac{\partial}{\partial t}\hat{F}_{1\cdots s} - \left[\hat{H}_{1\cdots s}, \hat{F}_{1\cdots s}\right] = Tr_{s+1}\sum_{i=1}^{s}\left[\hat{v}_{i,s+1}, \hat{F}_{1\cdots s+1}\right] \tag{13}$$

where $\hat{v}_{i,j}$ is the potential between particles *i,j* and $\hat{H}_{1\cdots s}$ is the s-particle Hamiltonian operator. The above equation constitutes the quantum generalization of the (BBGKY) hierarchy.

3. The Binary Distribution Function

We assume that the momentum of the electron lies between ξ_1 and $\xi_1 + \mathrm{d}\xi_1$ is P_{ξ_1}. Also the momentum of the positron lies between ξ_2 and $\xi_2 + \mathrm{d}\xi_2$ is P_{ξ_2} and the momentum of the dust (ion) lies between ξ_3 and $\xi_3 + \mathrm{d}\xi_3$ is P_{ξ_3}. In this section, we shall find the binary distribution function of a quantum dusty in curvilinear coordinates. Firstly, define the quantum N particle distrbution function as follows:

$$F_N^{qu}\left(\xi_N, P_{\xi_N}\right) = \frac{N!\exp\left[-\beta\sum_{i=1}^{N}\frac{P_{\xi_i}^2}{2m} - \beta U\left(\xi_N\right)\right]}{\int \mathrm{d}P_{\xi_N}\exp\left[-\beta\sum_{i=1}^{N}\frac{P_{\xi_i}^2}{2m}\right]\int \mathrm{d}\xi_N \exp\left[-\beta U\left(\xi_N\right)\right]} \tag{14}$$

The one particle distribution function is obtained by reducing $F_N^{qu}\left(\xi_N, P_{\xi_N}\right)$ by integrating over $N-1$ positions and momenta then

$$F_1^{qu}\left(\xi_1, P_{\xi_1}\right) = \frac{1}{(N-1)!}\iint \mathrm{d}\xi_N \mathrm{d}P_{\xi_N} F_N^{qu}\left(\xi_N, P_{\xi_N}\right) \tag{15}$$

If there are no external fields

$$F_1^{qu}\left(\xi_1, P_{\xi_1}\right) = \alpha\exp\left[\frac{-\beta}{2m}P_{\xi_1}^2\right] \tag{16}$$

where the value of α can be found by normalization:

$$\iint \mathrm{d}\xi_1 \mathrm{d}P_{\xi_1} F_1^{qu}\left(\xi_1, P_{\xi_1}\right) = N \tag{17}$$

By substituting from Equation (16) into Equation (17) we get

$$\alpha^{-1} = \frac{V}{N}\left(\frac{2\pi m}{\beta}\right)^{3/2} \tag{18}$$

Then the one particle distribution function is given by

$$F_1^{qu}\left(\xi_1, P_{\xi_1}\right) = \frac{N}{V}\left(\frac{\beta}{2\pi m}\right)^{3/2}\exp\left[\frac{-\beta}{2m}P_{\xi_1}^2\right] \tag{19}$$

By putting $s = 1$ into Equation (13) we can get the first equation of quantum BBGKY as

$$i\hbar\frac{\partial}{\partial t}\hat{F}_1-\left[\hat{H}_1,\hat{F}_1\right]=Tr_{s+1}\sum_{i=1}^{s}\left[\hat{v}_{12},\hat{F}_{12}\right] \tag{20}$$

Then we have the binary distribution function by substituting from Equation (19) into Equation (20):

$$F_{12}^{qu}\left(\xi_1,P_{\xi_1},\xi_2,P_{\xi_2}\right)=F_1^{qu}\left(\xi_1,P_{\xi_1}\right)F_2^{qu}\left(\xi_2,P_{\xi_2}\right)+g\left(\xi_1,\xi_2\right) \tag{21}$$

where $g\left(\xi_1,\xi_2\right)$ is the correlation function.

Let us now study the model of dusty three component plasma *i.e.* the neutral system of point-like particles of positive and negative charges such as electrons, positrons and dust particles like ions. This model is an important model in both laboratory physics and space physics and has many applications [24]. By finding the quantum distribution functions of this model we can get the important thermodynamic functions such as the internal energy and the equation of state. Dust particles are heavier and slower in their velocities than electrons and positrons where for dusty plasma the relation between electrons, positrons, and dust (ion) density at equilibrium is $n_e=Z_d n_i+n_p$, where n_s is the number density of s^{th} species and Z_d is the charge state of dust [24].

Substituting Equations (19) and (21) into (13) for $s=1,2$ we obtain

$$\begin{aligned}F_{12}^{qu}=&\frac{N^2}{8V^2}\left(\frac{\beta}{\pi}\right)^3\left[\frac{\exp\left[-\beta\frac{P_{\xi_e}^2}{m_e}\right]}{m_e^3}+2\frac{\exp\left[\frac{P_{\xi_e}^2}{2m_e}+\frac{P_{\xi_i}^2}{2m_i}\right]}{\left(m_e m_i\right)^{3/2}}\right]\\&-\frac{e_1e_2}{KT\xi_{12}}\mathrm{e}^{-\kappa\xi_{12}}-\frac{e_1e_2\boldsymbol{p}_{\xi^1}\cdot\boldsymbol{p}_{\xi^2}\mathrm{e}^{-\kappa\xi_{12}}}{\left(mc\right)^2KT\xi_{12}}+\sum_{s=1}^{3}\frac{q_s^2}{m_s}\frac{1}{\xi_s}+\cdots\end{aligned} \tag{22}$$

4. The Triplet Distribution Function

The quantum triplet distribution function F_{123}^{qu} defined in such a way that $F_{123}^{qu}\left(\xi_1,P_{\xi_1},\xi_2,P_{\xi_2},\xi_3,P_{\xi_3},t\right)\mathrm{d}\xi_1\mathrm{d}\xi_2\mathrm{d}\xi_3\mathrm{d}P_{\xi_1}\mathrm{d}P_{\xi_2}\mathrm{d}P_{\xi_3}$ is the probability of finding a particle of the type 1^{th} in the volume element $\mathrm{d}\xi_1$ surrounding ξ_1,with momentum in range $P_{\xi_1}\to P_{\xi_1}+\mathrm{d}P_{\xi_1}$, a particle of type 2^{th} in the volume element $\mathrm{d}\xi_2$ surrounding ξ_2, with momentum in range $P_{\xi_2}\to P_{\xi_2}+\mathrm{d}P_{\xi_2}$ and a particle of the type 3^{th} in the volume element $\mathrm{d}\xi_3$ surrounding ξ_3, with momentum in range $P_{\xi_3}\to P_{\xi_3}+\mathrm{d}P_{\xi_3}$ respectively at time *t*.

The quantum triplet distribution function $F_{123}^{qu}\left(\xi_1,P_{\xi_1},\xi_2,P_{\xi_2},\xi_3,P_{\xi_3}\right)$ is defined by the calculation of the interaction between three charged particles seems rather involved, because the force on particle 1 at time t would depend on the position and momentum of particles 2 and 3 at a retarded time. For simplification the quantum triplet distribution function F_{123}^{qu} can be written as

$$\begin{aligned}F_{123}^{qu}\left(123\right)=&F_1^{qu}\left(1\right)F_1^{qu}\left(2\right)F_1^{qu}\left(3\right)\\&+F_1^{qu}\left(1\right)g\left(23\right)+F_1^{qu}\left(2\right)g\left(13\right)\\&+F_1^{qu}\left(3\right)g\left(12\right)+h\left(123\right)\end{aligned} \tag{23}$$

where $h(123)$ is the correlation function between particles 1, 2 and 3.

Substituting Equations (19) and (22) into (13) for $s=1,2,3$ we obtain

$$F_{123}^{qu}(123)=\frac{N^3}{16\sqrt{2}V^3}\left(\frac{\beta}{\pi}\right)^{\frac{9}{2}}\left[\frac{\exp\left[\frac{P_{\xi_1}^2}{2m_1}+\frac{P_{\xi_2}^2}{2m_2}+\frac{P_{\xi_3}^2}{2m_3}\right]}{(m_1m_2m_3)^{3/2}}\right]$$
$$+\frac{N}{V}\left(\frac{\beta}{2\pi m}\right)^{3/2}\left\{\exp\left[\frac{-\beta}{2m}P_{\xi_1}^2\right]g(23)+\exp\left[\frac{-\beta}{2m}P_{\xi_2}^2\right]g(13)\right. \quad (24)$$
$$\left.+\exp\left[\frac{-\beta}{2m}P_{\xi_3}^2\right]g(12)\right\}+h(123)$$

For three component plasma, we can use the two particle correlation function $g(12)$ which is given by

$$g(12)=g_1(\xi_{12})\left[1+\frac{\boldsymbol{p}_{\xi^1}\cdot\boldsymbol{p}_{\xi^2}}{(mc)^2}+\frac{\left(\boldsymbol{\xi}_{12}\cdot\boldsymbol{p}_{\xi^1}\right)\left(\boldsymbol{\xi}_{12}\cdot\boldsymbol{p}_{\xi^2}\right)}{2(mc)^2\xi_{12}^2}\right] \quad (25)$$

where

$$g_1(\xi_{12})=-\frac{e_1e_2}{KT\xi_{12}}\mathrm{e}^{-\kappa\xi_{12}} \quad (26)$$

$g_1(r_{12})$ is the Debye-Hückel solution and the three particle correlation function $G(1,2,3)$ which is given by

$$h(123)=g_1(\xi_{12})g_1(\xi_{13})g_1(\xi_{23})\left[1+\frac{\boldsymbol{p}_{\xi^1}\cdot\boldsymbol{p}_{\xi^2}}{(mc)^2}+\frac{\boldsymbol{p}_{\xi^1}\cdot\boldsymbol{p}_{\xi^3}}{(mc)^2}\right.$$
$$\left.+\frac{\boldsymbol{p}_{\xi^2}\cdot\boldsymbol{p}_{\xi^3}}{(mc)^2}+\sum_{i,j=1,i\neq j}^{3}\frac{\left(\boldsymbol{\xi}_{ij}\cdot\boldsymbol{p}_{\xi^i}\right)\left(\boldsymbol{\xi}_{ij}\cdot\boldsymbol{p}_{\xi^j}\right)}{2(mc)^2\xi_{ij}^2}+\cdots\right] \quad (27)$$

Whatever particles 1, 2, 3 are, we can write the quantum triplet distribution function $F_{123}^{qu}(123)$ as

$$F_{123}^{qu}(123)=\frac{N^3}{16\sqrt{2}V^3}\left(\frac{\beta}{\pi}\right)^{\frac{9}{2}}\left[\frac{\exp\left[\frac{P_{\xi_1}^2}{2m_1}+\frac{P_{\xi_2}^2}{2m_2}+\frac{P_{\xi_3}^2}{2m_3}\right]}{(m_1m_2m_3)^{3/2}}\right]$$
$$+\frac{N}{V}\left(\frac{\beta}{2\pi m}\right)^{3/2}\left\{\exp\left[\frac{-\beta}{2m}P_{\xi_1}^2\right]\left(g_1(\xi_{23})\left[1+\frac{\boldsymbol{p}_{\xi^2}\cdot\boldsymbol{p}_{\xi^3}}{(mc)^2}+\frac{\left(\boldsymbol{\xi}_{23}\cdot\boldsymbol{p}_{\xi^2}\right)\left(\boldsymbol{\xi}_{23}\cdot\boldsymbol{p}_{\xi^3}\right)}{2(mc)^2\xi_{23}^2}\right]\right)\right.$$
$$\left.+\exp\left[\frac{-\beta}{2m}P_{\xi_2}^2\right]\left(g_1(\xi_{13})\left[1+\frac{\boldsymbol{p}_{\xi^1}\cdot\boldsymbol{p}_{\xi^3}}{(mc)^2}+\frac{\left(\boldsymbol{\xi}_{13}\cdot\boldsymbol{p}_{\xi^1}\right)\left(\boldsymbol{\xi}_{13}\cdot\boldsymbol{p}_{\xi^3}\right)}{2(mc)^2\xi_{13}^2}\right]\right)\right.$$

$$+\exp\left[\frac{-\beta}{2m}P_{\xi_3}^2\right]\left(g_1(\xi_{12})\left[1+\frac{\boldsymbol{p}_{\xi^1}\cdot\boldsymbol{p}_{\xi^2}}{(mc)^2}+\frac{\left(\boldsymbol{\xi}_{12}\cdot\boldsymbol{p}_{\xi^1}\right)\left(\boldsymbol{\xi}_{12}\cdot\boldsymbol{p}_{\xi^2}\right)}{2(mc)^2\xi_{12}^2}\right]\right)\Bigg\}$$

$$+g_1(\xi_{12})g_1(\xi_{13})g_1(\xi_{23})\Bigg[1+\frac{\boldsymbol{p}_{\xi^1}\cdot\boldsymbol{p}_{\xi^2}}{(mc)^2}+\frac{\boldsymbol{p}_{\xi^1}\cdot\boldsymbol{p}_{\xi^3}}{(mc)^2}+\frac{\boldsymbol{p}_{\xi^2}\cdot\boldsymbol{p}_{\xi^3}}{(mc)^2} \tag{28}$$

$$+\sum_{i,j=1,i\neq j}^{3}\frac{\left(\boldsymbol{\xi}_{ij}\cdot\boldsymbol{p}_{\xi^i}\right)\left(\boldsymbol{\xi}_{ij}\cdot\boldsymbol{p}_{\xi^j}\right)}{2(mc)^2\xi_{ij}^2}\Bigg]$$

5. Quantum Distribution Functions of Saturn's Rings

An alternative statistical description of planetary rings was formulated in a series of papers by Hämeen-Anttila [32] [33]. It uses a kinetic equation of Boltzmann type for the description of the evolution of the one-particle phase space distribution function, in a similar manner as gas-kinetics. Hämeen-Anttila gives analytical solutions for the collision integrals, where necessary in terms of appropriate approximations. The effect of self-gravity is taken into account in a self consistent manner in the local vertical gravity field of the disk and in its effect on close particle encounters. In principle the theory can treat the average effect of particle surface irregularities stochastically and it is formulated so that it can be extended to describe particle fragmentation and coagulation.

The biggest advantage is that the balance equations for mass, stress, and scale hight of the ring, are given analytically as partial differential equations. Thus, the theory can be applied to investigate the dynamical evolution of a planetary ring. The disk's self-gravity potential ϕ_{disk} couples to the surface mass density through Poisson's equation [34]

$$\nabla^2\phi_{disk}=4\pi a\sigma\delta \tag{29}$$

where σ is the surface mass density, a is gravitation parameter and δ is the Dirac delta function.

$$\frac{1}{h_1h_2h_3}\left[\frac{\partial}{\partial\xi_1}\left(\frac{h_2h_3}{h_1}\frac{\partial\phi_{disk}}{\partial\xi_1}\right)+\frac{\partial}{\partial\xi_2}\left(\frac{h_1h_3}{h_2}\frac{\partial\phi_{disk}}{\partial\xi_2}\right)+\frac{\partial}{\partial\xi_3}\left(\frac{h_2h_1}{h_3}\frac{\partial\phi_{disk}}{\partial\xi_3}\right)\right]=4\pi a\sigma\delta \tag{30}$$

where h_1, h_2h_3 is the natural basis vectors. The Kinetic theory describes the evolution of the local velocity distribution function of an ensemble of particles in terms of the Boltzmann equation or a suitable generalization of it, like Enskog's theory of hard sphere gases. The kinetic equation can be derived from Liouville's theorem, appearing as the leading equation in a hierarchy of equations describing n-particle distribution functions in phase space and neglecting correlations between particle pairs. Then the one particle distribution function in Equation (19) in in the local vertical gravity field can be given by

$$F_1^{qu}\left(\xi_1,P_{\xi_1}\right)=\frac{N}{V}\left(\frac{\beta}{2\pi m}\right)^{3/2}\exp\left[\frac{-\beta}{2m}P_{\xi_1}^2-e\phi\right] \tag{31}$$

Kinetic theory allows us to incorporate the full complexity of the dynamics of a planetary ring in a statistical description, such as the effects of the motion of ring particles on curved orbits between inelastic collisions, their finite size, the anisotropy of the velocity dispersion, and in principle also coagulation and fragmentation of the ring particles.

The collision motion of an ensemble of identical particles in the plane, in the frame of reference rotating with angular velocity ω can be described by the Boltzmann equation [35] in Curvilinear Coordinates:

$$\begin{aligned}&\frac{\partial f}{\partial t}+\frac{p_{\xi_1}}{mh_1}\frac{\partial f}{\partial \xi_1}+\left(\omega+\frac{p_{\xi_2}}{mh_2}\right)\frac{\partial f}{\partial \xi_2}+\left(\frac{2\omega}{m}p_{\xi_2}+\frac{p_{\xi_2}^2}{mh_2}-\frac{\partial \phi_1}{h_1\partial \xi_1}\right)\frac{\partial f}{\partial p_{\xi_1}}\\&=\left(\frac{\kappa^2}{2mh_1\omega}p_{\xi_1}+\frac{p_{\xi_1}p_{\xi_2}}{m^2h_1h_2}+\frac{\partial \phi_1}{h_2\partial \xi_2}\right)\frac{\partial f}{\partial p_{\xi_2}}+\left(\frac{\partial f}{\partial t}\right)_{cl}\end{aligned} \tag{32}$$

where ξ_1,ξ_2,ξ_3 was defined by Equation (1) and $\left(\frac{\partial f}{\partial t}\right)_{cl}$ is the collision integral which takes into account effects due to the discrete-point nature of the gravitational charges, or collision effects (including diffusion in space and velocity), and defines the change of the distribution function $f(r, v, t)$ arising from ordinary interparticle collisions (in a plasma this term represents the change of f arising from collisions with particles at distances shorter than a Debye length). The Boltzmann form for the collision integral is based on an assumption that the duration of a collision is much less than the time between collisions instantaneous collisions are considered [36]. The simple Krook integral in the case of a two-dimensional disk of identical particles has the form

$$\left(\frac{\partial f}{\partial t}\right)_{cl}=-\nu_c\left(f-f_0\right) \tag{33}$$

where f is the actual distribution function of particles and f_0 is the steady-state equilibrium distribution function (Shu and Stewart, 1985) [35]. The equilibrium axially symmetric distribution function is the Maxwellian with the surface density σ_0:

$$f_0=\frac{\sigma_0}{2\pi c^2}\exp\left(-\frac{p_\xi^2}{2m^2c^2}\right) \tag{34}$$

The gravitational potential of a rotating oblate planet

$$\phi(\xi,\beta)=-\frac{aM_0}{2}\left[1+\left(\frac{R}{\xi}\right)^2\left(\frac{1}{2}-\frac{3}{2}\sin^2\beta\right)I_2\right] \tag{35}$$

where r is the distance from the center of the planet to the point at which the potential is sought, β is the planetocentric latitude of the point, R is the radius of the planet, and M_0 is its mass. For saturn $I_2=0.017$, $M_0=5.7\times10^{29}$ g and $R=6\times10^7$ m for more exact values of the parameters see Ref. [37].

6. Conclusions

In this work we obtained the quantum binary and triplet distribution functions

of dusty plasma; the calculation is based on curvilinear coordinates and the Bogoliubov-Born-Green-Kirkwood-Yvon (BBGKY) hierarchy. We consider only the thermal equilibrium plasma. The model under consideration is the three-component dusty plasma *i.e.* neutral system of point like particles of positive and negative charges (electrons and positrons) interspersed with dust particles (ions) [24]. **Figure 1** and **Figure 2** show the effect of dust on the quantum binary and triplet distribution functions. From these figures we note that the existence of dust makes a fluctuation in binary and triplet distribution functions in the range of $\xi = (0.5, 2.5)$. It was shown that the local stability criterion obtained from the computer models is in general agreement with the theoretical prediction as outlined in the present paper.

The first derivation of reactive quantum Boltzmann equations by Olmstead and Curtiss [18] starts with the Wigner transformed version of the standard BBGKY hierarchy for a system of stable atomic and diatomic constituents. Also, they calculated the quantum triplet distribution function of moderately dense gases. Alavi *et al.* [19] described the time evolution of a one-particle statistical distribution or density operator, influenced by the interaction of another particle which represents the effect of all other particles in the system.

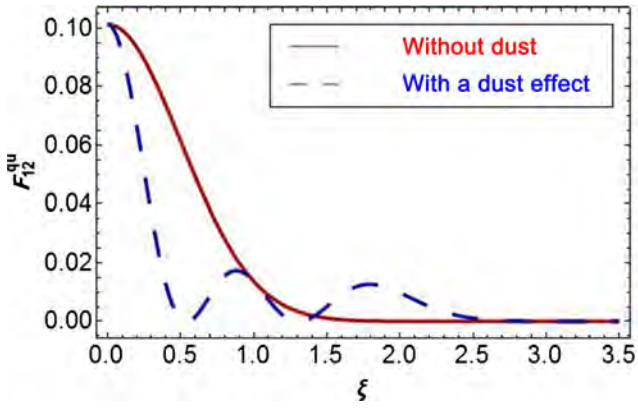

Figure 1. The quantum binary distribution function from Equation (22) without dust effect (solid line) and with a dust effect (dashed line).

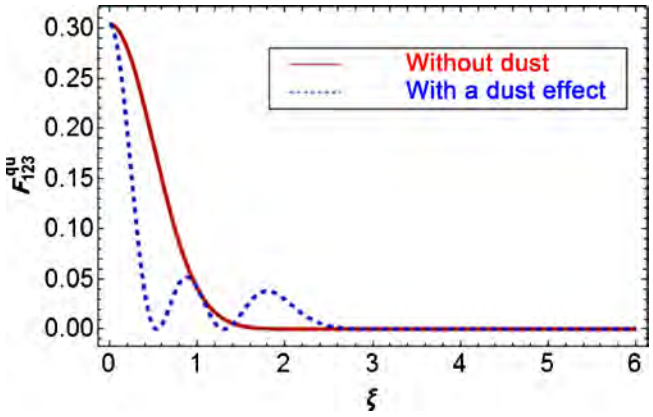

Figure 2. The quantum triplet distribution function from Equation (28) without dust effect (solid line) and with a dust effect (dashed line).

Figure 3 and Figure 4 show the comparison between the quantum binary and triplet distribution function based on our result without dust effect (solid line), Alavi *et al.* [19] (dashed line) and from Olmstead and Curtiss [18] (dot-dashed line). We note from this comparison the convergence between the results obtained and the results of the references [19] and [18].

Figure 5 and Figure 6 show the comparison between the quantum binary and triplet distribution function based on our result with the effect of dust, Alavi *et al.* [19] and from Olmstead and Curtiss [18]. After taking into account the effect of dust, we noticed that our results are closer to the results obtained by Olmstead and Curtiss [18] in the range of $\xi=(0,0.5)$, but with the increase in the value of the variable ξ in the range of $\xi=(0.5,1)$ the results are closer to results obtained by Alavi *et al.* [19].

Initial quantum curvilinear coordinates phase-space (ξ,V_ξ) for dusty plasma electrons (gray color), positrons (red color) and dust (orange color) was given in Figure 7. Figure 8 shows the quantum curvilinear coordinates phase-space (ξ,V_ξ) for dusty plasma based on Particle-In-Cell (PIC) simulation methods.

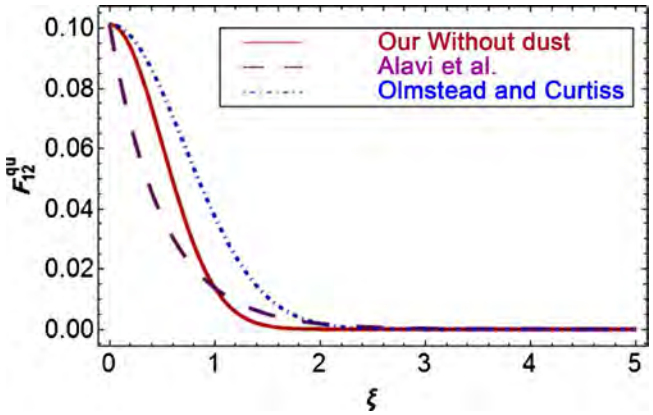

Figure 3. The comparison between the quantum binary distribution function based on our result without dust effect (solid line), Alavi *et al.* [19] (dashed line) and from Olmstead and Curtiss [18] (dot-dashed line).

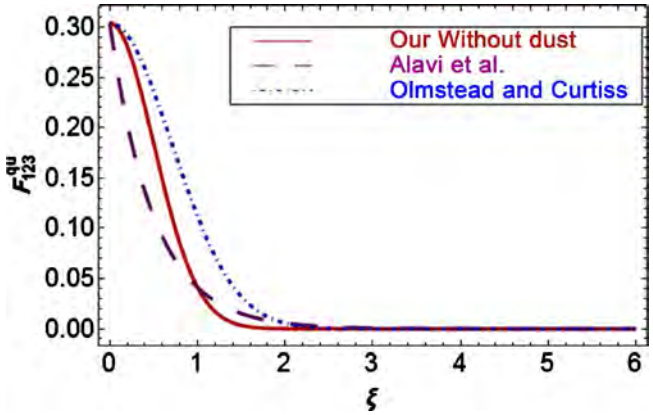

Figure 4. The comparison between the quantum triplet distribution function based on our result without dust effect (solid line), Alavi *et al.* [19] (dashed line) and from Olmstead and Curtiss [18] (dot-dashed line).

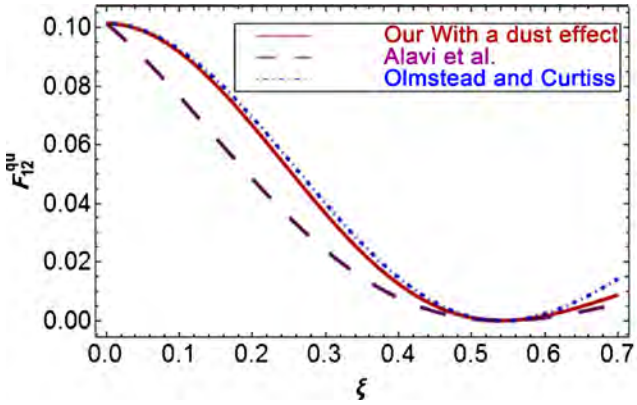

Figure 5. The comparison between the quantum binary distribution function based on our result with a dust effect (solid line), Alavi *et al.* [19] (dashed line) and from Olmstead and Curtiss [18] (dot-dashed line).

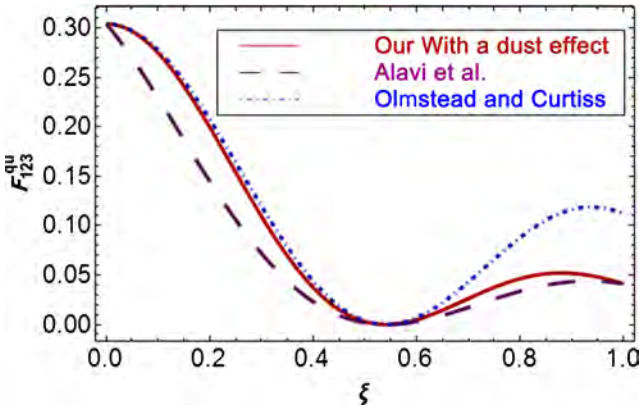

Figure 6. The comparison between the quantum triplet distribution function based on our result without dust effect (solid line), Alavi *et al.* [19] (dashed line) and from Olmstead and Curtiss [18] (dot-dashed line).

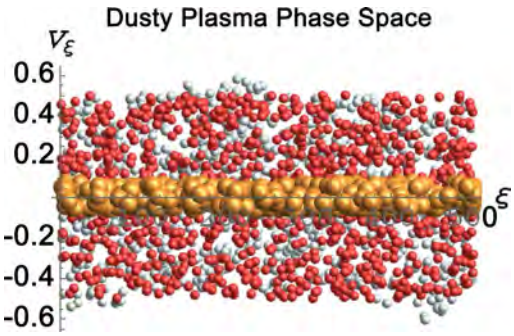

Figure 7. Initial quantum curvilinear coordinates phase-space (ξ, V_ξ) for dusty plasma electrons (gray color), positrons (red color) and dust (orange color).

We observe from the phase space that the speed of dust particles is much lower than the speed of electrons and positrons. The density of dust particles varies due to the large volume of dust particles.

The quantum binary distribution function for dusty plasma was given in **Figure 9**. The quantum triplet distribution function for dusty plasma see **Figure 10**

with $\xi_1 = \xi_2 \neq \xi_3$.

Figure 11 and Figure 12 show the quantum binary and triplet distribution functions for dusty plasma in curvilinear phase space $\left(\xi, P_\xi\right)$. These solutions are important in different branches of physics and other areas of applied sciences and can provide help for researchers to study and understand the physical interpretation of the dusty plasma model.

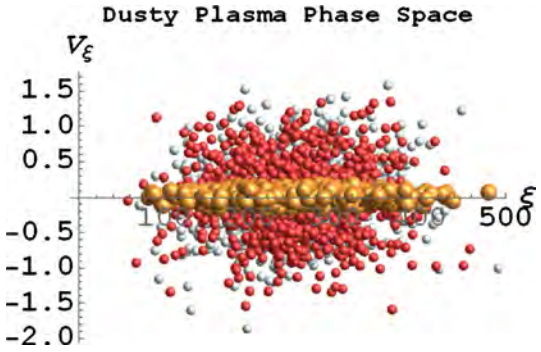

Figure 8. The quantum curvilinear coordinates phase-space $\left(\xi, V_\xi\right)$ for dusty plasma electrons (gray color), positrons (red color) and dust (orange color) based on Particle-In-Cell (PIC) simulation methods.

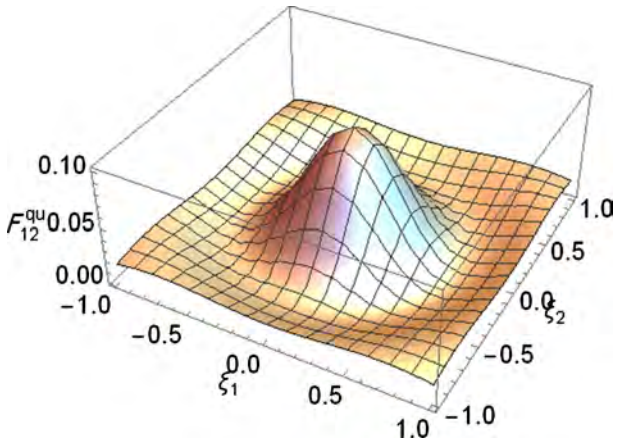

Figure 9. The quantum binary distribution function for dusty plasma with $\xi_1 \neq \xi_2$.

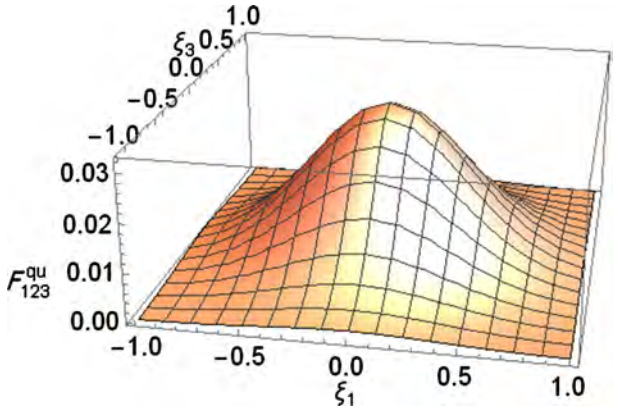

Figure 10. The quantum triplet distribution function for dusty plasma with $\xi_1 = \xi_2 \neq \xi_3$.

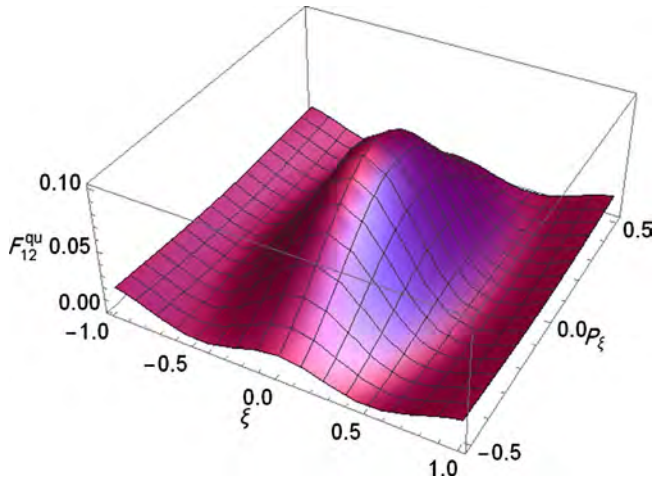

Figure 11. The quantum binary distribution function for dusty plasma in curvilinear phase-space (ξ, P_ξ).

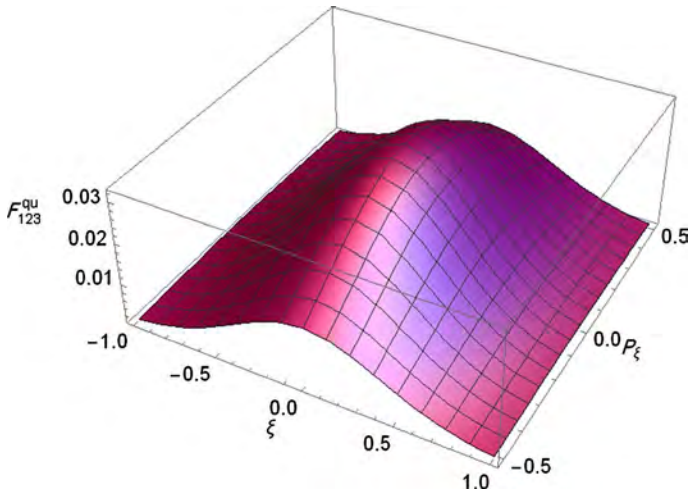

Figure 12. The quantum triplet distribution function for dusty plasma in curvilinear phase-space (ξ, P_ξ).

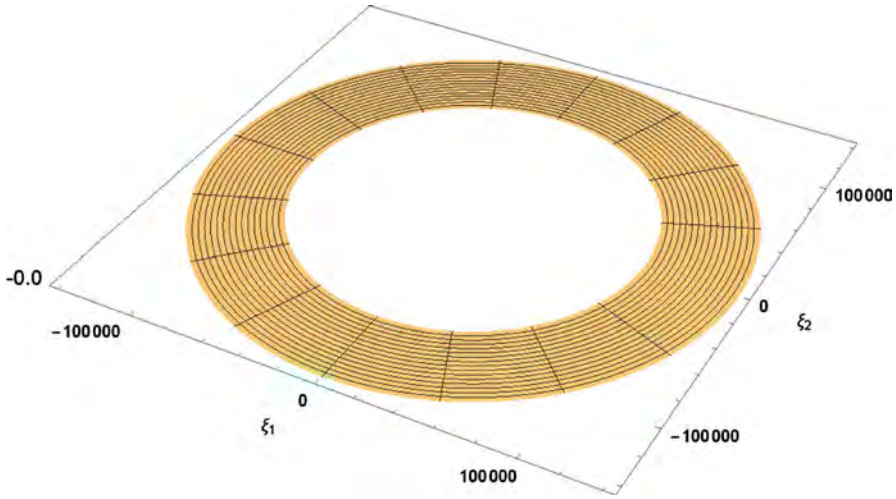

Figure 13. Model of Saturn planet rings in the radius interval (92,000 km; 139,350 km).

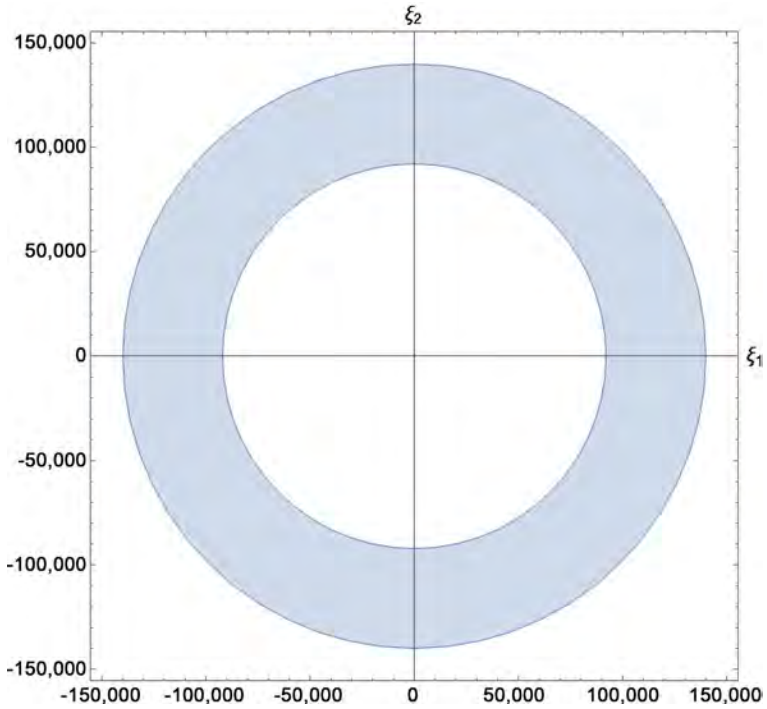

Figure 14. 2D Model of Saturn planet rings in the radius interval (92,000 km; 139,350 km).

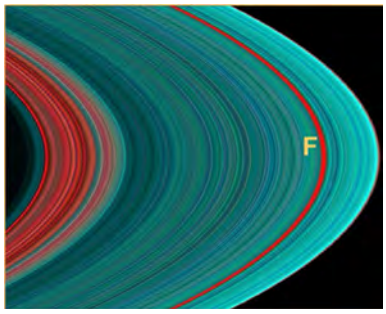

Figure 15. Ultraviolet ring's image; red color refer to dust and blue for water ice.

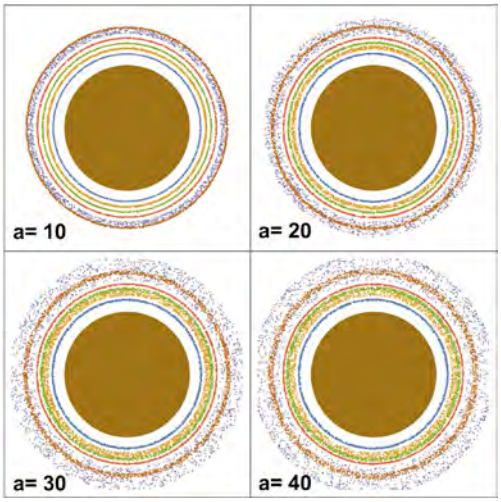

Figure 16. Simulation of dusty plasma for sturan rings for different values of gravitation parameter in the radius interval (92,000 km; 139,350 km).

Model of Saturn planet rings in the radius interval (92,000 km, 139,350 km) was given in Figure 13 and Figure 14. Figure 15 shows ultraviolet ring's image; red color refers to dust and blue for water ice. Figure 16 shows the Simulation model of dusty plasma for Saturn rings for different values of gravitation parameter. Also, we note from this figure when gravitation parameter increased the dispersion of the presence of particles becomes more visible than the lower values of the gravitation parameter.

Conflicts of Interest

The authors declare no conflicts of interest regarding the publication of this paper.

References

[1] Hussein, N.A. and Hassan, A.R. (1990) Quantum Binary Distribution of High Temperature Plasma. *Bulletin of the Faculty of Science. Assiut University*, **19**, 39-98.

[2] Kraeft, W.D., Vorberger, J., Gericke, D.O. and Schlanges, M. (2007) Thermodynamic Functions for Plasmas beyond Montroll Ward. *Contributions to Plasma Physics*, **47**, 253-261. https://doi.org/10.1002/ctpp.200710034

[3] Bogoliubov, N.N. (1962) Probleme der Dynamischen Theorie in der Statistischen Physik. *Studies in Statistical Mechanics*, **10**, 275.

[4] Kraeft, W.D., Kremp, D., Ebeling, W. and Röpke, G. (1986) Quantum Statistics of Charged Particle Systems. Akademie Verlag, Berlin. https://doi.org/10.1007/978-1-4613-2159-0

[5] Kaniadakis, G. (2003) BBGKY Hierarchy Underlying Many-Particle Quantum Mechanics. *Physics Letters A*, **310**, 377-382. https://doi.org/10.1016/S0375-9601(03)00448-1

[6] Fesciyan, S. (1973) The BBGKY Hierarchy in Quantum Statistical Mechanics. *Communications in Mathematical Physics*, **30**, 11-22. https://doi.org/10.1007/BF01646684

[7] Hussein, N.A., Osman, A.-N.A., Eisa, D.A. and Abbas, R.A. (2014) Quantum Binary and Triplet Distribution Functions of Plasma by using Green's Function. *Contributions to Plasma Physics*, **54**, 815-826. https://doi.org/10.1002/ctpp.201400016

[8] Barker, A. (1968) A Quantum Mechanical Calculation of the Radial Distribution Function for a Plasma. *Australian Journal of Physics*, **21**, 121-128. https://doi.org/10.1071/PH680121

[9] Satoh, H., Tanaka, M. and Katsura, S. (1984) Triplet Distribution Function of the Fluid with the Square Well Potential. *Molecular Physics*, **53**, 1195-1208. https://doi.org/10.1080/00268978400102941

[10] Lado, F. (1991) Integrals over the Triplet Distribution Function without the Triplet Distribution Function. *Molecular Physics*, **72**, 1387-1395. https://doi.org/10.1080/00268979100100971

[11] Taylor, M.P. and Lipson, J.E.G. (1992) On the Born-Green-Yvon Equation and Triplet Distributions for Hard Spheres. *The Journal of Chemical Physics*, **97**, 4301. https://doi.org/10.1063/1.463932

[12] Zahn, K., Maret, G., Rub, C. and Grunberg, H. (2003) Three-Particle Correlations in

Simple Liquids. *Physical Review Letters*, **91**, Article ID: 115502. https://doi.org/10.1103/PhysRevLett.91.115502

[13] Russ, C., Brunner, M., Bechinger, C. and Grunberg, H. (2005) Three-Body Forces at Work: Three-Body Potentials Derived from Triplet Correlations in Colloidal Suspensions. *Europhysics Letters*, **69**, 468. https://doi.org/10.1209/epl/i2004-10345-8

[14] Jorge, S., Lomba, E. and Abascal, J.L.F. (2002) Theory and Simulation of the Triplet Structure Factor and Triplet Direct Correlation Functions in Binary Mixtures. *Chemical Physics*, **116**, 730. https://doi.org/10.1063/1.1426418

[15] Ludwig, P., Thomsen, H., Balzer, K., Filinov, A. and Bonitz, M. (2010) Tuning Correlations in Multi-Component Plasmas. *Plasma Physics and Controlled Fusion*, **52**, Article ID: 124013. https://doi.org/10.1088/0741-3335/52/12/124013

[16] Hakim, R. (2011) Introduction to Relativistic Statistical Mechanics: Classical and Quantum. World Scientific, USA. https://doi.org/10.1142/7881

[17] Hansen, J.P. (1973) Statistical Mechanics of Dense Ionized Matter. I. Equilibrium Properties of the Classical One-Component Plasma. *Physical Review A*, **8**, 3096. https://doi.org/10.1103/PhysRevA.8.3096

[18] Olmstead, R.D. and Curtiss, C.F. (1975) A Quantum Kinetic Theory of Moderately Dense Gases. III. The Effect of Bound States on the Transport Coefficients. *The Journal of Chemical Physics*, **63**, 1966. https://doi.org/10.1063/1.431531

[19] Alavi, S., Wei, G.W. and Snider, R.F. (1998) Chain Relations of Reduced Distribution Functions and Their Associated Correlation Functions. *The Journal of Chemical Physics*, **108**, 706. https://doi.org/10.1063/1.475430

[20] Błaszak, M. and Domański, Z. (2013) Canonical Quantization of Classical Mechanics in Curvilinear Coordinates. Invariant Quantization Procedure. *Annals of Physics*, **339**, 89-108. https://doi.org/10.1016/j.aop.2013.08.014

[21] Kjaergaard, H.G. and Mortensen, O.S. (1990) The Quantum Mechanical Hamiltonian in Curvilinear Coordinates: A Simple Derivation. *American Journal of Physics*, **58**, 344-347. https://doi.org/10.1119/1.16167

[22] Fichtl, C., Finn, J. and Cartwright, K. (2012) An Arbitrary Curvilinear-Coordinate Method for Particle-in-Cell Modeling. *Computational Science & Discovery*, **5**, Article ID: 014011. https://doi.org/10.1088/1749-4699/5/1/014011

[23] Mendis, D.A. (1997) Advances in Dusty Plasmas: Proceedings of the International Conference on the Physics of Dusty Plasmas. In: Shukla, P.K., Mendis, D. and Desai, T., Eds., *Advances in Dusty Plasmas*, World Scientific, Singapore, 3-19.

[24] Shukla, P.K. and Mamun, A.A. (2002) Introduction to Dusty Plasma Physics. IOP, London, UK.

[25] Ferdousi, M., Yasmin, S., Ashraf, S. and Mamun, A.A. (2015) Ion-Acoustic Shock Waves in Nonextensive Electron-Positron-Ion Plasma. *Chinese Physics Letters*, **32**, Article ID: 015201. https://doi.org/10.1088/0256-307X/32/1/015201

[26] Wang, Y. and Zhang, J. (2008) Soliton and Chaotic Structures of Dust Ion-Acoustic Waves in Quantum Dusty Plasmas. *Physics Letters A*, **372**, 6509-6517. https://doi.org/10.1016/j.physleta.2008.09.004

[27] Goertz, C. (1989) Dusty Plasmas in the Solar System. *Reviews of Geophysics*, **27**, 271-292. https://doi.org/10.1029/RG027i002p00271

[28] Dougherty, M., Esposito, L. and Krimigis, S. (2009) Saturn from Cassini-Huygens. Springer Science & Business Media, Berlin. https://doi.org/10.1007/978-1-4020-9217-6

[29] Smith, L., Soderblom, R., Batson, P., Bridges, J., Inge, H. and Bunker, A. (1982) A

New Look at the Saturn System: The Voyager 2 Images. *Science*, **215**, 504-537. https://doi.org/10.1126/science.215.4532.504

[30] Gyergyek, T. and Kovačič, J. (2014) Potential Formation in Front of an Electrode Close to the Plasma Potential Studied by PIC Simulation. *Contributions to Plasma Physics*, **54**, 647-668. https://doi.org/10.1002/ctpp.201300036

[31] Reinmüller, K. (1998) Determination of the Plasma Potential Using Emissive Probes-Implications from PIC Simulations. *Contributions to Plasma Physics*, **38**, 7-12. https://doi.org/10.1002/ctpp.19980380106

[32] Hämeen-Anttila, K.A. (1975) Statistical Mechanics of Keplerian Orbits. *Astrophysics and Space Science*, **37**, 309-333. https://doi.org/10.1007/BF00640356

[33] Hämeen-Anttila, K.A. (1976) Statistical Mechanics of Keplerian Orbits. II-Dispersion in Particle Size. *Astrophysics and Space Science*, **43**, 145-174. https://doi.org/10.1007/BF00640563

[34] Pollack, J.B. (1975) The Rings of Saturn. *Space Science Reviews*, **18**, 3-93. https://doi.org/10.1007/BF00350197

[35] Shu, F.H. and Stewart, G.R. (1985) The Collisional Dynamics of Particulate Disks. *Icarus*, **62**, 360-383. https://doi.org/10.1016/0019-1035(85)90181-2

[36] Griv, E., Gedalin, M., Eichler, D. and Yuan, C. (2000) A Gas-Kinetic Stability Analysis of Self-Gravitating and Collisional Particulate Disks with Application to Saturn's Rings. *Planetary and Space Science*, **48**, 679-698. https://doi.org/10.1016/S0032-0633(00)00037-4

[37] https://solarsystem.nasa.gov/planets/saturn/overview/

Scientific Research Publishing

International Journal of Astronomy and Astrophysics, 2019, 9, 133-141
http://www.scirp.org/journal/ijaa
ISSN Online: 2161-4725
ISSN Print: 2161-4717

A Study of Dark Matter with Spiral Galaxy Rotation Curves. Part II

Bruce Hoeneisen

Universidad San Francisco de Quito, Quito, Ecuador
Email: bruce1@fnal.gov

How to cite this paper: Hoeneisen, B. (2019) A Study of Dark Matter with Spiral Galaxy Rotation Curves. Part II. *International Journal of Astronomy and Astrophysics*, **9**, 133-141.
https://doi.org/10.4236/ijaa.2019.92010

Received: April 19, 2019
Accepted: June 11, 2019
Published: June 14, 2019

Abstract

In Part II of this study of spiral galaxy rotation curves we apply corrections and estimate all identified systematic uncertainties. We arrive at a detailed, precise, and self-consistent picture of dark matter.

Keywords

Dark Matter, Spiral Galaxies, Disk Galaxies, Majorana Neutrinos

1. Introduction

Dark matter in the core of spiral galaxies can exceed 10^7 times the mean dark matter density of the Universe. For this reason we have studied spiral galaxy rotation curves measured by the THINGS collaboration [1] with the hope of constraining the properties of dark matter [2]. In "Part I" of this study [2] we integrate numerically the equations that describe the mixture of two self-gravitating non-relativistic ideal gases, "baryons" and "dark matter". These equations require four boundary conditions: the densities $\rho_h(r_{\min})$ and $\rho_b(r_{\min})$ of dark matter and baryons at the first measured point $r_{\min}$, and the "reduced" root-mean-square radial velocities $\langle v_{rh}^2 \rangle'^{1/2}$ and $\langle v_{rb}^2 \rangle'^{1/2}$, defined as follows:

$$\langle v_{rh}^2 \rangle' \equiv \frac{\langle v_{rh}^2 \rangle}{1-\kappa_h}, \tag{1}$$

and similarly for baryons. $\langle v_{rh}^2 \rangle^{1/2}$ is the root-mean-square of the radial component of the dark matter particle velocities, and $0 \le \kappa_h \le 1$ describes dark matter rotation, see [2] for details. In the present analysis we take $\kappa_h = 0.15 \pm 0.15(\text{syst})$ [2]. The four boundary parameters are fit to minimize the χ^2 between the rotation curves $v_{\text{obs}}(r)$ and $v_b(r)$ measured by the THINGS collaboration [1], and the calculated rotation curves. The fits obtain rotation curves within the ob-

servational uncertainties. These fits are presented in Figures 1 to 10 of [2], and the fitted parameters are presented in Table 1 of [2].

In the present analysis we apply corrections and study all identified systematic uncertainties. We use the standard notation in cosmology as defined in [3], and the values of the cosmological parameters therein. Occasionally we use units with $\hbar = 1$ and $c = 1$ as is customary.

2. Corrections from $\rho_h(r_{\min})$ to $\rho_h(r \to 0)$

The first measured point $r_{\min}$ does not lie in the center of the spiral galaxy core, so we make a correction from $\rho_h(r_{\min})$ to $\rho_h(r \to 0)$ by numerical integration with the same equations and parameters described above. These corrections are presented in Table 1.

3. Measurement of the Adiabatic Invariant $v_{hrms}(1)$

For each spiral galaxy we obtain the parameter

$$v_{hrms}(1)^2 \equiv 3\left\langle v_{rh}^2 \right\rangle \left(\frac{\Omega_c \rho_{\text{crit}}}{\rho_h(0)} \right)^{2/3} \equiv \frac{3kT_h(1)}{m_h}. \tag{2}$$

$v_{hrms}(1)$ is the dark matter particles root-mean-square velocity extrapolated to the present time with expansion parameter $a = 1$ in three dimensions, hence the factor 3. $T_h(1)$ is the temperature of dark matter of a homogeneous Universe at the present time. The parameter $v_{hrms}(1)$ is invariant with respect to adiabatic expansion of the dark matter. Note that for an ideal "noble" gas

Table 1. Corrections from $\rho_h(r_{\min})$ [2] to $\rho_h(r \to 0)$. The statistical uncertainty is from the fit [2]. The systematic uncertainty is from the extrapolation from $r_{\min}$ to $r \to 0$.

Galaxy	$r_{\min}$ [kpc]	$\rho_h(r_{\min})$ $\left[10^{-2} M_\odot \text{ pc}^{-3}\right]$	$\rho_h(r \to 0)$ $\left[10^{-2} M_\odot \text{ pc}^{-3}\right]$
NGC 2403	0.5	$7.5 \pm 1.4(\text{stat})$	$10.3 \pm 1.4(\text{stat}) \pm 0.8(\text{syst})$
NGC 2841	4.0	$9.3 \pm 0.7(\text{stat})$	$20.8 \pm 0.7(\text{stat}) \pm 6.0(\text{syst})$
NGC 2903	1.0	$14.6 \pm 2.1(\text{stat})$	$14.7 \pm 2.1(\text{stat}) \pm 0.7(\text{syst})$
NGC 2976	0.1	$4.0 \pm 2.7(\text{stat})$	$4.06 \pm 2.70(\text{stat}) \pm 0.03(\text{syst})$
NGC 3198	1.0	$4.5 \pm 0.8(\text{stat})$	$5.3 \pm 0.8(\text{stat}) \pm 1.0(\text{syst})$
NGC 3521	1.0	$22.9 \pm 8.6(\text{stat})$	$24.6 \pm 8.6(\text{stat}) \pm 0.7(\text{syst})$
NGC 3621	0.5	$2.6 \pm 0.5(\text{stat})$	$2.93 \pm 0.50(\text{stat}) \pm 0.10(\text{syst})$
DDO 154	0.25	$1.3 \pm 0.3(\text{stat})$	$1.36 \pm 0.30(\text{stat}) \pm 0.10(\text{syst})$
NGC 5055	1.0	$28.2 \pm 6.8(\text{stat})$	$37.3 \pm 6.8(\text{stat}) \pm 9.0(\text{syst})$
NGC 7793	0.25	$8.0 \pm 1.6(\text{stat})$	$8.98 \pm 1.6(\text{stat}) \pm 0.5(\text{syst})$

$T_h V^{\gamma-1} = \text{constant}$ with $\gamma = 5/3$. By "noble" we mean that collisions (if any) between dark matter particles do not excite internal degrees of freedom (if any) of these particles. Alternatively, Equation (2) can be understood as $v_h \propto 1/a$ for non-relativistic particles in an expanding Universe. At expansion parameter a when perturbations are still linear, and after dark matter becomes non-relativistic, the root-mean-square velocity of dark matter particles is

$$v_{h\text{rms}}(a) = \frac{v_{h\text{rms}}(1)}{a} \equiv \left(\frac{3kT_h(a)}{m_h}\right)^{1/2}. \tag{3}$$

Results are presented in **Table 2**. The average of $v_{h\text{rms}}(1)$ of 10 complete and independent measurements is

$$v_{h\text{rms}}(1) = 1.192 \pm 0.109(\text{tot})\,\text{km/s}. \tag{4}$$

This result is noteworthy since the 10 galaxies used for these measurements have masses spanning three orders of magnitude, and angular momenta spanning five orders of magnitude [2]. Note that the correction in **Table 1** has allowed us to include galaxy NGC 2841 in the average (this galaxy was excluded in [2] because the first measured point at $r_{\min}$ is at the edge of the galaxy core).

The expansion parameter $a_{h\text{NR}}$ at which dark matter becomes non-relativistic can be estimated from (3) as

Table 2. Presented are $\langle v_{th}^2 \rangle'^{1/2}$ from **Table 1** of [2], and $v_{h\text{rms}}(1)$ defined in (2). $\rho_h(0)$ is taken from **Table 1**. $\kappa_h = 0.15 \pm 0.15(\text{syst})$ [2]. The statistical uncertainties of $\langle v_{th}^2 \rangle'^{1/2}$ and $\rho_h(0)$ are correlated [2]. The systematic uncertainty includes contributions from **Table 1** and from κ_h. The χ^2 of these 10 measurements is $\chi^2 = 36.4$, so the total uncertainty of the average has been multiplied by $\left[36.4/(10-1)\right]^{1/2} = 2.0$, as recommended in [3].

Galaxy	$\langle v_{th}^2 \rangle'^{1/2}$ [km/s]	$v_{h\text{rms}}(1)$ [km/s]
NGC 2403	101 ± 3	$1.103 \pm 0.083(\text{stat}) \pm 0.088(\text{syst})$
NGC 2841	220 ± 3	$1.900 \pm 0.047(\text{stat}) \pm 0.232(\text{syst})$
NGC 2903	142 ± 3	$1.377 \pm 0.095(\text{stat}) \pm 0.106(\text{syst})$
NGC 2976	129 ± 177	$1.921 \pm 3.061(\text{stat}) \pm 0.144(\text{syst})$
NGC 3198	104 ± 3	$1.417 \pm 0.112(\text{stat}) \pm 0.139(\text{syst})$
NGC 3521	153 ± 10	$1.250 \pm 0.227(\text{stat}) \pm 0.095(\text{syst})$
NGC 3621	126 ± 5	$2.092 \pm 0.202(\text{stat}) \pm 0.159(\text{syst})$
DDO 154	36.5 ± 3.7	$0.783 \pm 0.137(\text{stat}) \pm 0.062(\text{syst})$
NGC 5055	144 ± 4	$1.024 \pm 0.091(\text{stat}) \pm 0.113(\text{syst})$
NGC 7793	85.5 ± 5.0	$0.977 \pm 0.115(\text{stat}) \pm 0.076(\text{syst})$
Average		$1.192 \pm 0.109(\text{tot})$

$$a_{h\mathrm{NR}} \approx \frac{v_{h\mathrm{rms}}(1)}{c}. \tag{5}$$

There are threshold factors of O(1) presented in Section 5.

4. Dark Matter Mass m_h

We consider the scenario with dark matter dominated by a single type of particle (plus anti-particle) of mass m_h. The mass density of a non-relativistic gas of fermions or bosons with chemical potential μ can be written as [4]

$$\rho_h = \left\langle v_{rh}^2 \right\rangle^{3/2} \frac{N_{f,b} m_h^4}{(2\pi)^{3/2} \hbar^3} \Sigma_{f,b}, \tag{6}$$

where the sums are

$$\Sigma_{f,b} = \frac{e^{\mu'}}{1^{3/2}} \mp \frac{e^{2\mu'}}{2^{3/2}} + \frac{e^{3\mu'}}{3^{3/2}} \mp \frac{e^{4\mu'}}{4^{3/2}} + \cdots, \tag{7}$$

where $\mu' \equiv \mu/(kT_h)$, with upper signs for fermions, and lower signs for bosons. The sums for fermions and bosons are $\Sigma_f = 0.76515$ and $\Sigma_b = 2.612$ for chemical potential $\mu = 0$. N_f (N_b) is the number of fermion (boson) degrees of freedom. From (2) and (6) we obtain

$$m_h = \left[\frac{(6\pi)^{3/2} \Omega_c \rho_{\mathrm{crit}} \hbar^3}{v_{h\mathrm{rms}}(1)^3 N_{f,b} \Sigma_{f,b}} \right]^{1/4}. \tag{8}$$

Note that the measured m_h is independent of $\Omega_c \rho_{\mathrm{crit}}$, see (2). From (4) and (8) we obtain

$$m_h = (53.5 \pm 3.6(\mathrm{tot})\,\mathrm{eV}) \cdot \left(\frac{2}{N_f} \frac{0.76515}{\Sigma_f} \right)^{1/4}, \tag{9}$$

for fermions, and

$$m_h = (46.8 \pm 3.2(\mathrm{tot})\,\mathrm{eV}) \cdot \left(\frac{1}{N_b} \frac{2.612}{\Sigma_b} \right)^{1/4}, \tag{10}$$

for bosons. Note that we have obtained these results directly from the fits to the spiral galaxy rotation curves, with no input from cosmology. The uncertainties in (9) and (10) include all statistical and systematic uncertainties listed in Table 1 and Table 2.

A non-relativistic non-degenerate ideal gas has

$$\frac{\mu}{kT_h} = -\ln\left(\frac{v}{v_Q} \right), \tag{11}$$

where $v \equiv V/N$ is the volume per particle, and $v_Q \equiv \left[2\pi\hbar^2/(m_h kT_h) \right]^{3/2}$ is the "quantum volume". For a non-degenerate ideal gas, $v/v_Q \gg 1$ so the chemical potential μ is negative, and increases logarithmically with particle concentration. Fermi-Dirac or Bose Einstein degeneracy sets in as $\mu \to 0$. Note that in an adiabatic expansion $\mu/(kT_h)$ is constant.

Fitting spiral galaxy rotation curves, we obtain limits $m_h > 16\,\text{eV}$ for fermions, and $m_h > 45\,\text{eV}$ for bosons, at 99% confidence [2]. Equivalently, from (9) and (10), we obtain $\Sigma_f \lesssim 96$ for $N_f = 2$, and $\Sigma_b \lesssim 3.1$ for $N_b = 1$.

5. Transition from Ultra-Relativistic to Non-Relativistic Dark Matter

Consider dark matter in statistical equilibrium with chemical potential μ and temperature T_h. This assumption is justified by the observed Boltzmann distribution of the dark matter [2]. We apply periodic boundary conditions in an expanding cube of volume a^3V. The comoving number density of dark matter particles is [4]:

$$n_h a^3 = \frac{N_{f,b}}{(2\pi\hbar)^3}\int_0^\infty 4\pi p^2 \mathrm{d}p \frac{1}{\exp\left[\left(\sqrt{m_h^2c^4 + p^2c^2/a^2} - m_hc^2 - \mu\right)\Big/\left(kT_h\right)\right] \pm 1}. \quad (12)$$

The last factor is the average number of fermions (upper sign) or bosons (lower sign) in an orbital of momentum p/a.

Now let dark matter decouple while ultra-relativistic, and assume no self-annihilation. Then $n_h a^3$ is conserved. In an adiabatic expansion, e.g. collisionless dark matter, the number of dark matter particles in an orbital is constant so μ and T_h adjust accordingly. The problem has one degree of freedom, so we choose, without loss of generality, $\mu' \equiv \mu/(kT_h)$ constant. $T_h \propto 1/a$ in the ultra-relativistic limit ($kT_h \gg mc^2$), and $T_h \propto 1/a^2$ in the non-relativistic limit ($kT_h \ll mc^2$). (In the transition between these two limits T_h is momentum dependent.) Let us define $x \equiv pc/(akT_h)$, and $y^2 \equiv p^2/(2m_h a^2 kT_h)$. In the ultra-relativistic limit

$$n_h a^3 = A_{f,b} N_{f,b} \left(\frac{kaT_h}{\hbar c}\right)^3, \quad A_{f,b} = \frac{1}{2\pi^2}\int_0^\infty \frac{x^2\mathrm{d}x}{\exp\left[x - \mu'\right] \pm 1}. \quad (13)$$

In the non-relativistic limit

$$n_h a^3 = \Sigma_{f,b} N_{f,b} \left(\frac{m_h k a^2 T_h}{2\pi\hbar^2}\right)^{3/2}, \quad \Sigma_{f,b} = \frac{4}{\pi^{1/2}}\int_0^\infty \frac{y^2\mathrm{d}y}{\exp\left[y^2 - \mu'\right] \pm 1}, \quad (14)$$

as in (6). The intercept of these two asymptotes *defines* $a_{h\text{NR}}$ and $T_{h\text{NR}} \equiv T_h(a_{h\text{NR}}) = T_h(1)/a_{h\text{NR}}^2$:

$$m_h c^2 = 2\pi\left(\frac{A_{f,b}}{\Sigma_{f,b}}\right)^{2/3} kT_{h\text{NR}}, \quad (15)$$

$$a_{h\text{NR}} = \left(\frac{2\pi}{3}\right)^{1/2}\left(\frac{A_{f,b}}{\Sigma_{f,b}}\right)^{1/3}\frac{v_{h\text{rms}}(1)}{c}. \quad (16)$$

For $\mu = 0$, we obtain for fermions $A_f = 0.09135$, $\Sigma_f = 0.76515$, $m_h c^2 = 1.523 kT_{h\text{NR}}$, and $a_{h\text{NR}} = 0.7126 v_{h\text{rms}}(1)/c$; and for bosons $A_b = 0.1218$, $\Sigma_b = 2.612$, $m_h c^2 = 0.8139 kT_{h\text{NR}}$, and $a_{h\text{NR}} = 0.5209 v_{h\text{rms}}(1)/c$. Einstein condensation sets in at $\mu = 0$.

For $\mu/(kT_h) = -1.5$ we obtain for fermions $A_f = 0.0220$, $\Sigma_f = 0.2074$, $m_h c^2 = 1.409 kT_{h\mathrm{NR}}$, and $a_{h\mathrm{NR}} = 0.6852 v_{h\mathrm{rms}}(1)/c$; and for bosons $A_b = 0.02328$, $\Sigma_b = 0.2432$, $m_h c^2 = 1.315 kT_{h\mathrm{NR}}$, and $a_{h\mathrm{NR}} = 0.6620 v_{h\mathrm{rms}}(1)/c$.

For $\mu/(kT_h) = -10.0$ we obtain for both fermions and bosons $A_{f,b} = 4.6\times10^{-6}$, $\Sigma_{f,b} = 4.5\times10^{-5}$, $m_h c^2 = 1.366 kT_{h\mathrm{NR}}$, and $a_{h\mathrm{NR}} = 0.6747 v_{h\mathrm{rms}}(1)/c$.

In summary, from the measured adiabatic invariant $v_{h\mathrm{rms}}(1)$ we obtain m_h and $a_{h\mathrm{NR}}$ with (8) and (16) respectively. The ratio T_h/T of dark matter-to-photon temperatures, after e^+e^- annihilation while dark matter is still ultra-relativistic, is

$$\frac{T_h}{T} = \frac{1}{2\pi}\left(\frac{\Sigma_{f,b}}{A_{f,b}}\right)^{2/3} \frac{a_{h\mathrm{NR}} m_h c^2}{kT_0}, \tag{17}$$

where the photon temperature is $T = T_0/a$. Note that T_h/T is proportional to $v_{h\mathrm{rms}}(1)^{1/4}$, and is proportional to $1/T_0$. The intercept of the two asymptotes that we implemented allows direct comparison of (17) with T_h/T in Table 7 of [2].

6. Results for the Case $\mu = 0$

We now specialize to the case of zero chemical potential $\mu = 0$ corresponding, in particular, to equal numbers of dark matter particles and anti-particles, or to Majorana sterile neutrinos [5], or to dark matter that was once in diffusive equilibrium with the Standard Model sector. We obtain from the measured adiabatic invariant $v_{h\mathrm{rms}}(1)$:

$$m_h = \left[53.5 \pm 3.6(\mathrm{tot})\right] \cdot \left(\frac{2}{N_f}\right)^{1/4} \mathrm{eV}, \tag{18}$$

$$a_{h\mathrm{NR}} = \left[2.83 \pm 0.26(\mathrm{tot})\right] \times 10^{-6}, \tag{19}$$

$$\frac{T_h}{T} = \left[0.423 \pm 0.010(\mathrm{tot})\right] \cdot \left(\frac{2}{N_f}\right)^{1/4} \tag{20}$$

for fermions, or

$$m_h = \left[46.8 \pm 3.2(\mathrm{tot})\right] \cdot \left(\frac{1}{N_b}\right)^{1/4} \mathrm{eV}, \tag{21}$$

$$a_{h\mathrm{NR}} = \left[2.07 \pm 0.19(\mathrm{tot})\right] \times 10^{-6}, \tag{22}$$

$$\frac{T_h}{T} = \left[0.507 \pm 0.012(\mathrm{tot})\right] \cdot \left(\frac{1}{N_b}\right)^{1/4} \tag{23}$$

for bosons. These uncertainties are valid for the considered scenario and include statistical uncertainties and all identified systematic uncertainties listed in **Table 1** and **Table 2**. Systematic uncertainties unknown at present may be needed in the future.

These results can be compared with expectations in Table 7 of [2] (and its extensions for other N_f and N_b). Note that T_h/T is proportional to $v_{h\mathrm{rms}}(1)^{1/4}$,

and proportional to $1/T_0$, so it is highly significant that the measured $v_{h\mathrm{rms}}(1)$ obtains $T_h/T \approx 0.4$ for $\mu = 0$. A different measured $v_{h\mathrm{rms}}(1)$, or a different T_0, would have lead to the conclusion that $\mu \neq 0$ and/or dark matter was never in thermal equilibrium with the Standard Model sector. In conclusion, the measured value of $v_{h\mathrm{rms}}(1)$ is strong evidence that $\mu = 0$ and that dark matter was in thermal equilibrium with the Standard Model sector at some time in the early history of the Universe.

Measurements with individual spiral galaxies for the case of fermions with $N_f = 2$, e.g. sterile Majorana neutrinos, are presented in Table 3.

7. Additional Systematic Uncertainties?

Non-spherical spiral galaxies: Equations (3) to (6) of [2] are valid in general. So long as the numerical integration is along a radial direction in the plane of the galaxy, with $\nabla P_h = \hat{\boldsymbol{e}}_r \, \mathrm{d}P_h/\mathrm{d}r$ and $\nabla \cdot \boldsymbol{g}_h = \left(1/r^2\right)\mathrm{d}\left(r^2 g_h\right)/\mathrm{d}r$, and similarly for baryons, there is no approximation, and no systematic uncertainty is needed.

Mixing of dark matter: So long as dark matter is assumed collisionless, the adiabatic invariant $v_{h\mathrm{rms}}(1)$ should be exactly conserved, so we assign no systematic uncertainty to Equation (3).

New studies may require additional systematic uncertainties. However, at present we do not identify any.

Table 3. Measurements of the expansion parameter $a_{h\mathrm{NR}}$ at which dark matter becomes non-relativistic, the dark matter particle mass m_h, and the ratio of temperatures T_h/T of dark matter-to-photons after e^+e^- annihilation and before dark matter becomes non-relativistic. In this table the particles of dark matter are assumed to be fermions with $N_f = 2$ and $\mu = 0$. The 1σ total uncertainties include the statistical and systematic uncertainties of $v_{h\mathrm{rms}}(1)$ in Table 2. The χ^2's are 36.4, 40.8, and 40.4 respectively, for 10 - 1 degrees of freedom, so the uncertainties of the averages have been multiplied by $\left[\chi^2/(10-1)\right]^{1/2}$, as recommended in [3].

Galaxy	$10^6 \times a_{h\mathrm{NR}}$	m_h [eV]	T_h/T
NGC 2403	2.62 ± 0.29	56.7 ± 4.6	0.415 ± 0.011
NGC 2841	4.52 ± 0.56	37.7 ± 3.5	0.476 ± 0.015
NGC 2903	3.27 ± 0.34	48.0 ± 3.7	0.439 ± 0.011
NGC 2976	4.57 ± 7.28	37.4 ± 44.7	0.477 ± 0.190
NGC 3198	3.37 ± 0.42	47.0 ± 4.4	0.442 ± 0.014
NGC 3521	2.97 ± 0.59	51.6 ± 7.6	0.428 ± 0.021
NGC 3621	4.97 ± 0.61	35.1 ± 3.2	0.487 ± 0.015
DDO 154	1.86 ± 0.36	73.3 ± 10.5	0.381 ± 0.018
NGC 5055	2.43 ± 0.34	59.9 ± 6.3	0.408 ± 0.014
NGC 7793	2.32 ± 0.33	62.1 ± 6.6	0.403 ± 0.014
Average	2.83 ± 0.26	46.1 ± 3.3	0.432 ± 0.010

8. Conclusions

A numerical integration obtains rotation curves for spiral galaxies [2]. This integration requires four parameters (boundary conditions). These parameters are obtained by a fit that minimizes the χ^2 between the observed [1] and calculated rotation curves. The fits for ten spiral galaxies, as well as the fitted parameters, are presented in Reference [2]. The fits are in agreement with observations within observational uncertainties. Two of the measured parameters, that are of interest to the present analysis, are $\rho_h(r_{\min})$ and $\langle v_{rh}^2 \rangle'^{1/2}$, and are presented in Table 1 and Table 2. From these two parameters we calculate the adiabatic invariant $v_{h\mathrm{rms}}(1)$ defined in (2). Measurements of $v_{h\mathrm{rms}}(1)$ for ten spiral galaxies are presented in Table 2. We obtain an average

$$v_{h\mathrm{rms}}(1) = 1.192 \pm 0.109(\mathrm{tot})\,\mathrm{km/s}. \tag{24}$$

This result is remarkable considering that the ten galaxies span three orders of magnitude in mass, and five orders of magnitude in angular momenta [2].

We consider dark matter that is dominated by a single type of particle of mass m_h. We assume that dark matter decoupled from the Standard Model sector and from self-annihilation while still ultra-relativistic. Then from $v_{h\mathrm{rms}}(1)$ we obtain directly the expansion parameter at which dark matter becomes non-relativistic:

$$a_{h\mathrm{NR}} \approx \frac{v_{h\mathrm{rms}}(1)}{c}, \tag{25}$$

up to a threshold factor of O(1) presented in Section 5. From the adiabatic invariant $v_{h\mathrm{rms}}(1)$ we also obtain the mass m_h of dark matter particles, as a function of the chemical potential μ, with no input from cosmology, see (8).

The fits to spiral galaxy rotation curves allow us to set lower bounds to the dark matter particle mass m_h [2], and upper bounds to the dark matter chemical potential μ, that are not much greater than zero.

To proceed, we need to know the chemical potential μ of dark matter. We consider the scenario with $\mu = 0$ which is appropriate for equal numbers of dark matter particles and anti-particles, or Majorana sterile neutrinos [5], or dark matter that was once in diffusive equilibrium with the Standard Model sector. The upper bound to μ, obtained from the spiral galaxy rotation curves, is close to zero. A negative chemical potential would imply a dark matter temperature while ultra-relativistic higher than the temperature of the Standard Model sector, which seems implausible. In any case we proceed assuming $\mu = 0$, and obtain the results (18) to (23).

The ratio T_h/T is proportional to $v_{h\mathrm{rms}}(1)^{1/4}$, and proportional to $1/T_0$, so the result $T_h/T \approx 0.4$ is highly significant. A different measured adiabatic invariant $v_{h\mathrm{rms}}(1)$, or a different T_0, could have obtained T_h/T orders of magnitude different from unity, so the measurement $T_h/T \approx 0.4$ is strong evidence that dark matter was once in thermal equilibrium with the Standard Model sector, and gives added support to the scenario $\mu \approx 0$.

We compare the measured T_h/T and m_h with expectations, see Table 7 of [2] (and extensions with other N_f and N_b), and find one very good match: fermion dark matter with $N_f = 2$ that decoupled in the approximate temperature range from the confinement-deconfinement transition to m_s, that suggests Majorana sterile neutrino dark matter [2]; and one marginal match for a boson with $N_b = 3$ that decoupled in the temperature range from m_π to m_c.

Conflicts of Interest

The author declares no conflicts of interest regarding the publication of this paper.

References

[1] de Blok, W.J.G., *et al.* (2008) High-Resolution Rotation Curves and Galaxy Mass Models from THINGS. *The Astronomical Journal*, **136**, 2648-2719. https://doi.org/10.1088/0004-6256/136/6/2648

[2] Hoeneisen, B. (2019) A Study of Dark Matter with Spiral Galaxy Rotation Curves. *International Journal of Astronomy and Astrophysics*, **9**, 71-96. https://doi.org/10.4236/ijaa.2019.92007

[3] Tanabashi, M., *et al.* (Particle Data Group) (2018) The Review of Particle Physics. *Physical Review D*, **98**, Article ID: 030001.

[4] Hoeneisen, B. (1993) Thermal Physics. Mellen Research University Press, San Francisco.

[5] Srivastava, Y.N., Widom, A. and Swain, J. (1997) Thermodynamic Equations of State for Dirac and Majorana Fermions. hep-ph/9709434. http://cds.cern.ch/record/334578/files/9709434.pdf

International Journal of Astronomy and Astrophysics, 2019, 9, 142-153
http://www.scirp.org/journal/ijaa
ISSN Online: 2161-4725
ISSN Print: 2161-4717

AGN Singularities and Jets Modelled with the Superstar Scenario

Ding-Yu Chung

Utica, Michigan, USA
Email: dy_chung@yahoo.com

How to cite this paper: Chung, D.-Y. (2019) AGN Singularities and Jets Modelled with the Superstar Scenario. *International Journal of Astronomy and Astrophysics*, **9**, 142-153.
https://doi.org/10.4236/ijaa.2019.92011

Received: April 1, 2019
Accepted: June 18, 2019
Published: June 21, 2019

Abstract

In this paper we present solutions with the superstar scenario for the problems of singularity and the relativistic jet in AGN (Active Galactic Nuclei) based on supermassive black hole with singularity. The five-zone structure of superstar from inside to outside consists of the Singularity-Free Superstar Core (SC), the short-range repulsive super force field (SFF) near the event horizon, the superstar lepton sphere (SLS) containing infalling leptons (electron-positron pairs), the superstar ergosphere (SE), and the superstar accretion disk (SAD). As in the Meissner effect in superconductor, the short-range SFF repulses leptons in the SLS preventing singularity, while infalling leptons from the SAD and the SE continue to enter the SLS through the strong gravity of the SC. When the density at the bottom of the SLS reaches the critical density, leptons fall into the SC with the corresponding size increase of the SC to prevent singularity. Without further infalling leptons, the short-range repulsive force from the SFF disintegrates the SLS into the SLS plasma fragments (electron-positron pair plasma), detaching from the SC. Some SLS plasma fragments in the SAD generate the broad relativistic SAD jet, and some SLS plasma fragments in the SE generate the coincident narrow relativistic SE jet. In this two-jet model (the origin of the spine-sheath jet structure), protected by the SAD jet, the fast and narrow SE jet inside the slow and broad SAD jet generates the VHE (very high energy ≥ 100 GeV) Synchrotron Self Compton (SSC) gamma-ray emission without the attenuation by the photons in the BLR (broad line region) of flat spectrum radio quasar (FSRQ). In conclusion, AGN based on supermassive superstar provide the solutions for singularity, VHE gamma-ray emissions in FSRQs and FR1 type radio galaxies, AGN jet structure, and AGN jet type.

Keywords

ANG, Relativistic Jet, Superstar, Supermassive, Singularity, Black Hole, Super Force Field, Very High Energy Gamma-Ray Emission

1. Introduction

AGN (Active Galactic Nuclei) is based on supermassive supermassive black hole with singularity. Black hole has been a standard model for the collapse of a large star. Singularity in black hole remains contentious. Gravastar (gravitational vacuum star) [1] [2] by P. O. Mazurand and E. Mottola is a model for the collapse of a large star without singularity. In gravastar, quantum effects would change space-time around a collapsing star, initiating a radical phase transition like when liquid water becomes ice, for some of the infalling matter. For gravastar, the phase transition involves the transformation into a "gravitational vacuum" with an interior de Sitter condensate surrounded by a Bose-Einstein condensate (BEC) bubble, similar to the transformation of a cloud of atoms into one huge "super-atom", a BEC at an extremely low temperature above absolute zero degree. The BEC is prevented from complete collapse by the interior de Sitter condensate exerting a balanced pressure outwards on the condensate. A thin phase boundary (shell) for the phase transition is in between the interior region and the exterior region.

In this paper, superstar without singularity is proposed as an alternative to black hole and gravastar as described in the previous paper [3]. Due to quantum effects, the space-time around gravastar exerts a balanced pressure outwards on gravastar to prevent the complete collapse of gravastar. Similarly, due to quantum effects, the space-time around superstar is the short-range repulsive super force to prevent the complete collapse of superstar. The repulsive effect of the super force field at nearly infinite density is like the repulsive Meissner effect in superconductor to eject applied magnetic fields from the interior of the superconductor at nearly absolute zero temperature as described in the previous paper [4].

This paper describes AGN based on supermassive singularity-free superstar as an alternative to AGN based on supermassive black hole with singularity. AGN produce very high luminosities in a very concentrated volume. In the prevailing model of the physical structure of AGN, at the center is a supermassive black hole (10^6 to 10^{10} $M_\odot$) whose gravitational potential energy is the ultimate source of the AGN luminosity [5]. Matter pulled toward the rotating supermassive black hole form a rotating accretion disk. The region near the accretion disk is the broad line region (BLR) with high-density optical and ultraviolet photons emitted from the accretion disk. The region much farther from the disk is the narrow line region with low-density photons. Outflows of energetic particles in the relativistic collimated jet occur along the poles of the disk. A subset of the jetted AGN is blazar [6] with the relativistic jet closely aligned to the line of sight of the observer. Blazars show the properties of variability at all frequencies-time scales and high polarization at both optical and radio frequencies. Blazars include flat spectrum radio quasars (FSRQs) that show broad optical emission lines and BL Lacertae objects (BL Lacs) with weak or even absence of such emission lines.

The spectral energy distribution (SED) of blazars is dominated by the gam-

ma-ray emission, but the location of the main gamma-ray emitting region in blazars is still uncertain. In the standard scenario of model, the SED of the large majority of gamma-ray detected FSRQ is the BLR External Compton (EC) scenario [7] [8] where the BLR provides effective seed photons for the inverse Compton (IC) scattering by relativistic electrons in the jet. In the recent paper by Costamante, Cutini, Tosti, Antolini, and Tramacere, the BLR-EC scenario is tested [9]. They test this scenario on the Fermi gamma-ray spectra of 106 broad-line blazars detected with the highest significance or largest BLR, by looking for cut-off signatures at high energies compatible with γ-γ interactions with BLR photons, resulting in the attenuation of gamma-ray. They found that only one object out of ten seems compatible with substantial attenuation through the interaction with BLR photons. The one object is below the cut-off energy. They conclude that for 9 out of 10 objects, the jet does not interact with BLR photons to produce gamma-ray. The result is the production of very high energy (VHE, ≥100 GeV) gamma-rays without attenuation, contradicting the BLR-EC scenario. Such VHE gamma-rays have to be produced outside the BLR. However, it is difficult to find a scenario without the involvement of the BLR in FSRQ where the BLR is highly active. As a result, the proper relativistic jet producing VHE gamma-ray emission in FSRQ is still unknown.

This paper proposes that AGN based on supermassive singularity-free superstar provide the solutions for the problems of singularity and the relativistic jet to producing VHE gamma-ray emission in AGN based on supermassive black hole. Section 2 describes black hole and superstar. Section 3 deals with AGN based on supermassive superstar,

2. Black Hole and Superstar

The uncertainty principle in quantum mechanics

$$\sigma_x \sigma_p \geq \frac{\hbar}{2} \tag{1}$$

Postulates that the position, x, and momentum, p, of a particle cannot be simultaneously determined with arbitrarily high precision. In the generalized uncertainty principle [10], an extra term related to the Planck energy is introduced to avoid singularity.

$$\sigma_x \sigma_p \geq \frac{\hbar}{2} + \frac{\alpha G}{c^3} \tag{2}$$

where α is a constant and G relates to the Planck energy, At energy much below the Planck energy, the extra term in Equation (2) is irrelevant and the Heisenberg uncertainty principle is recovered, while approaching the Planck energy, the extra term becomes relevant, and is related to the minimal observable length. In this paper, an extra force field is introduced to maintain the non-zero minimal length and momentum at the extreme conditions such as at the temperature near absolute zero degree ($\sigma_p \approx 0$) and extremely high density ($\sigma_x \approx 0$) when $\sigma_x \sigma_p \approx 0$. This extra force field is the short-range super force field, resulting in su-

perstar and superconductor [3] [4]. Superstar with the short-range super force field to star is like superconductor with the short-range super force field to conductor [4].

The conventional five-zone structure from inside to outside of black hole [11] consists of singularity at the center of black hole,, the event horizon [12], the black hole photon sphere (BHPS) [13], the black hole ergosphere (BHE) [14], and the black hole accretion disk (BHAD) [15] as in **Figure 1**.

Singularity is the region of the black hole where all the mass of the black hole has been compressed down to nearly zero volume with almost infinite density and an enormous gravitational force. As the boundary of the black hole, the event horizon with the Schwarzschild radius preventing any escape of matters and radiation. Adjacent to the event horizon, the surrounding unstable and thin black hole photon sphere (BHPS) with a radius 1.5 times the Schwarzschild radius contains photons travelling in a circular orbit. Outside of the event horizon, a rotating black hole produces black hole ergosphere (BHE) where nothing can remain at rest. Ergosphere has an elliptical shape like a flattened sphere, and the north and south poles of the ergosphere touch the top and bottom of the event horizon. Objects and radiation can escape from ergosphere.

Black hole accretion disk (BHAD) is mostly gas around black holes transports gas to the black hole at their centers. The gas is pulled into the BHAD from infalling star and interstellar material, and the latent angular momentum of gas causes the BHAD to rotate in the shape of pancake. The accreting gas near the black hole event horizon orbits at very high speeds to produce friction, which heats it up so much that individual atoms dissociate into plasma consisting of mostly leptons (electron-positron pairs), some of which fall into black hole. The plasma creates a strong magnetic field around black hole. The BHAD is larger than the BHE, so there is space between the BHAD and the BHE. The region near the accretion disk is the broad line region (BLR) with fast-moving high-density optical and ultraviolet photons emitted from the accretion disk. The region much farther from the disk is the narrow line region with slow-moving low-density photons.

The five-zone structure of superstar is similar to the five-zone structure of black hole. The five-zone structure of superstar from inside to outside consists of the Singularity-Free Superstar Core (SC), the super force field (SFF) as the short-range repulsive force field near the event horizon to separate the SC and

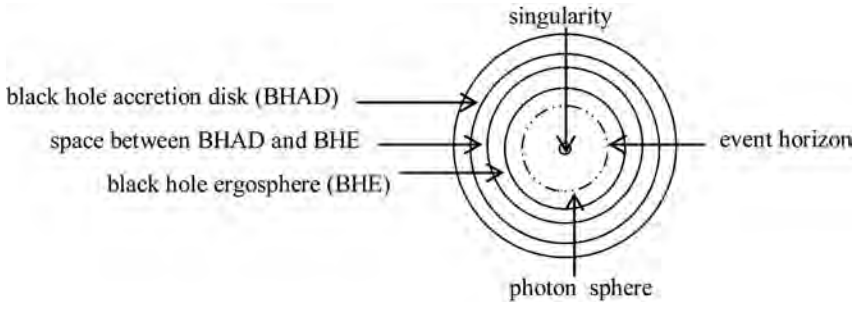

Figure 1. The structure of black hole.

the infalling leptons, the superstar lepton sphere (SLS) to contain infalling leptons, the superstar ergosphere (SE), and superstar accretion disk (SAD) as in Figure 2.

The Schwarzschild radius of a rotating black hole is given as

$$r_s = \frac{GM}{c^2} \tag{2}$$

where G is the gravitational constant, M is the object mass, and c is the speed of light. The radius of the superstar core is equal to or larger than the Schwarzschild radius.

$$r_{\text{superstar core}} \geq \frac{GM}{c^2} \tag{3}$$

The Sun as a superstar has the mass of 1.99×10^{30} kg and the Schwarzschild radius of 2.95×10^{3} m. Supermassive superstars up to 21 billion (2.1×10^{10}) of the mass of the Sun have been detected, such as NGC 4889 with the mass of 4.2×10^{40} kg and the Schwarzschild radius of 6.2×10^{13} m.

3. AGN Based on Supermassive Superstar

The Meissner effect in superconductor is explained by the outward pressure of the super force field to eject applied magnetic fields from the interior of the superconductor as it transitions into the super force field at nearly absolute zero temperature. As in the Meissner effect in superconductor, the super force field in supermassive superstar exerts a short-range repulsive force to repel leptons in the SLS, while infalling leptons from the SAD and the SE continue to enter the SLS through the strong gravity of the SC. When the density at the bottom of the SLS reaches the critical density, leptons fall into the SC with the corresponding size increase of the SC to prevent singularity. Without further infalling leptons, the short-range repulsive force from the super force field disintegrates the SLS to generate the SLS plasma fragments (electron-positron pair plasma) detaching from the SC. When the amount of the SLS plasma fragments is high enough, some SLS plasma fragments in the inner part of the SAD generating the relativistic SAD jet through the process similar to the Blandford-Znajek process [16], and some SLS plasma fragments in the SE generate the coincident relativistic SE jet through the process similar to the Penrose Process [17]. The result is the

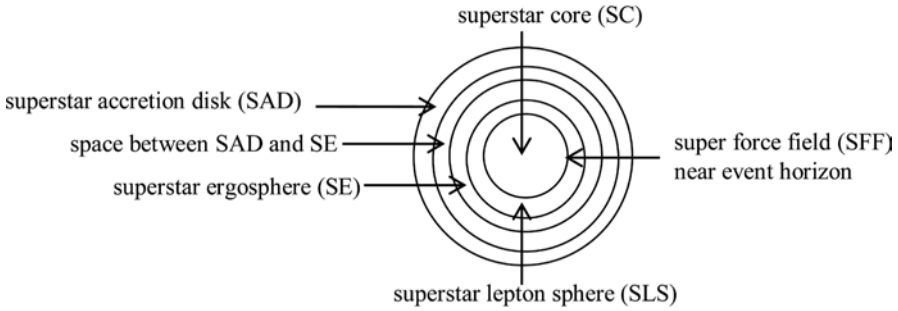

Figure 2. The structure of superstar.

two-jet model based on supermassive superstar.

In the conventional Blandford-Znajek process for the jet from supermassive black hole, the energy of the relativistic jet is extracted from magnetic fields around an accretion disk, which are dragged and twisted by the spin of the supermassive black hole. The Blandford-Znajek process requires an accretion disk with a strong poloidal magnetic field around a rotating supermassive black hole. In the conventional Penrose Process for the jet from supermassive black hole, the energy of the relativistic jet is extracted from the negative-energy particles produced in the ergosphere. The Penrose Process requires the breakup (spontaneous fission) of particles at relativistic speeds in opposite directions in the ergosphere. Parfrey, Philippov, and Cerutti recently present general-relativistic collisionless plasma simulations [18] of rotating supermassive black hole magnetospheres which begin from vacuum, inject electron-positron pair plasma near the event horizon, and reach steady states with electromagnetically powered Blandford-Znajek jets that occurs at north and south poles. Near the supermassive black hole's midsection in the ergosphere, magnetic field lines operating in opposing directions like a two-lane highway meet at the equator. This congregation causes the lines to twist and tangle. In the space between these bundles, the electric field accelerates particles. Some fly outward, following a curved trajectory into the peripheries of the polar jets. Others speed into the supermassive black hole, resulting in the Penrose process. Overall, the simulations suggest that roughly 80% of the jet's energy comes from Blandford-Znajekwith the remaining 20% originating from the Penrose process. The computer simulation by Parfrey, Philippov, and Cerutti produces the two-jet model based on supermassive black hole.

For the two-jet model based on superstar, the main energy sources of both SAD jet and SE jet are the SLS plasma fragments (electron-positron pair plasma), and the formations of the jets are derived from the rotating SE/SAD. Because the inner portions of the lepton layers on the SE/SAD are rotating more quickly than the outer portions, the magnetic field lines twist violently. This causes the jets of leptons to blast outward at almost the speed of light perpendicularly to the SE/SAD, similar to the Blandford-Znajek process and Penrose process. The SLS plasma fragments provide sufficient energies to produce large scale relativistic jets. Furthermore, the short-range repulsive force of the super force field also avoids the adsorption of the SLS plasma fragments by the SC, unlike the Blandford-Znajek process and Penrose process with supermassive black hole to adsorb plasma. As a result, AGN based on supermassive superstar allows large-scale relativistic jets. Some computer simulations of AGN jet based on supermassive black hole that do not have unlimited plasma and the Penrose process as the simulation by Parfrey, Philippov, and Cerutti cannot generate large-scale jets [19].

The jet from the SLS plasma fragments is similar to the jet from a symbiotic binary which usually contains a white dwarf with a companion red giant [20]. A

red giant loses its material through the flow to the white dwarf nearby via an accretion disk. Some symbiotic stars have jets which are bi-polar and extend from both poles of the white dwarf. Therefore, the red giant is like the SLS as the source of the SLS plasma fragments, while the accretion disk of the white dwarf is like the SE/SAD. However, the strong gravity of supermassive superstar prevents the escape of material through the jet formation directly and initially from the infalling star as in a symbiotic binary. The SLS plasma fragments inside the structure of supermassive superstar provide the critical mass in a small area to generate a large scale jet.

The distance between the SAD and the SAD jet is much larger than the distance between the SC and the SE jet, so the leptons from the SAD travels longer distance from the SAD than from the SC to form the jets in the high-density BLR. As a result, the SAD jet is the slow jet with the low Lorentz factor, and the SE jet is the fast jet with the high Lorentz factor. Due to the longer distance between the SAD and the SAD jet than the distance between the SC and the SE jet, the radius of the SAD jet is larger than the radius of the SE jet. Therefore, the fast and narrow SE jet is inside the coincident slow and broad SAD jet as the two-jet model in Figure 3.

In this two-jet model, the relativistic leptons in the fast SE jet up-scatter radiation from the slow moving SAD jet to produce gamma-ray as in the Synchrotron Self Compton (SSC) model [21]. In the SSC model, the seed photons for the Inverse Compton (IC) process producing gamma-ray are the synchrotron photons produced by the relativistic leptons. This two-jet model is similar to the two-blob model proposed by Georganopoulos *et al.* [22] in which radiation from the slow blob II is up-scattered by the relativistic mono-directional leptons in the fast blob I. The two-blob model by Georganopoulos *et al.* fits the SED well.

The slow SAD jet generates mostly the low frequency emissions and occasionally low-energy gamma-ray emissions through the inverse Campton scattering with the photons in the high-density BLR, while under the protection by the SAD jet, the fast SE jet inside the slow SAD jet generates the VHE SSC emission without the attenuation by the high-density photons in the BLR of FSRQ. Therefore, the two-jet model of the SAD jet and the SE jet provides the solution for the relativistic producing the VHE gamma-ray emissions in FSRQ.

The two-jet model also explains VHE gamma-rays [23] in FR1 type radio galaxies which jets aligned at large angles to the line of sight. In the two-jet model, the SAD jet producing VHE gamma-rays in FR1 type radio galaxies is the very

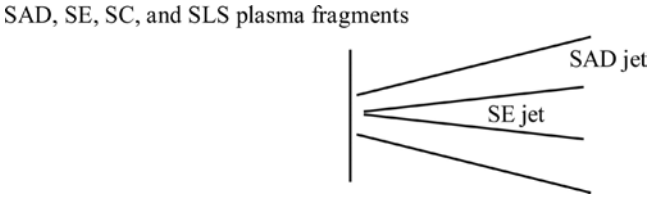

Figure 3. The two-jet model: the fast and narrow SE jet from the SC is inside of the slow and broad SAD jet from the SAD.

slow SAD jet through the very high-density BLR. As the very slow SAD jet moves through the very high-density BRL, the fast-moving photons in the very high-density BLR deaccelerate the very slow SAD jet, and change the mono-directional leptons in the SAD jet into multi-directional leptons. Subsequently, some multi-directional leptons in the SAD jet in the narrow line region produce VHE gamma-rays by up-scattering mono-directional soft radiation from the SE jet preferentially in the direction opposite to the SE jet motion. Therefore, VHE gamma-rays which are produced in the SAD jet without the attenuation from the photons in the low-density narrow line region can be emitted at a relatively large angle to the jet axis in the observer's reference frame. This two-jet model is similar to the two-blob model proposed by Banasinski and Bednarek [24] in which radiation from the fast blob I is up-scattered by the relativistic isotropic (multi-directional) leptons in the slow blob II. The two-blob model by Banasinski and Bednarek fits the SED well. Therefore, the two-jet model of the very slow SAD jet and the SE jet provides the solution for the relativistic jet producing the VHE gamma-ray emissions in FR1 type radio galaxies.

The currents carried by the AGN jets can be probed using maps of the Faraday rotation measure (RM), since a jet current are accompanied by a toroidal magnetic field, which gives rise to a systematic change in the RM across the jet [25]. The collected data indicate that AGN jets reveal strong signs of the spine-sheath jet structure with a central spine of orthogonal magnetic field and a sheath of longitudinal magnetic field along the edges of the jet [26]. They suggest that the inner region of the jet spine consists of a low-density and fast-moving gas, while the outer region of the jet sheath consists of a denser and slower moving gas [27] The spine-sheath jet structure can also be explained by the coaxial cable proposed by Gabuzda [28] [29]. Like coaxial cable with the inner conductor and the outer shield sharing a geometric axis, an AGN jet has an inward current along its axis and an outward current in a more extended sheath-like region surrounding the jet. The current typically flows inward along the jet axis and outward in a more extended region surrounding the jet, typical to the current structure of a coaxial cable, accompanied by a self-consistent system of nested helical magnetic fields, whose toroidal components give rise to the observed transverse RM gradients. These data conclusively demonstrate the existence of the coaxial currents of AGN jets. The origin of the spine-sheath jet structure can be explained by the two-jet model. The spine (inward current) and the sheath (outward current) in the spine-sheath jet structure model are derived from the SE jet and SAD jet, respectively, in the two-jet model.

The amount of the SLS plasma fragments is determined by the thicknesses of the SLS derived from the mass of infalling star and interstellar material. The SLS plasma fragments stay around the SE/SAD through gravity until they escape through the relativistic jets. The jets have limited capacities to carry leptons. Therefore, the timescale of the jet is determined by the amount of the SLS plasma fragments which is determined by the thickness of the SLS derived from the

mass of infalling star and interstellar material. When the amount of the SLS plasma fragments becomes insufficient to generate the jet, the jet ends. The SLS plasma fragment remnants (electron-positron pairs) become the fast-moving photons in the BLR. The SAD, the SE, and the SLS maintain the minimum amounts of leptons in the equilibrium state among gravity, angular momentum, and the short-range repulsive force of the super force field. The fast-moving photons from the SLS fragment plasma remnants in the BLR gradually move away from the BLR. This process repeats for another occurrence of infalling star and interstellar material. The amount of the photons from the SLS plasma fragment remnants is determined by the frequency of the occurrence of infalling star and interstellar material. The jetted AGN with frequent occurrences of infalling star and interstellar material are FSRQs with the high amount of photons from the SLS plasma fragment remnants in the BLR, while the jetted AGN with infrequent occurrences are BL Lacertae objects with the low amount of photons from the SLS plasma fragment remnants in the BLR. The result is the blazar sequence as the sequence of the amounts of photons surrounding the jets [30].

4. Conclusions

In this paper we present solutions for the problems of singularity and the relativistic jet in AGN (Active Galactic Nuclei) based on supermassive black hole with singularity. The five-zone structure of superstar from inside to outside consists of the Singularity-Free Superstar Core (SC), the short-range repulsive super force field (SFF) near the event horizon, the superstar lepton sphere (SLS) containing infalling leptons (electron-positron pairs), the superstar ergosphere (SE), and the superstar accretion disk (SAD). As in the Meissner effect in superconductor, the short-range SFF repulses leptons in the SLS preventing singularity, while infalling leptons from the SAD and the SE continue to enter the SLS through the strong gravity of the SC. When the density at the bottom of the SLS reaches the critical density, leptons fall into the SC with the corresponding size increase of the SC to prevent singularity.

Without further infalling leptons, the short-range repulsive force from the SFF disintegrates the SLS into the SLS plasma fragments (electron-positron pair plasma), detaching from the SC. Some SLS plasma fragments in the SAD generate the broad relativistic SAD jet, and some SLS plasma fragments in the SE generate the coincident narrow relativistic SE jet. In this two-jet model (the origin of the spine-sheath jet structure), protected by the SAD jet, the fast and narrow SE jet inside the slow and broad SAD jet generates the VHE (very high energy ≥ 100 GeV) Synchrotron Self Compton (SSC) gamma-ray emission without the attenuation by the photons in the BLR (broad line region) of flat spectrum radio quasar (FSRQ). The two-jet model of the very slow SAD jet and the SE jet also provides the solution for the relativistic jet producing the VHE gamma-ray emissions in FR1 type radio galaxies.

An important theory on the jet structure is the spine-sheath jet structure. The

origin of the spine-sheath jet structure can be explained by the two-jet model. The spine and the sheath in the spine-sheath jet structure model are derived from the SE jet and SAD jet, respectively, in the two-jet model. The timescale of the jet is determined by the amount of the SLS plasma fragments which is determined by the thickness of the SLS derived from the mass of infalling star and interstellar material. When the amount of the SLS plasma fragments becomes insufficient to generate the jet, the jet ends. The SLS plasma fragment remnants (electron-positron pairs) become the fast-moving photons in the BLR. The jetted AGN with frequent occurrences of infalling star and interstellar material are FSRQs with the high amount of photons from the SLS plasma fragment remnants in the BLR, while the jetted AGN with infrequent occurrences are BL Lacertae objects with the low amount of photons from the SLS plasma fragment remnants in the BLR. The result is the blazar sequence as the sequence of the amounts of photons surrounding the jets. In conclusion, AGN based on supermassive superstar provide the solutions for singularity, VHE gamma-ray emissions in FSRQs and FR1 type radio galaxies, AGN jet structure, and AGN jet type.

Conflicts of Interest

The author declares no conflicts of interest regarding the publication of this paper.

References

[1] Mazur, P. and Mottola, E. (2004) Gravitational Vacuum Condensate Stars. *Proceedings of the National Academy of Science of the United States of America*, **101**, 9545-9550. https://doi.org/10.1073/pnas.0402717101

[2] Mazur, P. and Mottola, E. (2015) Surface Tension and Negative Pressure Interior of a Non-Singular 'Black Hole'. *Classical and Quantum Gravity*, **32**, Article ID: 215024. https://doi.org/10.1088/0264-9381/32/21/215024

[3] Chung, D. and Krasnoholovets, V. (2013) Singularity-Free Superstar as an Alternative to Black Hole and Gravastar. *Journal of Modern Physics*, **4**, 1-6. https://doi.org/10.4236/jmp.2013.47A1001

[4] Chung, D. (2015) The Basic Cause of Superconductivity. *Journal of Modern Physics*, **6**, 26-36. https://doi.org/10.4236/jmp.2015.61005

[5] Kazanas, D. (2012) Toward a Unified AGN Structure. *Astronomical Review*, **7**, 92-123. https://doi.org/10.1080/21672857.2012.11519707

[6] Urry, C. and Padovani, P. (1995) Unified Schemes for Radio-Loud Active Galactic Nuclei. *Publications of the Astronomical Society of the Pacific*, **107**, 803-845. https://doi.org/10.1086/133630

[7] Sikora, M., Begelman, M. and Rees, M. (1994) Comptonization of Diffuse Ambient Radiation by a Relativistic Jet: The Source of Gamma Rays from Blazars? *Astrophysical Journal*, **421**, 153-162. https://doi.org/10.1086/173633

[8] Sikora, M., Stawarz, Ł., Moderski, R., Nalewajko, K. and Madejski, G.M. (2009) Constraining Emission Models of Luminous Blazar Sources. *The Astrophysical Journal*, **704**, 38-50. https://doi.org/10.1088/0004-637X/704/1/38

[9] Costamante, L., Cutini, S., Tosti, G., Antolini, E. and Tramacere, A. (2018) On the Origin of Gamma Rays in *Fermi* Blazars: Beyond the Broad Line Region. *Monthly Notices of the Royal Astronomical Society*, **477**, 4749-4767. https://doi.org/10.1093/mnras/sty887

[10] Capozziello, S., Lambiase, G. and Scarpetta, G. (2000) Generalized Uncertainty Principle from QuantumGeometry. *International Journal of Theoritical Physics*, **39**, 15-22. https://doi.org/10.1023/A:1003634814685

[11] Iyer, B. and Bhawal, B. (1999) Black Holes Gravitational Radiation and the Universe. Springer, New York. https://doi.org/10.1007/978-94-017-0934-7

[12] Chaisson, E. (1990) Relatively Speaking: Relativity, Black Holes, and the Fate of the Universe. W. W. Norton & Company, New York.

[13] Teo, E. (2003) Spherical Photon Orbits around a Kerr Black Hole. *General Relativity and Gravitation*, **35**, 1909-1926. https://doi.org/10.1023/A:1026286607562

[14] Visser, M. and Williams, T. (2008) The Kerr Spacetime: A Brief Introduction. Oxford Scholarship Online, Oxford. https://doi.org/10.1093/acprof:oso/9780195309386.003.0001

[15] Wagoner, R. (2008) Relativistic and Newtonian Diskoseismology. *New Astronomy Reviews*, **51**, 828-834. https://doi.org/10.1016/j.newar.2008.03.012

[16] Blandford, R. and Znajek, R. (1977) Electromagnetic Extraction of Energy from Kerr Black Holes. *Monthly Notices of the Royal Astronomical Society*, **179**, 433-456. https://doi.org/10.1093/mnras/179.3.433

[17] Penrose, R. (1969) Gravitational Collapse: The Role of General Relativity. *La Rivista del Nuovo Cimento*, **1**, 252-276.

[18] Parfrey, K., Philippov, A. and Cerutti, B. (2019) First-Principles Plasma Simulations of Black-Hole Jet Launching. *Physics Review Letters*, **122**, Article ID: 035101. https://doi.org/10.1103/PhysRevLett.122.035101

[19] Komissarov, S. (2005) Observations of the Blandford-Znajek Process and the Magnetohydrodynamic Penrose Process in Computer Simulations of Black Hole Magnetospheres. *Monthly Notices of the Royal Astronomical Society*, **359**, 801-808. https://doi.org/10.1111/j.1365-2966.2005.08974.x

[20] Mikołajewska, J. (2002) Orbital and Stellar Parameters of Symbiotic Stars. *ASP Conference Series*, **303**, 9-24

[21] Jones, T., O'dell, S. and Stein, W. (1974) Physics of Compact Nonthermal Sources. I. Theory of Radiation Processes. *Astrophysical Journal*, **188**, 353-368. https://doi.org/10.1086/152724

[22] Georganopoulos, M., Perlman, E.S. and Kazanas, D. (2005) Is the Core of M87 the Source of Its TeV Emission? Implications for Unified Schemes. *The Astrophysical Journal*, **634**, L33-L36. https://doi.org/10.1086/498714

[23] Aliu, E., *et al.* (2012) Veritas Observations of Day-Scale Flaring of M 87 in 2010 April. *The Astrophysical Journal*, **746**, 141.

[24] Banasinski, P. and Bednarek, W. (2018) Two Blobs in a Jet Model for the γ-Ray Emission in Radio Galaxies. *The Astrophysical Journal*, **864**, 128. https://doi.org/10.3847/1538-4357/aad4fa

[25] Broderick, A. and Loeb, A. (2009) Signatures of Relativistic Helical Motion in the Rotation Measures of Active Galactic Nucleus Jets. *The Astrophysical Journal Letters*, **703**, L104-L108. https://doi.org/10.1088/0004-637X/703/2/L104

[26] Gabuzda. D., Reichstein, A. and O'Neill, E. (2014) Are Spine-Sheath Polarization Structures in the Jets of Active Galactic Nuclei Associated with Helical Magnetic

Fields? *Monthly Notices of the Royal Astronomical Society*, **444**, 172-184. https://doi.org/10.1093/mnras/stu1381

[27] Walg, S., *et al.* (2013) Relativistic AGN Jets I. The Delicate Interplay between Jet Structure, Cocoon Morphology and Jet-Head Propagation. *Monthly Notices of the Royal Astronomical Society*, **433**, 1453-1478. https://doi.org/10.1093/mnras/stt823

[28] Gabuzda, D., Nagle, M. and Roche, N. (2018) The Jets of AGN as Giant Coaxial Cables. *Astronomy & Astrophysics*, **612**, Article No. A67. https://doi.org/10.1051/0004-6361/201732136

[29] Gabuzda, D. (2019) Evidence for Helical Magnetic Fields Associated with AGN Jets and the Action of a Cosmic Battery. G*alaxies*, **7**, 14 p. https://doi.org/10.3390/galaxies7010005

[30] Fossati, G., *et al.* (1998) A Unifying View of the Spectral Energy Distributions of Blazars. *Monthly Notices of the Royal Astronomical Society*, **299**, 433-448. https://doi.org/10.1046/j.1365-8711.1998.01828.x

International Journal of Astronomy and Astrophysics, 2019, 9, 154-171
http://www.scirp.org/journal/ijaa
ISSN Online: 2161-4725
ISSN Print: 2161-4717

Spectroscopic Survey of Hα Emission Line Stars Associated with Bright Rimmed Clouds

Kensuke Hosoya[1*], Yoichi Itoh[1], Yumiko Oasa[2], Ranjan Gupta[3], Asoke Kumar Sen[4]

[1]Nishi-Harima Astronomical Observatory, Center for Astronomy, University of Hyogo, Kobe, Japan
[2]Faculty of Education, Saitama University, Saitama, Japan
[3]Inter University Center for Astronomy and Astrophysics (IUCAA), Pune, India
[4]Department of Physics, Assam University, Silchar, India
Email: *yitoh@nhao.jp

How to cite this paper: Hosoya, K., Itoh, Y., Oasa, Y., Gupta, R. and Sen, A.K. (2019) Spectroscopic Survey of Hα Emission Line Stars Associated with Bright Rimmed Clouds. *International Journal of Astronomy and Astrophysics*, **9**, 154-171.
https://doi.org/10.4236/ijaa.2019.92012

Received: May 12, 2019
Accepted: June 18, 2019
Published: June 21, 2019

Abstract

The results of a spectroscopic survey of Hα emission line stars associated with fourteen bright rimmed clouds are presented. Slit-less optical spectroscopy was carried out with the Inter University Centre for Astronomy and Astrophysics (IUCAA) 2 m telescope and IUCAA Faint Object Spectrograph and Camera (IFOSC). Hα emission line was detected from 173 objects. Among them 85 objects have a strong Hα emission line with its equivalent width larger than 10 Å. Those are classical T Tauri stars. 52 objects have a weak Hα emission line with its equivalent width less than 10 Å and do not show intrinsic near-infrared excess. Those are weak-line T Tauri stars. On the other hand, 36 objects have a weak Hα emission line (<10 Å), although they show intrinsic near-infrared excess. Such objects are not common in low-mass star forming regions. Those are misfits of the general concept on formation process of a low-mass star, in which it evolves from a classical T Tauri star to a weak-line T Tauri star. Those might be weak-line T Tauri stars with a flared disk in which gas is heated by ultraviolet radiation from a nearby early-type star. Alternatively, we propose pre-transitional disk objects as their evolutional stage.

Keywords

Star Formation, Pre-Main Sequence Stars, T Tauri Stars

1. Introduction

A T Tauri star (TTS) is a low-mass star in the pre-main sequence stage. It was first identified as a variable star [1]. Successive studies on low-mass star forming regions, such as the Taurus molecular cloud, revealed two types of TTSs, namely

classical TTSs (CTTSs) and weak-line TTSs (WTTSs). CTTSs show the Hα emission line with its equivalent width larger than 10 Å. WTTSs also show the Hα emission line, but its equivalent width is less than 10 Å. [2] investigated near-infrared colors of TTSs in the Taurus molecular cloud. They estimated the amount of the interstellar extinction from $E(R-I)$ color and then calculated the dereddened colors of the TTSs. They noted that the WTTSs have the dereddened colors similar to those of normal main sequence stars. On the other hand, the dereddened colors of CTTSs occupy a narrow range in a $(J-H)-(H-K)$ color-color diagram. The range is well fitted by a linear line with an intersection with the reddening vector from an M6 dwarf at $A_V = 1.9$ mag (hereafter termed as the dereddened CTTS line). Dereddened colors of approximately half of the CTTSs are redder than that intersection point. Such CTTSs have an intrinsic near-infrared excess. Those are brighter in the *H*- and/or *K* band than the radiation expected only from the photosphere. The intrinsic near-infrared excess of a TTS is caused by an optically thick circumstellar disk, and the amount of the excess depends on the optical thickness of the disk, geometric structure of the disk, and viewing angle of the disk [3] [4]. Approximately half of CTTSs show the intrinsic near-infrared excess while the other CTTSs do not. On the other hand, WTTSs do not show the intrinsic near-infrared excess.

A low-mass star evolves from a protostar to a CTTS and subsequently a WTTS. [5] investigated the ages of TTSs in the Taurus molecular cloud. They used Hipparcos parallaxes as well as photometric and spectroscopic information for 72 TTSs. They plotted them on the HR diagram and then estimated their ages by comparing them to a pre-main sequence evolutionary track. It is revealed that the ages of the CTTSs are younger than those of the WTTSs. A solar mass star evolves from a CTTS to a WTTS at the age of 4×10^6 yr. [6] deduced the surface gravity of TTSs in the Taurus molecular cloud from high resolution spectroscopy and then estimated their ages by plotting them on the HR diagram. The fraction of the objects with the intrinsic near-infrared excess decreases with the age. They concluded that the dissipation timescale of the circumstellar disk is $3 - 4 \times 10^6$ yr. The general concept that a low-mass star evolves from a CTTS to a WTTS is well established by observational studies of nearby low-mass star forming regions.

Bright rimmed clouds (BRCs) are molecular clouds harboring an IRAS source and are located at periphery of an HII region. Ultra-violet radiation from OB stars ionizes molecular cloud materials through shock and excites hydrogen atoms at the surface of the cloud, making diffuse Hα emission. [7] and [8] presented comprehensive catalogs of BRCs, in which 89 BRCs are listed. Properties of the clouds and young stellar objects (YSOs) associated with the clouds have been extensively investigated. [9] carried out millimeter mapping observations of molecular clouds associated with the W5 HII region. They noticed that molecular clouds facing the HII region show a steep density gradient toward the HII region due to the compression of the HII region to the clouds. [10] conducted

Hα grism spectroscopy and optical narrow-band imaging observations of 28 BRCs. They detected 460 Hα emission line stars. [11] carried out wide-field near-infrared imaging observations of 32 BRCs. They identified 2099 objects as YSO candidates. These observational studies confirmed the formation of low-mass stars in BRCs. [12] carried out a near-infrared survey of 44 BRCs. They indicated that stars with bluer colors are located closer to the OB star and those with redder colors were closer to the IRAS source. [13] presented a near-infrared image of BRC 14. They revealed that the fraction of YSO candidates to all sources, the extinction of all sources, and the near-infrared excess of the YSO candidates increased from the outside of the rim to the center of the molecular cloud. These results indicated that star formation proceeds from outside to the center of the cloud.

We conducted slit-less optical spectroscopy of 14 BRCs to identify Hα emission line stars. We discuss evolution process of a low-mass star in a massive-star forming region based on the relationship between the Hα emission line and its intrinsic near-infrared excess.

2. Observations and Data Reduction

Spectroscopic survey of Hα emission line stars were carried out on six nights of 2011 January and 2012 January with IFOSC (IUCAA Faint Optical Spectrograph and Camera) mounted on the IUCAA 2-m telescope at Giravali near Pune, India. We used the IFOSC5 grism and the wide Hα filter, and we did not use any slits. IFOSC has a 2048 × 2048 CCD with the field of view of 10.5' × 10.5'. We had spectra centered at 6563 Å with a width of 80 Å and spectral resolution of ~ 9 Å. We also obtained V-band images. The targets were 14 BRCs listed in [7] and [8] that were observable on the observing date (**Table 1**). Three frames of 300-s exposure each were obtained for spectroscopy and one frame of 60 s was obtained for imaging. The OB star making the HII region and the bright rim is located in the observing fields of view for BRCs 15, 24, and 25. However, these OB stars are so bright that their spectra were saturated. The general seeing conditions varied between 0.9" and 2.0".

The object frames were calibrated with the Image Reduction and Analysis Facility (IRAF). Data were processed in standard manner, namely bias subtraction and flat fielding with the twilight frames. We detected point sources in the V-band image with SExtractor program. The limiting magnitude is approximately 19 mag. Based on the coordinate of the source, a spectrum image of each object was extracted from the spectral frame. The spectrum extends along a line. We average the counts of each line and the average count was then subtracted from each line of the image. In the process, the continuum flux of the object was subtracted and the emission line appeared as a point source. We detected the emission line via the SExtractor program. We also confirmed the emission line by eye inspection. For the image with the emission line, we extracted a 1-D spectrum from the image prior to the continuum subtraction. An equivalent width of

Table 1. Properties of the observed bright rimmed clouds.

Cloud	RA [J2000]	DEC [J2000]	HII region	Spectral type of the exciting star	Distance [pc]	obs. fields
BRC 15	05 23 30.1	+33 11 54	S 236	O5V, O6V	3600	6
BRC 16	05 19 48.9	−05 52 05	S 276	O7V, O8.5II, O9.5I	400	2
BRC 17	05 31 28.1	+12 06 24	S 264	O5V	450	3
BRC 18	05 44 29.8	+09 08 54	S 264	O5V	450	4
BRC 19	05 34 30.7	−02 38 12	S 277	O9.5V	400	1
BRC 21	05 39 41.3	−03 37 12	S 277	O9.5V	400	1
BRC 23	06 22 58.7	+23 09 58	S 249	O9V	1900	1
BRC 24	06 34 55.4	+04 25 14	S 275	O5V	1400	9
BRC 25	06 41 03.3	+10 21 59	S 273	O7V	913	3
BRC 26	07 03 47.2	−11 45 47	S 296	O7III	990	2
BRC 27	07 03 58.7	−11 23 19	S 296	B0V	990	2
BRC 28	07 04 43.4	−10 21 59	S 296	B0IV	990	2
BRC 29	07 04 52.4	−12 09 26	S 296	O7.5V	990	1
BRC 45	07 18 23.7	−22 06 13	RCW 14	O8V	1930	2

the emission line was measured with the IRAF splot task. We did not fit a Gaussian profile. The minimum equivalent width of the detected Hα emission line was 0.3 Å.

3. Results

Emission lines of Hα were identified from 173 objects (Table 2). Their equivalent widths range from 0.3 Å to 132 Å. We investigated near-infrared properties of the emission line stars by using 2MASS photometries. The near-infrared color-color diagram of the emission line stars are presented in Figure 1. We defined the line parallel to the reddening vector through an M6 dwarf color as the near-infrared excess border. Among the emission line stars, 77 objects are plotted redward of the border. We identified that such objects have the intrinsic near-infrared excess. The color-color diagram of TTSs in the BRCs is significantly different from that of TTSs in Taurus. TTSs with the equivalent width less than 10 Å in Taurus are plotted blueward of the near-infrared excess border (Meyer *et al.* 1997). On the other hand, such objects in the BRCs are plotted on either side of the near-infrared excess border, like CTTSs in the BRCs and also like CTTSs in Taurus.

In the Taurus molecular cloud, WTTSs are older than CTTSs. The ages of the TTSs in the BRCs were estimated on the $(I, I-J)$ color-magnitude diagram with the isochrone of [14]. *I*-magnitudes of the objects were taken from the USNO-B1.0 catalog. Because the extinction vector is relatively parallel to the isochrone on this diagram, it is possible to roughly estimate the age of the object.

Table 2. Hα emission line stars.

ID	RA [J2000] h m s	DEC [J2000] ° ' "	EW(Hα) Å	J mag	H mag	K mag	Identification
		BRC 15					
1	5 23 32.21	33 27 43.6	16.8	14.36	13.29	12.41	[PSM2011] 107
2	5 23 15.81	33 27 43.5	3.8	15.17	14.25	13.96	[PSM2011] 135, [CMP2012] 975
3	5 22 54.07	33 26 33.0	1.2	14.35	13.55	13.25	[PSM2011] 82, [CMP2012] 559
4	5 22 51.19	33 26 32.9	11.4	15.96	15.19	14.59	[MSB2007]37, [PSM2011] 851, [CMP2012] 465
5	5 22 53.82	33 25 41.5	13.9	15.93	14.89	14.12	[MSB2007]38, [PSM2011] 883, [CMP2012] 548
6	5 22 52.30	33 24 7.4	1.7	13.58	12.71	12.25	[PSM2011] 61, [CMP2012] 496
7	5 22 51.90	33 23 59.3	1.1	14.61	14.21	13.65	[PSM2011] 56
8	5 22 51.04	33 25 47.1	2.5	13.08	12.34	11.75	[MSB2007] 41, [PSM2011] 847, [CMP2012] 461
9	5 22 54.15	33 24 58.0	2.7	15.15	14.46	14.20	[PSM2011] 1168, [CMP2012] 563
10	5 22 45.78	33 28 16.2	60	15.05	14.04	13.54	[PSM2011] 177, [CMP2012] 294
11	5 22 18.44	33 28 21.2	6.3	11.13	11.04	10.98	NGC1893-256, [PSM2011] 1072, [CMP2012] 11
12	5 22 51.04	33 25 47.1	1.1	13.08	12.34	11.75	[MSB2007] 41, [PSM2011] 847, [CMP2012] 461
13	5 22 43.02	33 25 5.4	24.5	11.65	11.31	10.92	NGC1893-35, [MSB2007] 47, [PSM2011] 12
14	5 22 43.78	33 25 25.8	40.1	12.38	10.77	9.42	[MSB2007] 46, [PSM2011] 92, [CMP2012] 241
15	5 22 38.78	33 22 5.4	8.6	14.68	13.70	13.08	[PSM2011] 718, [CMP2012] 151
16	5 22 46.84	33 29 27.9	9.6	14.83	13.9	13.36	[MSB2007] 40, [PSM2011] 131, [CMP2012] 329
17	5 22 49.35	33 29 2.1	7.1	14.99	14.06	13.57	[PSM2011] 112, [CMP2012] 410
18	5 22 49.57	33 30 1.5	28.8	14.42	13.45	12.95	[PSM2011] 137, [CMP2012] 414
19	5 23 9.33	33 30 2.3	35.7	10.79	10.41	10.01	GGA 333, [PSM2011] 5
20	5 23 6.32	33 31 1.7	6.4	14.74	13.82	13.24	[PSM2011] 97, [CMP2012] 873
21	5 23 4.96	33 31 50.1	1.5	15.14	14.38	13.89	[PSM2011] 105, [CMP2012] 848
22	5 22 52.23	33 29 58.0	6.8	12.68	11.91	11.35	[MSB2007] 34, [PSM2011] 31, [CMP2012] 494
23	5 23 3.32	33 29 25.1	1.7	15.46	14.41	13.72	[MSB2007] 13, [PSM2011] 113, [CMP2012] 806
24	5 23 2.76	33 29 40.2	8.8	15.47	14.60	13.90	[MSB2007] 17, [PSM2011] 175, [CMP2012] 795
25	5 23 0.07	33 30 39.0	21.7	14.34	13.42	12.97	[PSM2011] 99, [CMP2012] 718
26	5 22 58.11	33 30 41.0	9.3	13.84	13.30	12.63	[MSB2007] 27, [PSM2011] 33
27	5 23 13.59	33 29 44.0	5.2	15.34	14.48	13.93	[PSM2011] 144, [CMP2012] 961
28	5 23 1.07	33 29 25.1	30	15.97	14.89	14.19	[MSB2007] 21, [PSM2011] 253, [CMP2012] 743
29	5 23 9.95	33 29 8.8	12.6	15.40	14.11	13.20	[MSB2007] 2, [PSM2011] 140, [CMP2012] 924
19	5 23 9.33	33 30 2.3	35.7	10.79	10.41	10.01	GGA 333, [PSM2011] 5
20	5 23 6.32	33 31 1.7	6.4	14.74	13.82	13.24	[PSM2011] 97, [CMP2012] 873
21	5 23 4.96	33 31 50.1	1.5	15.14	14.38	13.89	[PSM2011] 105, [CMP2012] 848
22	5 22 52.23	33 29 58.0	6.8	12.68	11.91	11.35	[MSB2007] 34, [PSM2011] 31, [CMP2012] 494
23	5 23 3.32	33 29 25.1	1.7	15.46	14.41	13.72	[MSB2007] 13, [PSM2011] 113, [CMP2012] 806

Continued

ID	RA [J2000] h m s	DEC [J2000] ° ' "	EW(Hα) Å	J mag mag	H mag mag	K mag mag	Identification
24	5 23 2.76	33 29 40.2	8.8	15.47	14.60	13.90	[MSB2007] 17, [PSM2011] 175, [CMP2012] 795
25	5 23 0.07	33 30 39.0	21.7	14.34	13.42	12.97	[PSM2011] 99, [CMP2012] 718
26	5 22 58.11	33 30 41.0	9.3	13.84	13.30	12.63	[MSB2007] 27, [PSM2011] 33
27	5 23 13.59	33 29 44.0	5.2	15.34	14.48	13.93	[PSM2011] 144, [CMP2012] 961
28	5 23 1.07	33 29 25.1	30	15.97	14.89	14.19	[MSB2007] 21, [PSM2011] 253, [CMP2012] 743
29	5 23 9.95	33 29 8.8	12.6	15.40	14.11	13.20	[MSB2007] 2, [PSM2011] 140, [CMP2012] 924
30	5 23 3.82	33 29 24.2	2	14.80	13.90	13.30	[MSB2007] 12, [PSM2011] 114, [CMP2012] 819
31	5 23 4.05	33 29 48.4	26.3	15.03	13.95	13.15	[MSB2007] 16, [PSM2011] 201, [CMP2012] 825
		BRC 17					
1	5 31 23.12	12 10 33.7	6.9	13.17	12.46	12.02	
2	5 31 26.94	12 10 20.5	2.7	11.96	11.25	10.89	
3	5 31 23.59	12 9 43.9	5.2	10.42	9.62	9.19	HI Ori, HBC 93, [DM99] 143
4	5 31 28.05	12 9 10.3	16.8	9.41	8.31	7.34	HK Ori, HBC 94
5	5 31 15.51	12 11 23.7	2.5	12.10	11.21	10.72	[DM99] 136
6	5 31 19.46	12 9 15.3	2.2	11.99	10.78	10.09	
7	5 30 51.70	12 8 36.7	26.5	11.64	10.87	10.45	V4480 Ori, HBC 91, [DM99]125
8	5 31 12.49	12 7 54.5	2	13.29	12.52	12.21	
9	5 31 21.91	11 54 56.7	2.2	13.60	12.96	12.69	
		BRC 18					
1	5 44 19.40	9 16 19.3	3.5	13.12	12.39	12.03	
2	5 44 22.89	9 10 35.3	2.5	12.45	11.72	11.45	[DM99] 247
3	5 44 23.21	9 12 3.9	1.4	10.00	9.36	8.95	[DM99] 248
4	5 44 37.32	9 11 59.1	3.8	12.95	12.33	12.05	
5	5 44 37.02	9 13 20.0	15.4	12.33	11.66	11.33	[DM99] 252
6	5 44 30.23	9 12 23.8	8.1	14.13	13.36	12.91	
7	5 44 17.35	9 10 59.2	17	10.79	10.04	9.62	V630 Ori, [DM99] 244
8	5 44 25.73	9 12 1.3	1.9	13.07	12.35	12.09	
9	5 44 10.04	9 8 40.8	43.2	13.85	13.12	12.64	
10	5 44 14.86	9 8 8.2	9.4	12.67	11.97	11.67	[DM99] 243
11	5 44 7.26	9 6 38.1	41.9	11.66	10.94	10.68	V629 Ori, [DM99] 240
12	5 44 28.66	9 6 18.6	8.8	14.43	13.81	13.46	
13	5 44 8.99	9 9 14.8	3.4	11.10	10.03	9.25	QR Ori, [DM99] 241
14	5 44 12.77	9 5 10.5	10.5	13.26	12.59	12.24	
15	5 43 56.59	9 18 16.9	26.8	12.85	12.04	11.67	[DM99] 238
16	5 43 31.22	9 17 46.3	10.8	12.88	12.30	11.97	

Continued

ID	RA [J2000] h m s	DEC [J2000] ° ' "	EW(Hα) Å	J mag mag	H mag mag	K mag mag	Identification
17	5 43 57.00	9 16 24.0	38.8	12.34	11.57	11.17	
18	5 43 50.67	9 12 25.0	10.3	13.33	12.37	11.82	
19	5 43 39.59	9 10 40.8	4.9	13.34	12.66	12.35	
20	5 43 51.36	9 13 40.6	66.9	14.62	13.98	13.74	
21	5 43 32.20	9 9 24.0	7.2	11.29	10.55	10.19	V626 Ori, [DM99]231
22	5 43 44.50	9 8 1.2	20.8	14.57	12.62	11.09	
23	5 43 53.50	9 7 11.8	42	13.09	12.23	11.71	
24	5 43 20.92	9 6 7.1	5	10.07	9.13	8.41	V625 Ori, [DM99]227
25	5 43 52.20	9 6 51.4	1.8	14.45	13.82	13.56	
		BRC 19					
1	5 34 34.24	−2 58 16.6	55	12.77	11.67	11.03	Haro 5-83
2	5 34 20.38	−2 57 46.9	3.1	13.75	12.27	11.27	V1945 Ori
		BRC 24					
1	6 34 25.74	4 28 15.8	20.6	14.57	13.55	12.76	[WFT2009] RMCX 324
2	6 34 41.04	4 27 9.9	15.9	14.82	13.50	12.68	
3	6 33 50.40	4 32 55.9	3.5	13.11	12.42	11.98	
4	6 34 2.21	4 30 7.6	9.9	14.43	13.49	13.00	[WFT2009] RMCX 189
5	6 34 17.07	4 27 35.3	22.5	14.72	13.53	12.69	
6	6 34 4.22	4 34 34.1	9.9	14.45	13.44	12.86	[WFT2009] RMCX 199
7	6 34 3.41	4 34 8.8	22	13.24	12.36	11.72	[WFT2009] RMCX 195
8	6 33 58.01	4 33 31.3	20.2	14.75	13.71	12.97	[WFT2009] RMCX 179
9	6 33 55.73	4 28 23.4	14.4	15.48	14.41	13.85	
10	6 33 54.60	4 29 41.6	6	15.35	13.87	12.88	
11	6 34 8.90	4 29 38.5	13.7	15.15	14.13	13.64	[WFT2009] RMCX 233
12	6 33 45.75	4 31 3.5	25.4	15.24	14.08	13.56	
13	6 33 56.09	4 31 19.3	32.1	14.65	13.65	13.11	[WFT2009] RMCX 172
14	6 34 2.85	4 34 51.0	2.4	13.55	12.68	12.20	[WFT2009] RMCX 190
15	6 33 41.16	4 37 5.1	3.8	14.01	12.94	12.17	[WFT2009] RMCX 149
16	6 32 35.75	4 46 30.4	23	14.01	13.10	12.56	[BNM2013] 66.01 15
4	6 34 2.21	4 30 7.6	9.9	14.43	13.49	13.00	[WFT2009] RMCX 189
5	6 34 17.07	4 27 35.3	22.5	14.72	13.53	12.69	
6	6 34 4.22	4 34 34.1	9.9	14.45	13.44	12.86	[WFT2009] RMCX 199
7	6 34 3.41	4 34 8.8	22	13.24	12.36	11.72	[WFT2009] RMCX 195
8	6 33 58.01	4 33 31.3	20.2	14.75	13.71	12.97	[WFT2009] RMCX 179
9	6 33 55.73	4 28 23.4	14.4	15.48	14.41	13.85	

Continued

ID	RA [J2000] h m s	DEC [J2000] ° ' "	EW(Hα) Å	J mag mag	H mag mag	K mag mag	Identification
10	6 33 54.60	4 29 41.6	6	15.35	13.87	12.88	
11	6 34 8.90	4 29 38.5	13.7	15.15	14.13	13.64	[WFT2009] RMCX 233
12	6 33 45.75	4 31 3.5	25.4	15.24	14.08	13.56	
13	6 33 56.09	4 31 19.3	32.1	14.65	13.65	13.11	[WFT2009] RMCX 172
14	6 34 2.85	4 34 51.0	2.4	13.55	12.68	12.20	[WFT2009] RMCX 190
15	6 33 41.16	4 37 5.1	3.8	14.01	12.94	12.17	[WFT2009] RMCX 149
16	6 32 35.75	4 46 30.4	23	14.01	13.10	12.56	[BNM2013] 66.01 15
17	6 32 34.95	4 44 39.2	32.8	10.11	9.90	9.53	NGC2244 279
18	6 32 45.11	4 45 23.1	15.5	13.33	12.29	11.57	[WTF2008] Main 878
19	6 32 31.01	4 50 6.0	1.5	12.07	11.57	11.09	NGC2244 269
20	6 32 31.44	4 42 34.0	0.5	11.74	11.03	10.83	[WTF2008] Main 831
21	6 32 50.74	4 44 47.6	1.3	12.94	12.09	11.70	[WTF2008] Main 898
22	6 32 1.83	4 53 38.6	6.5	14.26	13.32	12.91	[WTF2008] Main 498
23	6 32 7.82	4 52 28.4	18.3	14.03	13.21	12.76	[WTF2008] Main 590
24	6 32 4.66	4 54 51.5	2.8	13.80	12.92	12.54	[WTF2008] Main 541
25	6 32 4.53	4 53 25.0	2.7	13.59	12.71	12.23	[WTF2008] Main 536
26	6 31 41.02	4 54 47.9	8.3	14.18	13.36	12.95	[WTF2008] Main 133
27	6 31 43.85	5 2 57.5	4	13.27	12.38	11.97	[WTF2008] Main 169
28	6 31 49.26	4 57 0.9	5.4	13.7	12.85	12.27	[WTF2008] Main 254
29	6 31 51.65	4 55 5.2	6.7	13.91	13.01	12.45	V547 Mon
30	6 31 29.76	4 54 49.1	8.8	11.45	10.89	9.69	GGA 395, NGC2244 74
31	6 31 39.62	4 59 45.1	23.5	14.12	13.13	12.65	[WTF2008] Main 124
32	6 31 39.88	4 56 39.1	17.8	15.05	14.10	13.62	
33	6 31 20.87	5 4 8.5	3.8	14.07	13.23	12.71	[BNM2013] 66.03 296
34	6 31 48.31	4 58 20.3	5.8	12.43	11.57	11.08	[WTF2008] Main 243
35	6 31 29.52	4 54 34.2	8.1	14.92	14.11	13.72	[WTF2008] Main 43
36	6 30 42.71	4 55 31.4	1.7	11.23	10.47	9.75	V539 Mon
37	6 31 0.55	4 58 7.3	8.4	14.64	13.76	13.18	[WFT2010] 126
38	6 31 30.96	5 6 58.5	28.6	12.88	12.08	11.60	
39	6 31 40.00	5 5 56.4	6.3	9.68	8.96	8.27	NGC2244 106
40	6 31 2.88	5 3 49.3	8.9	13.74	12.84	12.38	[WFT2010] 134
41	6 31 12.63	5 5 2.6	3.6	14.42	13.30	12.62	
		BRC 25					
1	6 41 1.53	10 14 56.1	20.7	12.93	12.18	11.66	LkHα 46
2	6 41 7.48	10 15 4.5	3.3	13.24	12.47	12.15	ESO-Hα 493

Continued

3	6	41	9.85	10	15	2.6	11.1	13.19	11.80	10.85	ESO-Hα 504
4	6	41	7.01	10	16	28.9	1.3	12.99	12.32	12.06	
5	6	40	59.79	10	2	12.6	15.5	14.66	13.82	13.50	ESO-Hα 454
6	6	41	2.86	10	7	11.9	4.5	13.98	13.22	12.87	ESO-Hα 468
7	6	41	7.26	9	58	31.2	0.3	12.54	11.87	11.68	V609 Mon
8	6	40	49.21	9	57	38.8	12.4	13.57	12.74	12.37	ESO-Hα 415
9	6	41	17.25	9	54	32.4	25.6	12.83	12.05	11.55	IQ Mon
10	6	40	49.75	9	52	58.6	2.7	14.20	13.56	13.33	V343 Mon
11	6	40	50.59	9	54	57.3	6.1	12.47	11.69	11.28	LkHα 31
12	6	40	52.55	9	52	6.0	2	12.69	11.97	11.72	ESO-Hα 425
13	6	41	12.58	9	52	31.2	9.6	11.49	10.69	10.21	MM Mon
14	6	40	59.45	9	59	45.5	4.9	12.78	12.09	11.69	V602 Mon
15	6	40	54.88	9	53	12.4	5.5	13.92	13.09	12.40	ESO-Hα 435
16	6	40	46.95	9	52	40.6	42	14.75	14.06	13.41	ESO-Hα 405
17	6	40	54.11	9	52	24.6	28.9	15.34	14.88	14.33	ESO-Hα 432
18	6	40	54.20	9	55	52.0	32	13.70	12.94	12.76	NGC2264 SBL 219
							BRC 26				
1	7	3	40.75	−11	46	16.6	22.7	15.24	14.06	13.21	
2	7	3	48.22	−11	41	46.0	5.2	13.61	12.84	12.55	
3	7	4	7.18	−11	40	32.7	3.9	14.08	13.87	13.73	
4	7	3	49.91	−11	31	17.0	8.2	14.03	13.20	12.95	
5	7	3	54.00	−11	32	47.9	5.2	12.34	11.61	11.18	
6	7	3	54.03	−11	32	37.2	63.1	14.57	13.7	13.29	
7	7	3	58.35	−11	33	34.6	19.1	14.92	13.93	13.52	
8	7	4	1.33	−11	36	17.5	26.3	14.77	13.93	13.42	
9	7	4	0.68	−11	37	49.3	12.8	13.98	13.23	12.93	
10	7	3	38.52	−11	31	51.9	22.8	14.22	13.28	12.75	
11	7	3	43.68	−11	36	56.6	33.3	14.89	13.92	13.66	
12	7	4	4.70	−11	31	15.9	24.5	15.57	14.66	14.38	
13	7	3	58.06	−11	32	39.9	3.4	14.10	13.23	12.93	
14	7	3	50.34	−11	32	51.4	16.3	15.81	14.92	14.30	[CPD2009] J070350.34-113251.4
15	7	4	0.41	−11	33	59.6	2.4	12.10	10.92	10.19	[CPD2009] J070400.41-113359.5
16	7	3	56.71	−11	35	9.6	23.3	14.34	12.95	12.11	[CPD2009] J070356.71-113509.6
17	7	4	3.94	−11	35	57.1	11.6	14.51	13.63	13.21	
18	7	4	5.53	−11	39	52.4	28.2	15.62	14.72	14.20	
19	7	3	48.98	−11	37	19.4	20	15.42	14.58	14.24	

Continued

ID	RA [J2000] h m s	DEC [J2000] ° ' "	EW(Hα) Å	J mag mag	H mag mag	K mag mag	Identification
		BRC 27					
1	7 4 8.04	−11 23 54.7	16.9	13.12	12.44	12.20	[OSP2002] BRC 27 22
2	7 4 6.70	−11 26 8.5	17	10.76	10.02	9.12	LkHα 220
3	7 4 9.96	−11 23 16.4	18	11.79	10.71	9.83	[OSP2002] BRC 27 25
4	7 3 53.04	−11 29 35.3	10.9	12.36	11.54	10.95	LkHα 219
5	7 3 54.03	−11 32 37.2	88.3	14.57	13.7	13.29	
6	7 3 49.9	−11 31 17.0	10.1	14.03	13.20	12.95	
7	7 3 45.76	−11 23 14.9	5.8	13.59	12.59	12.19	
8	7 4 4.27	−11 23 55.7	100	15.01	14.02	13.54	[OSP2002] BRC 27 12
9	7 4 5.93	−11 23 58.7	6.1	14.42	13.47	12.93	[OSP2002] BRC 27 16
10	7 4 12.93	−11 24 3.2	5.9	15.37	14.39	13.91	[OSP2002] BRC 27 28
11	7 3 47.58	−11 22 33.9	3.5	13.93	13.15	12.85	
12	7 3 57.05	−11 30 16.9	131.8	15.30	14.63	14.30	
13	7 4 22.75	−11 27 50.9	12.8	14.24	13.36	12.95	
14	7 4 20.87	−11 29 36.2	18.6	13.80	12.88	12.29	[CPD2009] J070420.87-112936.2
15	7 4 17.79	−11 28 21.2	23	14.50	13.75	13.3	
16	7 4 45.00	−11 27 58.9	28	14.86	14.16	13.80	
17	7 4 23.25	−11 24 17.3	5.8	13.45	12.64	12.19	
18	7 4 16.80	−11 24 32.4	46.2	14.12	13.21	12.60	[CPD2009] 112
19	7 4 40.79	−11 25 37.0	7	14.38	13.57	13.26	
20	7 4 13.53	−11 24 55.8	15.3	12.19	11.29	10.78	[OSP2002] BRC 27 29
21	7 4 26.26	−11 31 20.7	17.8	12.47	11.60	11.15	LkHα 222
		BRC 45					
1	7 18 36.26	−22 7 14.6	9.7	15.71	14.87	14.67	
2	7 18 22.93	−22 4 14.5	10.5	13.3	12.45	11.84	
3	7 18 28.46	−22 5 15	31.5	15.07	14.03	13.36	
4	7 18 39.85	−22 0 42.2	10.3	15.50	14.73	14.51	
5	7 19 2.80	−22 1 4.6	38.6	13.80	12.97	12.24	
6	7 18 56.73	−22 1 5.3	12.8	14.89	14.09	13.55	
7	7 18 57.67	−22 1 36.4	31.1	14.66	13.47	12.83	

[CDP2009]: [17]; [CMP2012]: [18]; [DM99]: [19]; [BNM2013]: [20]; [MSB2007]: [21]; [OSP2002]: [10]; [PSM2011]: [22]; [WFT2009]: [23]; [WTF2008]: [24].

It is indicated that majority of the objects have the age between 1 Myr and 10 Myr. We did not find any differences in the ages between the objects with a strong Hα emission line and the objects with a weak Hα emission line.

Masses of the TTSs were estimated with the isochrones of [14] [15] and [16]

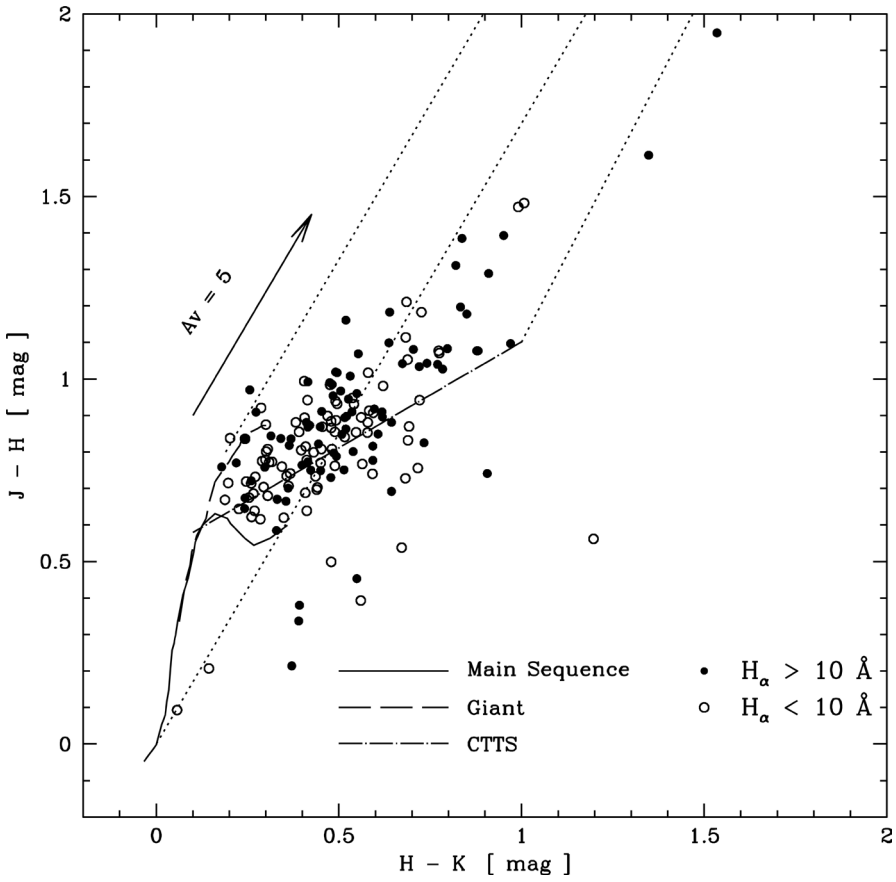

Figure 1. Near-infrared color-color diagram of the Hα emission line stars in the BRCs. A certain portion of stars with a weak Hα emission line show intrinsic near-infrared excess.

on the $(J, J-H)$ color-magnitude diagram. It is revealed that most of the objects have mass between 0.5 $M_\odot$ and 2 $M_\odot$.

4. Discussion

We identified Hα emission line stars in the BRCs. Some objects show intrinsic near-infrared excess and the others do not. We investigated the relationship between the intrinsic near-infrared excess and the Hα equivalent widths (**Figure 2**). The intersection of the reddening vector originating from the observed *JHK* colors of the TTSs and the dereddened CTTS line represents the amount of the intrinsic near-infrared excess of the TTS. Zero point of the intrinsic near-infrared excess is defined as the intersection of the near-infrared excess border and the dereddened CTTS line. We also defined the point of unity of the intrinsic near-infrared excess as the reddest intrinsic color of CTTSs (Meyer *et al.* 1997). The object with the intrinsic near-infrared excess > 0 has an intrinsic near-infrared excess. CTTSs and WTTSs are classified by the Hα equivalent width. We classified the objects into four types. Type 1 object has the Hα emission line with its equivalent width less than 10 Å and does not show the intrinsic near-infrared excess. Type 2 object has the Hα emission line with its equivalent width less than 10 Å and shows the intrinsic near-infrared excess. Type 3 object has the Hα

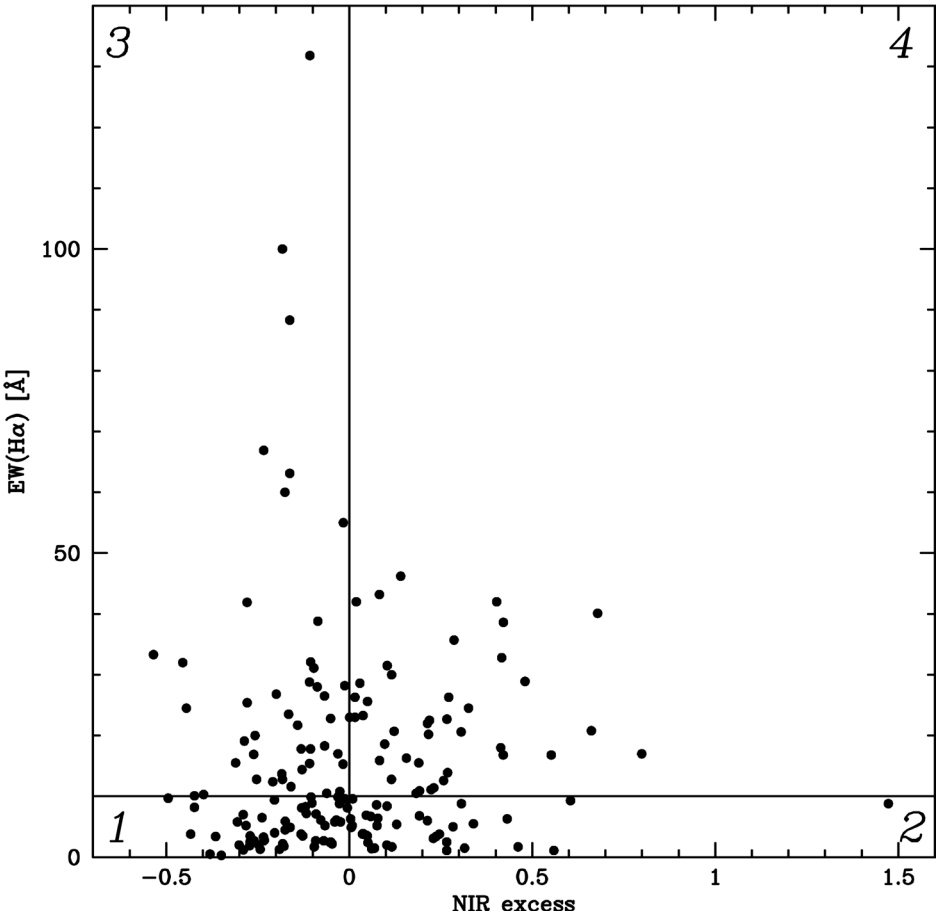

Figure 2. The intrinsic near-infrared excess and the equivalent widths of the Hα emission line of the TTSs associated with the BRCs. Type 3 objects and Type 4 objects are identified as CTTSs and Type 1 objects as WTTSs. Type 2 objects are newly identified with this study.

emission line with its equivalent width larger than 10 Å and does not show the intrinsic near-infrared excess. Type 4 object has the Hα emission line with its equivalent width larger than 10 Å and shows the intrinsic near-infrared excess. For the Hα emission line stars in the observed BRCs, 30% stars are classified into Type 1, 21% into Type 2, 25% into Type 3, and 24% into Type 4. We do not find mass nor extinction dependencies on the object types.

Hα emission line stars in other star forming regions were also investigated. We used the Hα equivalent widths listed in [25] for the objects in the Taurus molecular cloud, [26] for the Chamaeleon molecular cloud, [27] for the ρ Ophiuchi cloud, [28] and [29] for BRCs, and [30] for the Orion cluster. Near-infrared magnitudes of the Hα emission line stars were taken from 2MASS catalog. **Table 3** shows the classification of the Hα emission line stars in the regions. It is revealed that Type 2 objects are abundant in the massive star forming regions such as BRCs compared to those in the low-mass star forming regions such as the Taurus molecular cloud. On the other hand, difference in the spatial distributions of Type 2 objects and the other type objects is not identified for the BRCs observed in this study and IC 1396 cluster.

Table 3. Classification of the Hα emission line stars.

Region	Type 1	Type 2	Type 3	Type 4
BRC (this study)	52 (30%)	36 (21%)	44 (25%)	41 (24%)
BRC (Ikeda *et al.*)	177 (36%)	108 (22%)	98 (20%)	108 (22%)
IC 1396 (Nakano *et al.*)	236 (37%)	45 (7%)	249 (39%)	109 (17%)
Orion	167 (31%)	16 (3%)	221 (41%)	135 (25%)
Taurus	53 (42%)	5 (4%)	25 (20%)	42 (34%)
Chamaeleon	44 (63%)	3 (4%)	14 (18%)	12 (15%)
ρ Oph	185 (81%)	7 (3%)	21 (9%)	16 (7%)

The general concept that a low-mass star evolves from a CTTS to a WTTS is well established by many observational studies of nearby low-mass star forming regions. In our definition, Type 3 and Type 4 objects correspond to CTTSs and Type 1 objects to WTTSs. Dissipation process of a circumstellar disk around a low-mass star in strong UV field emanating from a nearby OB star has been widely discussed. [31] observed the Arches cluster near the Galactic center. They identified a significant population of near-infrared excess sources. The disk fraction of B-type star was derived as 6% in the Arches cluster. On the other hand, the fraction was as low as 3% in the vicinity of O-type stars in the cluster core. They concluded that disk dissipation process was more rapid in compact starburst clusters than in moderate star-forming environments.

Disk dissipation process due to UV radiation is also examined by numerical simulations. [32] considered circumstellar disk evolution in strong far-UV radiation fields from external stars. It is revealed that the UV radiation from nearby OB stars heats the gas near the disk edge and effectively drives mass loss from circumstellar disks. They also found that the UV radiation photoevaporates disks and disk radii are truncated to less than ~100 AU.

Type 2 objects have a weak Hα emission line but show the intrinsic near-infrared excess. Those are classified into WTTSs from optical spectroscopy, albeit into CTTSs from near-infrared photometry. The general concept of the formation process of a low-mass star does not involve such objects. We propose two hypotheses for Type 2 objects. The first hypothesis involves the idea that a Type 2 object is a WTTS with a flaring circumstellar disk. The Hα emission line stars are associated with the BRCs. Photons from the nearby OB star ionize hydrogen atoms outside the BRCs and excite hydrogen atoms at the boundary of the BRCs. Type 2 objects may be irradiated by UV photons from the nearby OB star. [33] calculated the structure of a circumstellar disk irradiated by UV radiation emanating from a nearby massive star, based on the circumstellar disk model of [34] and [35]. They indicated that the disk has large scale height, because gas in the disk is heated by the UV radiation then expands. We constructed SEDs of the Hα emission line stars in IC 1396 cluster with the photometric data of Guide Star Catalog, 2MASS catalog, and WISE catalog, then fitted them with the SED

model of [36]. Surface height of the circumstellar disk is expressed as,

$$H(r) = H_0 \left(\frac{r}{R_0} \right)^{\beta}, \quad (1)$$

where H_0 is the disk half-thickness, R_0 is the radius of the central star, and β is the flaring parameter [37]. β is deduced to be between 1.00 and 1.20 for all objects. The average β are 1.067 ± 0.008, 1.095 ± 0.015, and 1.106 ± 0.009 for Type 1, 3, and 4 objects, respectively, while that of Type 2 objects is as high as 1.125 ± 0.011. Large β of Type 2 objects supports the idea that those are WTTSs with a highly flared disk, although the difference in β between Type 2 and Type 4 is less than 2σ significance level. Spatial distribution of Type 2 objects should be inhomogeneous, if this hypothesis is valid. One may guess rich population of Type 2 objects outside the BRC or at the surface of the BRC. However, we do not find such spatial distribution of Type 2 objects.

Another hypothesis is that Type 2 objects are pre-transitional disk objects. A transitional disk object has a circumstellar disk with an inner hole created by photo evaporation of a central star or planet formation. A pre-transitional disk object has a small and optically thick disk in the inner hole of the circumstellar disk. If near-infrared excess arises from the inner disk and a small amount of material accretes from the inner disk to the photosphere, then the object is classified into Type 2 object. We investigated Hα strength and near-infrared excess of five pre-transitional disk objects listed in [38]. Four objects are located in the Type 2 region, or in Type 4 region near the border between Type 2 region and Type 4 region in the near-infrared excess and Hα equivalent width diagram. Similarities between Type 2 objects and pre-transitional disk objects is also found in the near-infrared and WISE colors. We plotted the TTSs in the BRCs, the transitional disk objects in the L 1641 cloud [39], and the known pre-transitional disk objects on the near-infrared and WISE color diagram (**Figure 3**). Majority of Type 2 objects are not plotted in the transitional disk object region, but their K- [4.6] colors are redder than that of the transitional disk objects. The known pre-transitional disk objects and Type 2 objects in the BRCs are plotted on the similar region in the diagram.

[40] carried out near-infrared polarimetry of BRC 74. They found that the magnetic field in the layer just behind the rim ran along the rim. The estimated magnetic field strength was ~90 μG, stronger than that far inside, ~30 μG, thereby suggesting that the magnetic field inside the rim is enhanced by the UV-radiation-induced shock. A proto-planetary disk has an inner stable region and an outer unstable region, if it magnetizes. [41] indicated that the boundary between stable and unstable regions is located at ~ 20 AU from the central star and the stable region shrinks in strong magnetic field environment. An abundant population of Type 2 objects in the BRCs may indicate slow evolution from CTTSs to WTTSs. Geometric structure and evolution timescale of a proto-planetary disk in the close vicinity of the central star under a strong magnetic field is to be investigated.

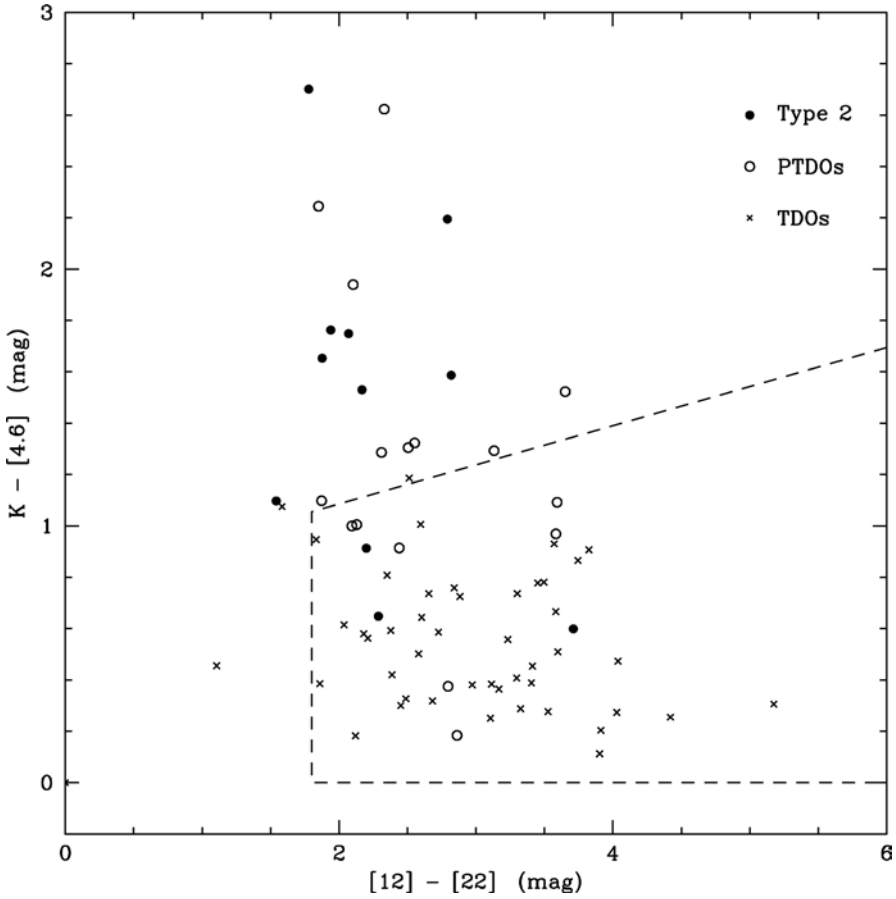

Figure 3. The near-infrared *K*-band and WISE 4.6 μm-, 12 μm-, and 22 μm-bands color diagram of Type 2 objects, transitional disk objects, and pre-transitional disk objects. The region enclosed by a dashed line is the region of the transitional disk objects. Type 2 objects and pre-transitional disk objects have redder color in *K*-[4.6] color.

5. Conclusion

We have conducted slit-less optical spectroscopy for 14 bright rimmed clouds and found 173 Hα emission line stars. Among them, 36 objects have a weak Hα emission line, but show intrinsic near-infrared excess. Those are identified as WTTSs with optical spectroscopy, but as CTTSs with near-infrared photometry. The general concept of the formation process of a low-mass star does not involve such objects. Those might be weak-line T Tauri stars with a flared circumstellar disk in which gas is heated by ultraviolet radiation from a nearby early-type star. Alternatively, those might be pre-transitional disk objects.

Acknowledgements

We thank the telescope staff members and operators at the IUCAA 2 m Telescope. This study was partly supported by the JSPS-DST collaboration.

Conflicts of Interest

The authors declare no conflicts of interest regarding the publication of this paper.

References

[1] Joy, A.H. (1945) T Tauri Variable Stars. *The Astrophysical Journal*, **102**, 168-195. https://doi.org/10.1086/144749

[2] Meyer, M.R., Calvet, N. and Hillenbrand, L.A. (1997) Intrinsic Near-Infrared Excesses of T Tauri Stars: Understanding the Classical T Tauri Star Locus. *The Astrophysical Journal*, **114**, 288-300. https://doi.org/10.1086/118474

[3] Bertout, C., Basri, G. and Bouvier, J. (1988) Accretion Disks around T Tauri Stars. *The Astrophysical Journal*, **330**, 350-373. https://doi.org/10.1086/166476

[4] Lada, C.J. and Adams, F.C. (1992) Interpreting Infrared Color-Color Diagrams—Circumstellar Disks around Low- and Intermediate-Mass Young Stellar Objects. *The Astrophysical Journal*, **393**, 278-288. https://doi.org/10.1086/171505

[5] Bertout, C., Siess, L. and Cabrit, S. (2007) The Evolution of Stars in the Taurus-Auriga T Association. *Astronomy & Astrophysics*, **473**, L21-L24. https://doi.org/10.1051/0004-6361:20078276

[6] Takagi, Y., Itoh, Y. and Oasa, Y. (2014) Disk Dissipation Timescale of Pre-Main Sequence Stars in Taurus. *Publications of the Astronomical Society of Japan*, **66**, 88. https://doi.org/10.1093/pasj/psu062

[7] Sugitani, K., Fukui, Y. and Ogura, K. (1991) A Catalog of Bright-Rimmed Clouds with IRAS Point Sources: Candidates for Star Formation by Radiation-Driven Implosion. I. The Northern Hemisphere. *The Astrophysical Journal Supplement Series*, **77**, 59-66. https://doi.org/10.1086/191597

[8] Sugitani, K. and Ogura, K. (1994) A Catalog of Bright-Rimmed Clouds with IRAS Point Sources: Candidates for Star Formation by Radiation-Driven Implosion. 2: The Southern Hemisphere. *The Astrophysical Journal Supplement Series*, **92**, 163-172. https://doi.org/10.1086/191964

[9] Niwa, T., *et al.* (2009) Millimeter-Wave Survey of Molecular Clouds around the W5-East Triggered Star-Forming Region. *Astronomy & Astrophysics*, **500**, 1119-1129. https://doi.org/10.1051/0004-6361/200811065

[10] Ogura, K., *et al.* (2002) Hα Emission Stars and Herbig-Haro Objects in the Vicinity of Bright-Rimmed Clouds. *The Astronomical Journal*, **123**, 2597-2626. https://doi.org/10.1086/339976

[11] Hayashi, M., Itoh, Y. and Oasa, Y. (2012) Near-Infrared Survey of Bright Rimmed Clouds. *Publications of the Astronomical Society of Japan*, **64**, 96. https://doi.org/10.1093/pasj/64.5.96

[12] Sugitani, K., Tamura, M. and Ogura, K. (1995) Young Star Clusters in Bright-Rimmed Clouds: Small-Scale Sequential Star Formation? *The Astrophysical Journal*, **455**, L39-L41. https://doi.org/10.1086/309808

[13] Matsuyanagi, I., *et al.* (2006) Sequential Formation of Low-Mass Stars in the BRC 14 Region. *Publications of the Astronomical Society of Japan*, **58**, L29-L34. https://doi.org/10.1093/pasj/58.4.L29

[14] Siess, L., Dufour, E. and Forestini, M. (2000) An Internet Server for Pre-Main Sequence Tracks of Low- and Intermediate-Mass Stars. *Astronomy & Astrophysics*, **358**, 593-599.

[15] Baraffe, I., *et al.* (1998) Evolutionary Models for Solar Metallicity Low-Mass Stars: Mass-Magnitude Relationships and Color-Magnitude Diagrams. *Astronomy & Astrophysics*, **337**, 403-412.

[16] Baraffe, I., *et al.* (2003) Evolutionary Models for Cool Brown Dwarfs and Extrasolar Giant Planets. The Case of HD 209458. *Astronomy & Astrophysics*, **402**, 701-712.

https://doi.org/10.1051/0004-6361:20030252

[17] Chauhan, N., *et al.* (2009) Triggered Star Formation and Evolution of T-Tauri Stars in and around Bright-Rimmed Cloud. *Monthly Notices of the Royal Astronomical Society*, **396**, 964-983. https://doi.org/10.1111/j.1365-2966.2009.14756.x

[18] Caramazza, M., *et al.* (2012) Star Formation in the Outer Galaxy: Coronal Properties of NGC 1893. *Astronomy & Astrophysics*, **539**, A74. https://doi.org/10.1051/0004-6361/201117256

[19] Dolan, C.J. and Mathieu, R.D. (1999) A WIYN Lithium Survey for Young Stars in the λ Orionis Star-Forming Region. *The Astronomical Journal*, **118**, 2409-2423. https://doi.org/10.1086/301075

[20] Bell, C.P.M., *et al.* (2013) Pre-Main Sequence Isochrones II. Revising Star and Planet Formation Time-Scales. *Monthly Notices of the Royal Astronomical Society*, **434**, 806-831. https://doi.org/10.1093/mnras/stt1075

[21] Maheswar, G., *et al.* (2007) Champagne Flow and Triggered Star Formation in NGC 1893. *Monthly Notices of the Royal Astronomical Society*, **379**, 1237-1247. https://doi.org/10.1111/j.1365-2966.2007.12020.x

[22] Prisinzano, L., *et al.* (2011) Star Formation in the Outer Galaxy: Membership and Fundamental Parameters of the Young Open Cluster NGC 1893. *Astronomy & Astrophysics*, **527**, A77. https://doi.org/10.1051/0004-6361/201015482

[23] Wang, J., *et al.* (2009) A Chandra Study of the Rosette Star-Forming Complex. II. Clusters in the Rosette Molecular Cloud. *The Astrophysical Journal*, **696**, 47-65. https://doi.org/10.1088/0004-637X/696/1/47

[24] Wang, J., *et al.* (2008) A Chandra Study of the Rosette Star-Forming Complex. I. The Stellar Population and Structure of the Young Open Cluster NGC 2244. *The Astrophysical Journal*, **675**, 464-490. https://doi.org/10.1086/526406

[25] Kenyon, S.J. and Hartmann, L. (1995) Pre-Main-Sequence Evolution in the Taurus-Auriga Molecular Cloud. *The Astrophysical Journal Supplement Series*, **101**, 117-171. https://doi.org/10.1086/192235

[26] Frasca, A., *et al.* (2015) The Gaia-ESO Survey: Chromospheric Emission, Accretion Properties, and Rotation in γ Velorum and Chamaeleon I. *Astronomy & Astrophysics*, **575**, A4. https://doi.org/10.1051/0004-6361/201424409

[27] Erickson, K.L., *et al.* (2011) The Initial Mass Function and Disk Frequency of the Rho Ophiuchi Cloud: An Extinction-Limited Sample. *The Astrophysical Journal*, **142**, A140. https://doi.org/10.1088/0004-6256/142/4/140

[28] Ikeda, H., *et al.* (2008) Sequential Star Formation in a Cometary Globule (BRC37) of IC1396. *The Astrophysical Journal*, **135**, 2323-2335. https://doi.org/10.1088/0004-6256/135/6/2323

[29] Nakano, M., *et al.* (2012) Wide-Field Survey of Emission-Line Stars in IC 1396. *The Astrophysical Journal*, **143**, A61. https://doi.org/10.1088/0004-6256/143/3/61

[30] Szegedi-Elek, E., *et al.* (2013) A New Halpha Emission-Line Survey in the Orion Nebula Cluster. *The Astrophysical Journal Supplement Series*, **208**, A28. https://doi.org/10.1088/0067-0049/208/2/28

[31] Stolte, A., *et al.* (2010) Disks in the Arches Cluster—Survival in a Starburst Environment. *The Astrophysical Journal*, **718**, 810-831. https://doi.org/10.1088/0004-637X/718/2/810

[32] Anderson, K.R., Adams, F.C. and Calvet, N. (2013) Viscous Evolution and Photoevaporation of Circumstellar Disks Due to External Far Ultraviolet Radiation Fields. *The Astrophysical Journal*, **774**, A9. https://doi.org/10.1088/0004-637X/774/1/9

[33] Walsh, C., *et al.* (2014) Complex Organic Molecules in Protoplanetary Disks. *Astronomy & Astrophysics*, **563**, A33. https://doi.org/10.1051/0004-6361/201322446

[34] Nomura, H. and Millar, T.J. (2005) Molecular Hydrogen Emission from Protoplanetary Disks. *Astronomy & Astrophysics*, **438**, 923-938. https://doi.org/10.1051/0004-6361:20052809

[35] Nomura, H. and Nakagawa, Y. (2006) Dust Size Growth and Settling in a Protoplanetary Disk. *The Astrophysical Journal*, **640**, 1099-1109. https://doi.org/10.1086/500251

[36] Robitaille, T.P., *et al.* (2006) Interpreting Spectral Energy Distributions from Young Stellar Objects. I. A Grid of 200,000 YSO Model SEDs. *The Astrophysical Journal Supplement Series*, **167**, 256-285. https://doi.org/10.1086/508424

[37] Kenyon, S.J. and Hartmann, L. (1987) Spectral Energy Distributions of T Tauri Stars—Disk Flaring and Limits on Accretion. *The Astrophysical Journal*, **323**, 714-733. https://doi.org/10.1086/165866

[38] van der Marel, N., *et al.* (2016) The (w)hole Survey: An Unbiased Sample Study of Transition Disk Candidates Based on Spitzer Catalogs. *Astronomy & Astrophysics*, **592**, A126. https://doi.org/10.1051/0004-6361/201628075

[39] Fang, M., *et al.* (2013) Young Stellar Objects in Lynds 1641: Disks, Accretion, and Star Formation History. *The Astrophysical Journal Supplement Series*, **207**, A5. https://doi.org/10.1088/0067-0049/207/1/5

[40] Kusune, T., *et al.* (2015) Near-IR Imaging Polarimetry toward a Bright-Rimmed Cloud: Magnetic Field in SFO 74. *The Astrophysical Journal*, **798**, A60. https://doi.org/10.1088/0004-637X/798/1/60

[41] Sano, T., *et al.* (2000) Magnetorotational Instability in Protoplanetary Disks. II. Ionization State and Unstable Regions. *The Astrophysical Journal*, **543**, 486-501. https://doi.org/10.1086/317075

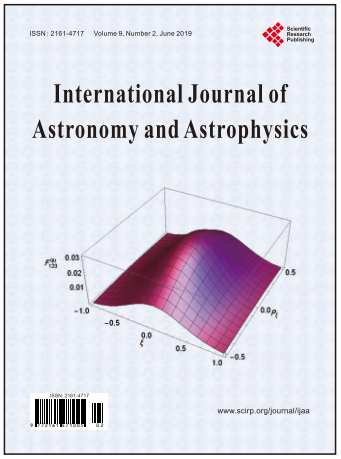

Call for Papers

International Journal of Astronomy and Astrophysics (IJAA)

ISSN 2161-4717 (Print) ISSN 2161-4725 (Online)
http://www.scirp.org/journal/ijaa

International Journal of Astronomy and Astrophysics **(IJAA)** is an international scientific journal dedicated to the publication and public discussion of high quality original research in all the fields of astrophysics and space sciences and related technology. All the manuscripts must be prepared in English, and are subject to a rigorous and fair peer-review process. Accepted papers will immediately appear online followed by printed hard copies.

Editor-in-Chief

Prof. Michael D. Smith University of Kent, UK

Editorial Board

Subject Coverage

The journal publishes original papers including but not limited to the following fields:

- Astrogeodynamics
- Astrophysics
- Cosmic Rays and Gamma Astronomy
- Dynamics of Celestial Bodies in the Solar System and Artificial Bodies
- Extrasolar Planets
- Formation and Evolution of Galaxies and Their Clusters
- Formation and Evolution of Stars
- Heliospheric Physics
- High-Energy and Cataclysmic Processes in Astrophysics
- Interstellar Matter
- Interstellar Medium: Star Formation Regions
- Kinematics and Structure of the Galaxy
- Large-Scale Structure of Universe Formation and Evolution of Galaxies
- Last Stages of Stellar Evolution and Chemical Evolution of the Galaxy
- Magnetospheric Physics
- Microquasars and High-Energy Astrophysics
- Neutron Astronomy
- New Astronomical Techniques and Methods
- Planets, Comets, Asteroids and Dust
- Pulsar Magnetospheres
- Solar and Stellar Physics
- Solar Magnetic Activity and Heliogeospace Environments
- Solar/Interstellar Terrestrial Relations
- Solar-Terrestrial Physics and Space Weather
- Space Observation and Exploration
- Supernovae and Evolution of the Universe

We are also interested in short papers (letters) that clearly address a specific problem, and short survey or position papers that sketch the results or problems on a specific topic. Authors of selected short papers would be invited to write a regular paper on the same topic for future issues of the IJAA.

Notes for Intending Authors

Submitted papers should not have been previously published nor be currently under consideration for publication elsewhere. Paper submission will be handled electronically through the website. All papers are refereed through a peer review process. For more details about the submissions, please access the website.

http://www.scirp.org/journal/ijaa **E-mail: ijaa@scirp.org**

What is SCIRP?

Scientific Research Publishing (SCIRP) is one of the largest Open Access journal publishers. It is currently publishing more than 200 open access, online, peer-reviewed journals covering a wide range of academic disciplines. SCIRP serves the worldwide academic communities and contributes to the progress and application of science with its publication.

What is Open Access?

All original research papers published by SCIRP are made freely and permanently accessible online immediately upon publication. To be able to provide open access journals, SCIRP defrays operation costs from authors and subscription charges only for its printed version. Open access publishing allows an immediate, worldwide, barrier-free, open access to the full text of research papers, which is in the best interests of the scientific community.

- High visibility for maximum global exposure with open access publishing model
- Rigorous peer review of research papers
- Prompt faster publication with less cost
- Guaranteed targeted, multidisciplinary audience

Scientific Research Publishing

Website: http://www.scirp.org

Subscription: sub@scirp.org

Advertisement: service@scirp.org